Uncertainty in Thermal Modeling of Spent Nuclear Fuel Casks

Spent Fuel and Waste Disposition

Prepared for
US Department of Energy
Spent Fuel and Waste Science and Technology

David J. Richmond, Sarah R. Suffield, James A. Fort, Megan E. Higley
Pacific Northwest National Laboratory

September 23, 2022
M3SF-22PN010203023
PNNL-33409

DISCLAIMER

This information was prepared as an account of work sponsored by an agency of the U.S. Government. Neither the U.S. Government nor any agency thereof, nor any of their employees, makes any warranty, expressed or implied, or assumes any legal liability or responsibility for the accuracy, completeness, or usefulness, of any information, apparatus, product, or process disclosed, or represents that its use would not infringe privately owned rights. References herein to any specific commercial product, process, or service by trade name, trade mark, manufacturer, or otherwise, does not necessarily constitute or imply its endorsement, recommendation, or favoring by the U.S. Government or any agency thereof. The views and opinions of authors expressed herein do not necessarily state or reflect those of the U.S. Government or any agency thereof.

SUMMARY

Uncertainty is a key metric in computational modeling that must be evaluated for results to have wide ranging applicability. A well characterized uncertainty range is ideal with clear error bars on results that can be presented to stakeholders. In the field of spent fuel cask modeling, this ideal has been historically difficult to achieve in practice because of the computationally intensive nature of the models used and the difficulty assigning reasonable uncertainties to quantities in as-built systems. The work in this report has been conducted to evaluate the overall state of uncertainty and sensitivity in spent fuel cask models and develop methodologies for evaluating these uncertainties. These methodologies must be practical for engineering applications. They should not require excessive computational resources or calendar time to achieve results. In engineering, the model must be on a scale such that it can be changed and adapted throughout a project as new information is discovered and project goals evolve.

This report covers three major modeling task areas that provide an overview of the types of sensitivity and uncertainty present in a spent fuel storage and transportation system. Section 3 discusses sensitivity and uncertainty analysis in the effective thermal conductivity model for the fuel region and applies these results to a single assembly model. Section 4 shows sensitivity analysis of a full cask model in the TN-32B and Section 5 demonstrates the overall uncertainty workflow using Coolant Boiling in Rod Arrays – Spent Fuel Storage and STAR-CCM+ developed from the sensitivity work in the preceding sections. Key outcomes and demonstrations from this work include:

- The results of the effective thermal conductivity uncertainty quantification show that this quantity, while important to modeling, has minimal effect on overall uncertainty and can be estimated reliably with different codes.
- Key sensitivities were identified in the TN-32B High Burnup Demonstration Research Project Cask; these will inform uncertainty analysis and future transient modeling.
- Latin hypercube sampling uncertainty quantification was demonstrated as a practical method for uncertainty quantification even with computationally intensive full cask models.
- Full cask model uncertainty results showed good agreement with data and demonstrated the importance of input parameter distribution selection.
- Methodology for a streamlined workflow utilizing multiple analysis tools was developed and can be applied to any future spent fuel cask modeling or other relevant systems that can be computationally modeled.

The work in this report was undertaken to study sensitivities and uncertainties in spent fuel cask modeling and then develop methodologies for uncertainty analysis that can be practically applied to future work. These goals were successfully met and there is now a demonstrated workflow in place that the U.S. Department of Energy can use when analyzing thermal models and can that be applied to other relevant computational modeling areas.

This page is intentionally left blank.

ACKNOWLEDGEMENTS

The authors would like to acknowledge the Department of Energy Spent Fuel and Waste Science Technology program for funding this work. The Electric Power Research Institute provided a continued data collection and distribution for the High Burnup Demonstration Research. Sandia National Laboratories staff members were key to this work by conducting the Dry Cask Simulator project. Project management support was provided by Brady Hanson and Steve Ross. Ben Jensen was the technical reviewer and Holly Campbell provided editing support.

This page is intentionally left blank.

CONTENTS

SUMMARY iii

ACKNOWLEDGEMENTS v

ACRONYMS xiii

1. INTRODUCTION 1

2. METHODOLOGY 3
   - 2.1 Uncertainty Types 3
     - 2.1.1 Model Uncertainty 3
     - 2.1.2 Numerical Uncertainty 3
     - 2.1.3 Input Uncertainty 4
   - 2.2 Uncertainty vs. Sensitivity 4
   - 2.3 Latin Hyper Cube Sampling Uncertainty Quantification 4

3. FUEL REGION EFFECTIVE THERMAL CONDUCTIVITY UNCERTAINTY QUANTIFICATION 5
   - 3.1 Model Construction 5
     - 3.1.1 Full versus Partial Array Modeling 5
     - 3.1.2 STAR-CCM+ Modeling 7
   - 3.2 Sensitivity Studies 7
     - 3.2.1 Assumptions 7
     - 3.2.2 Radial Effective Thermal Conductivity Calculation 7
   - 3.3 Initial Simulations and Observations 8
   - 3.4 Uncertainty Quantification 12
     - 3.4.1 Error due to Iteration and Discretization 12
     - 3.4.2 Rod and Cladding Thickness Tolerancing 14
     - 3.4.3 Cladding Emissivity 15
     - 3.4.4 Channel Emissivity 15
   - 3.5 Effective Thermal Conductivity and Uncertainty Calculations 15
   - 3.6 Predicted PCT and Uncertainty 18
   - 3.7 Key Results 18

4. SENSITIVITY ANALYSES FOR HIGH BURNUP DEMONSTRATION 21
   - 4.1 Steady State Models 21
     - 4.1.1 Updates to the Porous Media Model 21
     - 4.1.2 Sensitivity Runs 26
       - 4.1.2.1 Gap at Liner Base 27
       - 4.1.2.2 Thermal Radiation Included in Base Gap 29
       - 4.1.2.3 Ambient Temperature 30
       - 4.1.2.4 Gap Between Transition Rails and Basket 32
       - 4.1.2.5 Decay Heat 34
       - 4.1.2.6 Neutron Shield 36

4.2 Representation of Sensitivity Results 40
4.3 Transient Models 41
4.3.1 Model Updates 41
4.3.1.1 Detailed Model 42
4.3.1.2 Porous Media Model 42
4.3.2 Model Comparison and Initial Sensitivity Runs 43
4.3.2.1 Thermal Properties during Vacuum Drying 43
4.3.2.2 Rerun of Detailed Case Starting from Lid Placement in Pool 44
4.3.3 Implications for Uncertainty 45

5. UNCERTAINTY QUANTIFICATION FOR HIGH BURNUP DEMONSTRATION RESEARCH PROJECT CASK 47
5.1 STAR-CCM+ 48
5.2 COBRA-SFS 58
5.3 Combined Uncertainty Results 64
5.4 Computational Resources and Workflow 66

6. CONCLUSIONS 69

7. REFERENCES 71

LIST OF FIGURES

Figure 3-1. Detailed models of the a) partial length rods and b) full length rods 6

Figure 3-2. Representation of the modeling of the partial rod arrays and the full rod arrays with details for volume calculations 8

Figure 3-3. Effective thermal conductivities for the original calculation, each modeling type, and alternate calculations for channel emissivity = 0.17 9

Figure 3-4. Effective thermal conductivities for the original calculation, each modeling type, and alternate calculations for channel emissivity = 0.6505 9

Figure 3-5. Effective thermal conductivity for modeling techniques replicating STAR-CCM+ modeling for channel emissivity = 0.17 10

Figure 3-6. Effective thermal conductivity for modeling techniques replicating STAR-CCM+ modeling for channel emissivity = 0.6505 11

Figure 3-7. Peak cladding change for different modeling techniques from original k_{eff} calculation 12

Figure 3-8. Error due to spatial discretization for three different meshes as calculated by the GCI 13

Figure 3-9. Fuel rod and cladding tolerancing effects on k_{eff} 14

Figure 3-10. Fuel rod cladding emissivity effects on k_{eff} 15

Figure 3-11. k_{eff} curves for two heights and their upper and lower uncertainty bounds 16

Figure 3-12. PDFs from previous work and current work with experimental measurement of the PCT 18

Figure 4-1. Difference between STAR-CCM+ model predictions and measurements of fuel temperatures for basket cell 14; 0.125-inch gap between liner base and gamma shield 23

Figure 4-2. Difference between STAR-CCM+ model predictions and measurements of fuel temperatures for basket cell 14; 0.001-inch gap between liner base and gamma shield 24

Figure 4-3. Difference between STAR-CCM+ model predictions and measurements of fuel temperatures for basket cells 2 and 28; 0.125-inch gap between liner base and gamma shield 25

Figure 4-4. Definition of cask surface temperature measurement locations 27

Figure 4-5. Difference between STAR-CCM+ porous model predictions and measurements of Cell 14 fuel temperatures for basket cells; sensitivity to gap between liner base and gamma shield 28

Figure 4-6. Difference between STAR-CCM+ porous model predictions and measurements of "A" cask surface temperatures for basket cells; sensitivity to gap between liner base and gamma shield 29

Figure 4-7. Difference between STAR-CCM+ porous model predictions and measurements of Cell 14 fuel temperatures for basket cells; sensitivity to inclusion of thermal radiation in gap between liner base and gamma shield 30

Figure 4-8. Difference between STAR-CCM+ porous model predictions and measurements of Cell 14 fuel temperatures for basket cells; sensitivity to ambient temperature 31

Figure 4-9. Difference between STAR-CCM+ porous model predictions and measurements of "A" cask surface temperatures for basket cells; sensitivity to ambient temperature 32

Figure 4-10. Difference between STAR-CCM+ porous model predictions and measurements of Cell 14 fuel temperatures for basket cells; sensitivity to gap resistance between basket and transition rails 33

Figure 4-11. Difference between STAR-CCM+ porous model predictions and measurements of "A" cask surface temperatures for basket cells; sensitivity to gap resistance between basket and transition rails 34

Figure 4-12. Difference between STAR-CCM+ porous model predictions and measurements of Cell 14 fuel temperatures for basket cells; sensitivity to decay heat loading 35

Figure 4-13. Difference between STAR-CCM+ porous model predictions and measurements of "A" cask surface temperatures for basket cells; sensitivity to decay heat loading 36

Figure 4-14. Difference between STAR-CCM+ porous model predictions and measurements of Cell 14 fuel temperatures for basket cells; sensitivity to neutron shield resin thermal conductivity 37

Figure 4-15. Difference between STAR-CCM+ porous model predictions and measurements of "A" cask surface temperatures for basket cells; sensitivity to neutron shield resin thermal conductivity 38

Figure 4-16. Difference between STAR-CCM+ porous model predictions and measurements of Cell 14 fuel temperatures for basket cells; sensitivity to gap thicknesses on both sides of the neutron shield boxes 39

Figure 4-17. Difference between STAR-CCM+ porous model predictions and measurements of "A" cask surface temperatures for basket cells; sensitivity to gap thicknesses on both sides of the neutron shield boxes 40

Figure 4-18. Comparison of model results for measurement locations in Cell 14 44

Figure 5-1. Air temperature in the decontamination pit (ambient TC) and above the work platform (logger 1 and 2 TC) 48

Figure 5-2. Number of cases sensitivity study results for PCT 49

Figure 5-3. STAR-CCM+ High Burnup Demonstration model results for PCT 52

Figure 5-4. STAR-CCM+ High Burnup Demonstration model results for cask surface temperatures 52

Figure 5-5. STAR-CCM+ High Burnup Demonstration model results for 3K7 fuel TCs 53

Figure 5-6. STAR-CCM+ High Burnup Demonstration model results for 3U4 fuel TCs 53

Figure 5-7. STAR-CCM+ High Burnup Demonstration model results for 3U6 fuel TCs 54

Figure 5-8. STAR-CCM+ High Burnup Demonstration model results for 3U9 fuel TCs 54

Figure 5-9. STAR-CCM+ High Burnup Demonstration model results for 5T9 fuel TCs 55

Figure 5-10. STAR-CCM+ High Burnup Demonstration model results for 30A fuel TCs 55

Figure 5-11. STAR-CCM+ High Burnup Demonstration model results for 57A fuel TCs 56

Figure 5-12. COBRA-SFS results assembly 2 (3k7) lance 61

Figure 5-13. COBRA-SFS results assembly 6 (30A) lance 61

Figure 5-14. COBRA-SFS results assembly 14 (57A) lance 62
Figure 5-15. COBRA-SFS results assembly 19 (3U9) lance 62
Figure 5-16. COBRA-SFS results assembly 24 (3U4) lance 63
Figure 5-17. COBRA-SFS results assembly 28 (3U6) lance 63
Figure 5-18. COBRA-SFS results assembly 31 (5T9) lance 64
Figure 5-19. STAR-CCM+ PCT data (black) and COBRA-SFS PCT data (red) 65
Figure 5-20. 95–95 interval vs number of samples 65
Figure 5-21. Wall time vs. number of simulations 67

LIST OF TABLES

Table 3-1. Measured channel box emissivity as a function of height with bounds used for k_{eff} uncertainty simulations 6

Table 3-2. Associated calculations for GCI and estimated error for Tw = 300 K 13

Table 3-3. Curve-fit polynomials for k_{eff} calculated at each height with the elevations the polynomial was implemented between in the DCS model 17

Table 3-4. Uncertainty percentages for each keff polynomial as a function of average bundle temperature. 17

Table 4-1. Sensitivity cases 26

Table 4-2. Summary of differences in porous model predictions from measurements 41

Table 5-1. Perturbation parameters 47

Table 5-2. Results for STAR-CCM+ High Burnup Demonstration Model LHS Analysis 50

Table 5-5. Wall time for COBRA-SFS and STAR-CCM+ 66

ACRONYMS

BWR	boiling water reactor
CFD	Computational Fluid Dynamics
CI	confidence interval
COBRA-SFS	Coolant Boiling in Rod Arrays – Spent Fuel Storage
DCS	Dry Cask Simulator
DOE	Department of Energy
EPRI	Electric Power Research Institute
GRS	Gesellschaft für Anlagen- und Reaktorsicherheit (Global Research for Safety)
HBU	high burnup
ISFSI	independent spent fuel storage installation
LHS	Latin Hypercube Sampling
PCT	peak cladding temperature
PDF	probability distribution function
PNNL	Pacific Northwest National Laboratory
SFWST	Spent Fuel and Waste Science and Technology
SNF	spent nuclear fuel
SNL	Sandia National Laboratories
SUSA	Software for Uncertainty and Sensitivity Analyses
TC	thermocouple
UQ	Uncertainty Quantification

This page is intentionally left blank.

UNCERTAINTY IN THERMAL MODELING OF SPENT NUCLEAR FUEL CASKS

1. INTRODUCTION

Uncertainty is a key metric in computational modeling that must be evaluated for results to have wide ranging applicability. A well characterized uncertainty range is ideal with clear error bars on results that can be presented to stakeholders. In the field of spent fuel cask modeling, this ideal has been historically difficult to achieve in practice because of the computationally intensive nature of the models used and the difficulty assigning reasonable uncertainties to quantities in as-built systems. The work in this report has been conducted to evaluate the overall state of uncertainty and sensitivity in spent fuel cask models and to develop methodologies for evaluating these uncertainties. These methodologies must be practical for engineering applications. They should not require excessive computational resources or calendar time to achieve results. In engineering analysis, the model must be on a scale such that it can be changed and adapted throughout a project as new information is discovered and project goals evolve.

In sensitivity studies, parameters are typically varied one at a time, and this can be effective when their effect can be isolated from other parameters. But when paired inputs can produce a potentially non-linear response, simple sensitivity testing is no longer adequate. In real systems, there are numerous interdependent input parameters whose effects cannot be readily isolated. To analyze sensitivity and uncertainty, other approaches that examine combined parameter effects have been developed, for example, the mathematically rigorous technique known as uncertainty quantification (UQ) by polynomial chaos (Knio 2005, Najm 2009). (Khalil 2018) applied this technique to spent nuclear fuel storage. Another approach to UQ is described by Glaeser (2008) and can be applied using the Gesellschaft für Anlagen- und Reaktorsicherheit (Global Research for Safety [GRS]) developed toolset, Software for Uncertainty and Sensitivity Analyses (Kloos and Hofer 1999). An application using the GRS methodology was recently performed by Angelucci (2022). A similar approach is implemented using the Dakota (Dakota 2021) toolset developed by Sandia National Laboratories (SNL). A study of these proposed methodologies and a survey of the available toolsets were applied to the work detailed in this report.

The report is organized to provide a flow from isolated sensitivity and uncertainty parameters in Section 3 to sensitivity analysis on a full cask in Section 4 and then to demonstration of a full cask uncertainty analysis in Section 5. In all cases, the modeling work was designed to provide insight into the process more than to provide specific results. Although the results are valid and relevant, a more focused modeling project may be able to better define sensitivity and uncertainty ranges for specific applications and quantities of interest.

This page is intentionally left blank.

2. METHODOLOGY

The broad set of activities included in code and solution verification and validation and UQ in Computational Fluid Dynamics (CFD) are described in AIAA (2022). Code verification is the process of establishing the correct implementation of the model equations and solution scheme for a particular application. This step verifies that the numerical solution CFD code agrees with the exact solution of the model equations. Solution verification is the process of estimating the errors for representative verification test cases, including the effects of discretization and boundary conditions, to demonstrate that the accuracy is adequate for the intended application. For this study, code and solution verification are assumed to have been performed by the code developers. For the commercial code, STAR-CCM+, evidence of this is shown in the verification and validation case results that accompany each code release. For Coolant Boiling in Rod Arrays – Spent Fuel Storage (COBRA-SFS), a suite of cases is run upon each release to confirm results against previous validation (Michener 2017).

Code validation establishes the ability of the CFD models to represent physical reality in the intended application. Model validation has been the focus of the Spent Fuel and Waste Science and Technology (SFWST) thermal modeling efforts comparing model predictions with experimental measurements for the high burnup (HBU) demonstration (Fort et al. 2019a, Fort et al. 2020) and for the dry cask simulator (Suffield et al. 2020a, 2020b). These efforts have shown the difference between measurements and predictions for a select set of model inputs, but in general they have not shown uncertainties for the model predictions or the experimental measurements and the extent to which they overlap.

2.1 Uncertainty Types

Multiple systems have been used in literature and other reporting methods to categorize uncertainty. In this work, uncertainty discussion is defined by its source and the methods available to reduce it. The three categories used are model, numerical, and input uncertainty. It is important to categorize uncertainty factors correctly because it helps direct whether and what type of work can be undertaken to reduce uncertainty.

2.1.1 Model Uncertainty

Model uncertainty is the uncertainty introduced by modeling choices and abstractions needed to translate the physical world to a numerical model. This may include uncertainty from correlations, simplifications, and assumptions. This type of uncertainty is difficult to characterize and quantify because the methods needed to quantify this are generally expensive and time consuming. For correlations, separate effects testing is generally needed to compare correlation calculations against data. The best way to assess simplifications and assumptions is to do a model without the assumption in question and compare results. This, of course, assumes that it is possible and practical to do this model, which begs the question of why the model would be simplified in the first place. For these reasons, very little time is spent discussing model uncertainty in this report and it is not quantified. In general, the best way to deal with model uncertainty in practical applications is to make model selections with a known bias. For engineering purposes, a conservative bias is usually selected relative to whatever limit is being evaluated with the model.

2.1.2 Numerical Uncertainty

Numerical uncertainty is the uncertainty introduced by the numerical methods used to discretize a problem. In CFD and thermal modeling, this is often seen in meshing strategies and can be identified and quantified through use of the grid convergence index (GCI). Although GCI provides an indicator of mesh refinement, it still does not give a complete analysis of numerical error, especially in unstructured meshes with local refinements. There also may be some error due to convergence (iteration) because solutions can oscillate and criteria for convergence are selected to stop solution execution. In spent fuel storage and transportation casks, this error is usually minor and when calculated results in less than 0.5 °C of

uncertainty in most thermal analysis results. This is compared to other modeling fields involving complex flows and turbulence modeling where relatively wide convergence criteria may be needed to manage solutions.

2.1.3 Input Uncertainty

Input uncertainty is in general the easiest uncertainty to quantify, although it presents its own challenges to characterization. It is also usually a large factor in spent fuel cask modeling, and as such is, the area most of the work detailed in this report tried to address. This type of uncertainty is often due to manufacturing tolerances and boundary conditions, where these items are either unknown in the general case or have uncertainty ranges specified where specific information is available. When inputs are unknown, a reasonable range must be selected using engineering judgement, which can present a source of modeler-modeler variation even among reported uncertainty.

2.2 Uncertainty vs. Sensitivity

Uncertainty and sensitivity are related and often conflated but are distinct aspects of a model and should not be confused. The sensitivity of a model is the response of a quantity of interest relative to a change in the input parameters. To study sensitivity, input perturbations are usually selected in a range that will produce a response on the output. The key distinction between an uncertainty and sensitivity study is that the perturbations of inputs in sensitivity studies do not need to be selected in a reasonable range. In fact, a model may be highly sensitive to a parameter that has little to no uncertainty. For example, a thermal model may be highly sensitive to solid material thermal conductivity, but there is little uncertainty in this for most materials. The end result here would be minimal uncertainty due to thermal conductivity.

2.3 Latin Hyper Cube Sampling Uncertainty Quantification

Latin hypercube sampling (LHS) is a statistical method that can be used to sample a range of variables in a manner that covers the parameter space evenly (Adams et al. 2018, Oberkampf and Roy 2010). This is a more efficient method of covering a parameter's space than Monte Carlo sampling and has similar applications. For uncertainty quantification, Latin hypercube sampling is particularly powerful because it allows inputs to be defined as a probability distribution and allows models with non-linear responses to be evaluated with multiple simulations that generate statistics like mean and standard deviation. In this report, samples and simulations may be used interchangeably because during an analysis, each input is sampled and those sampled values are simulated as a set, then the result is recorded so that all of the values can be analyzed together to generate statistics. In this way a particular uncertainty "run" will include many modeling tool "runs" within it.

Usually, a 95–95 confidence interval is set for results, which is defined as a range that encompasses 95% of the possible realizations with 95% confidence. A 95% range is equivalent to two standard deviations (2σ). For high assurance models and critical safety analyses, it may be appropriate to utilize a wider range of 3σ (99.7%) or a different approach entirely. The LHS UQ method presents significant advantages to other methods because it allows for consideration of non-uniform distributions and can generate asymmetric error bars for a 95–95 confidence interval. In spent fuel cask thermal modeling, this is very relevant to parameters like gap size or fill gas pressure. The temperature response to these inputs tends to be asymptotic.

3. FUEL REGION EFFECTIVE THERMAL CONDUCTIVITY UNCERTAINTY QUANTIFICATION

The Dry Cask Simulator (DCS) was an experiment conducted at SNL that generated experimental datasets of flow and temperature measurements for a single, electrically heated but otherwise prototypic 9 × 9 boiling water reactor (BWR) fuel assembly (Durbin and Lindgren 2017). Previously, several models of the DCS in its horizontal and vertical configurations were constructed (Suffield et al. 2020a, 2020b). These models were run for many different combinations of heat load, fill gas, and internal pressure. Sensitivity analysis indicated which parameters have significant effects on peak cladding temperature (PCT) prediction. One of those factors that was determined to be sensitive is the radial effective thermal conductivity, k_{eff}. In previous work, an uncertainty of 10% was assigned to this parameter, based on engineering judgement. Although k_{eff} is a sub-model derived property (Jensen et al. 2021), it can be treated as input in a full model.

In this work, to better approximate its uncertainty, the radial effective thermal conductivity was rederived with uncertainty built into its modeling. The 2-D models of the single fuel assembly used in the DCS were created in ANSYS/Fluent. First, common modeling techniques were investigated for their impact on PCT and k_{eff}. Next, convergence and discretization error were estimated. Sensitivity studies on model inputs were conducted and uncertainty on PCT and the resulting k_{eff} was determined. Finally, this k_{eff} uncertainty was implemented in the DCS model, along with previously determined uncertainties, to estimate PCT uncertainty in the DCS for comparison with previous simulation and experimental data.

The modeling results are specific to the DCS; however, the techniques can be applied for any future models using a k_{eff} sub-model. In addition, the order of magnitude in uncertainty will be similar in any fuel assembly k_{eff}. This allows the results to be applied qualitatively to future modeling efforts and gives an understanding of spent fuel thermal model uncertainty generally.

3.1 Model Construction

The base 2-D model was created in the ANSYS Design Modeler, as shown in Figure 3-1. Dimensions and material specifications were taken from the Dry Cask Simulator Handbook (Lindgren and Durbin 2017). The magnesium oxide heater rods (fuel surrogate) were modeled as perfect circles of their nominal radius. The Incoloy heater rod cladding was assumed to have its nominal thickness and to be in intimate contact with the heater rod. The water rods are modeled with their nominal radius and are made of Zircaloy. The channel box is modeled as a square without beveling, with nominal dimensions and material properties of Zircaloy. The assembly is a 9 × 9 BWR array with seven rods from the center replaced by the two water rods. From this base model, small adjustments are made to capture specific DCS features, investigate the impacts of different modeling techniques, and conduct the sensitivity studies.

3.1.1 Full versus Partial Array Modeling

The majority of the fuel assembly modeling presented in this section can be directly applied to modeling of other spent fuel storage systems. However, there are a few unique features of the DCS that are atypical of spent fuel storage systems, requiring special treatment to capture. One feature of the DCS that requires special treatment are the partial rods. In the DCS assembly, eight of the rods are approximately 1.25 m shorter than the others (depiction shown in Figure 3-2). This can significantly affect the radial fuel effective thermal conductivity calculation because of the absence of heat generation of these rods and their replacement with helium volume. Two models were used to capture this geometry: one model simulated the top portion of the assembly where the partial rods had ended (shown in Figure 3-1a) and another simulated the assembly with all rods (shown in Figure 3-1b). The depths of these sections, although it is a 2-D model with no explicitly modeled depth, is an important parameter that is implemented in ANSYS/Fluent. The length of the partial section is 1.249 m and the length of the full section is 2.402 m, as depicted in Figure 3-2. Comparisons were made between the models to investigate

the impacts of the full and partial rod modeling on the k_{eff}. Comparisons were also made with previous k_{eff} values, which were based off a partial model constructed in STAR-CCM+ (Suffield et al. 2020).

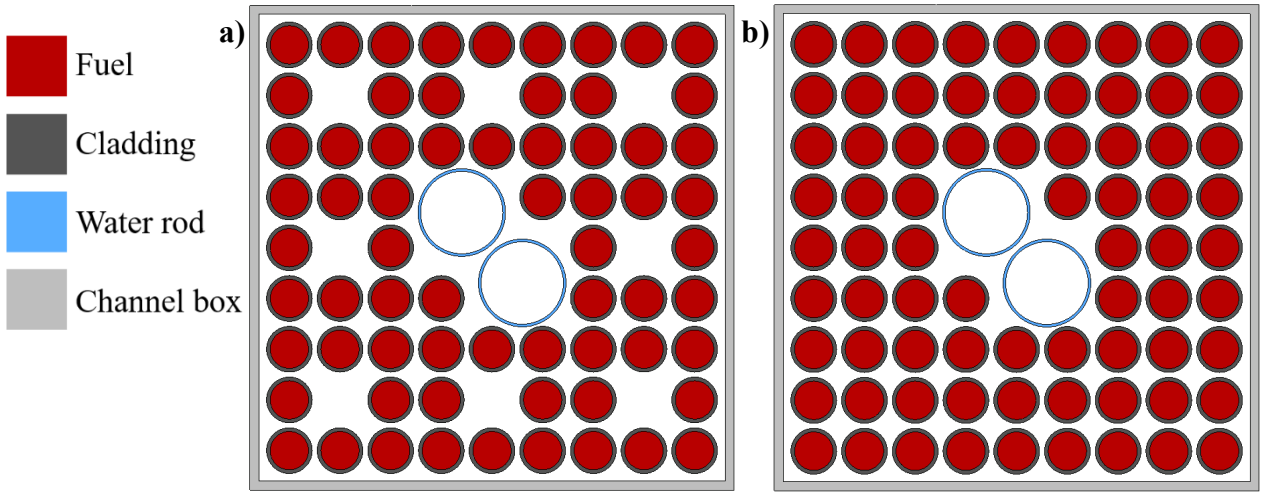

Figure 3-1. Detailed models of the a) partial length rods and b) full length rods

Another feature is the varying emissivity of the channel box and water rods. Table 3-1 shows the measured emissivity of the DCS assembly channel box as a function of height (Lindgren and Durbin 2017). The emissivity of the channel box and water rods varied between 0.156 and 0.655 along their length. This may have a significant effect on the effective thermal conductivity because radiation heat transfer is modeled as part of this calculation. Because of this, sensitivity studies were conducted to determine how much impact the varying channel emissivity has on the effective thermal conductivity. This helps inform future treatment of the varying emissivity for the uncertainty calculation. A common modeling practice is to model the fuel and cladding as one material with calculated effective properties. The original, STAR-CCM+ 2-D k_{eff} models of the fuel assembly used this modeling practice, so the effects of modeling the fuel and cladding separately (detailed) and as one material (smeared) are investigated.

Table 3-1. Measured channel box emissivity as a function of height with bounds used for k_{eff} uncertainty simulations

	Measured Average HTE				Simulation Bounds	
Height (in.)	Side 2	Side 1	Side 3	Side 4	Lower Bound	Upper Bound
0	0.156	0.172	0.187	0.181	0.156	0.187
12	0.162				0.150	0.175
24	0.157	0.176	0.166	0.175	0.157	0.176
36	0.175				0.166	0.184
48	0.214	0.231	0.221	0.224	0.214	0.231
60	0.301				0.287	0.315
72	0.402	0.423	0.44	0.425	0.402	0.440
84	0.436				0.420	0.453
96	0.535	0.543	0.555	0.527	0.527	0.555
108	0.595				0.586	0.605
120	0.632	0.639	0.629	0.639	0.629	0.639
132	0.653				0.647	0.660

	Measured Average HTE				Simulation Bounds	
Height (in.)	Side 2	Side 1	Side 3	Side 4	Lower Bound	Upper Bound
144	0.654	0.639	0.655	0.643	0.639	0.655
156	0.505	0.538	0.546	0.533	0.505	0.546

3.1.2 STAR-CCM+ Modeling

Both ANSYS/Fluent and STAR-CCM+ rely on finite volume methods, so depth is an important consideration for 2-D models. In ANSYS/Fluent, depth can be set to correspond to the geometry, as previously discussed and depicted in Figure 3-2. STAR-CCM+ assumes a unit depth that cannot be changed. To adjust this for the volumetric heat generation rate calculation, the entire volume of the fuel was calculated manually and implemented into the model, along with the 3.651 m heated length of the assembly. Additionally, the STAR-CCM+ model used for the original k_{eff} calculation modeled the rods using the diameter of the fuel without the cladding, but with effective properties of the fuel and cladding. To mimic the STAR-CCM+ model in ANSYS/Fluent, the Partial-Smeared-NoCladding (66 rods with a depth of 1.249 m with smeared properties without additional cladding diameter) and the Partial-Smeared-Long-NoCladding (66 rods with a depth of 3.651 m with smeared properties without additional cladding diameter) models were created.

3.2 Sensitivity Studies

The sensitivity study that required adjustments to the base model was the dimensional tolerancing study. For the tolerancing investigation, the fuel radius and cladding thickness were increased or decreased by 0.013 mm and 0.04 mm, respectively, which are the 3σ manufacturing uncertainties of the PB-2 BWR assembly (Ivanov 2013). The fuel and cladding were modeled with the same material properties and assumptions as the base model.

Using these modeling adjustments, four initial models were used to investigate common modeling techniques (Partial-Smeared, Full-Smeared, Partial-Detailed, and Full-Detailed). Because of differences with STAR-CCM+ and ANSYS/Fluent, two additional models were created to allow ANSYS/Fluent to mimic the original STAR-CCM+ model (Partial-Smeared-NoCladding and Long-Smeared-NoCladding).

3.2.1 Assumptions

It is assumed that the heat generation rate through the active portion of the rods is uniform in its distribution. No bowing in the fuel assembly or rods is assumed.

3.2.2 Radial Effective Thermal Conductivity Calculation

To calculate the radial effective thermal conductivity, temperature boundary conditions were applied to the channel box of the 2-D models. Using Eq. 1, the effective radial thermal conductivity was calculated for different heat generation rates and temperature boundary conditions. The radial effective thermal conductivity, k_{eff}, is given by

$$k_{eff} = \frac{0.2947Q}{4L_a(T_{PC}-T_w)} \quad \text{(Eq. 1)}$$

where Q is the heat generation, L_a is the active length, T_{PC} is the PCT, and T_w is the uniform wall temperature (Bahney and Lotz 1996). For the nominal calculation, the heat generation was taken as the total heat generation of the assembly, and the active length was taken as the length of the entire assembly (3.651 m). This made the Q and L_a in the calculation for full and partial rods the same. For the alternate calculation, the active length and heat generation were reduced by the fraction of total heater volume contained in that section. The full rod portion of the assembly has all 74 rods generating heat, while the partial rod portion of the assembly only has 66 rods generating heat. Because of this, the partial rod array has 34% of the length of the assembly, but only 32% of the volume. For the alternate calculations in the partial rod portion, Q is reduced to correspond to its volume fraction of the assembly (32%) and L_a is

reduced to its length fraction of the assembly (34%). For the alternate calculation in the full rod portion, Q is reduced to correspond to its volume fraction of the assembly (68%) and L_a is reduced to its length fraction of the assembly (66%).

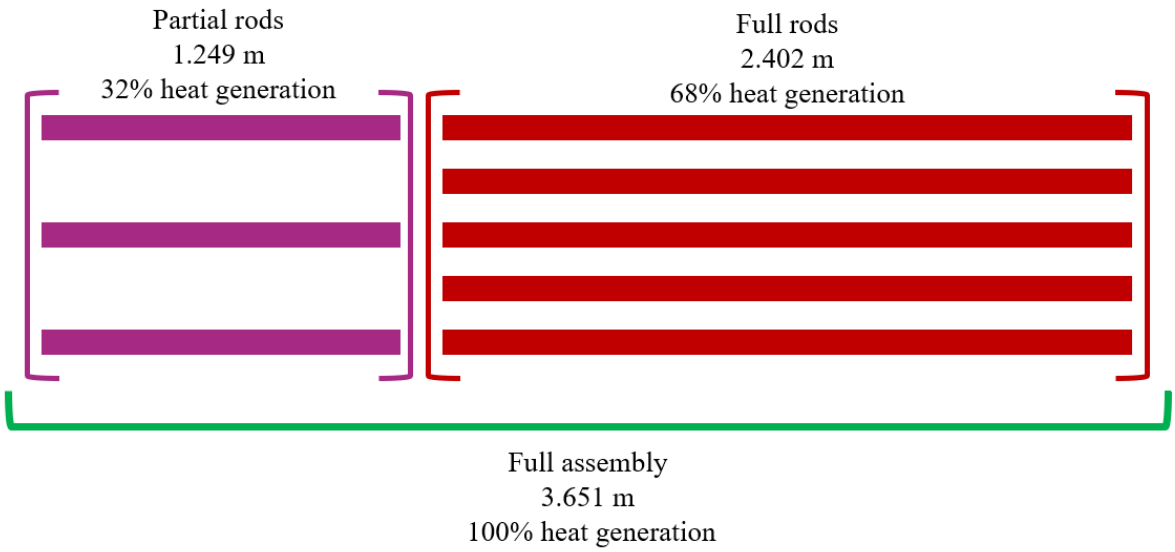

Figure 3-2. Representation of the modeling of the partial rod arrays and the full rod arrays with details for volume calculations

3.3 Initial Simulations and Observations

Initial simulations were conducted to understand the effects of different modeling techniques. These techniques are not directly related to error, but they may affect results. These modeling techniques are the detailed versus smeared modeling and the modeling of the partial versus full rod arrays, as previously described. Each of these modeling techniques in combination were evaluated at a low and high heat generation (0.5 kW and 5 kW), low and high channel and water rod emissivity (0.17 and 0.6505), and many wall temperatures (300 K to 900 K in increments of 50 K) to calculate their effective thermal conductivity. In addition, two different effective thermal conductivity calculations were conducted; one standard calculation with the full rod length and full heat generation, and the alternate calculation that used reduced values for the rod length and heat generation based on the full or partial rods, as described in the preceding section. These results were also compared to the original effective thermal conductivity derived using STAR-CCM+ at each emissivity.

Figure 3-3 and Figure 3-4 show the effective thermal conductivities using each modeling technique, Figure 3-3 for a channel emissivity of 0.17 and Figure 3-4 for a channel emissivity of 0.6505. Both figures show overlapping results for the Partial-Smeared and Partial-Detailed models and overlapping results for the full smeared and Full-Detailed models. This indicates that detailed versus smeared modeling has very little impact on k_{eff}. It also indicates, though, that partial versus full modeling does have an impact on the k_{eff}. Also, the k_{eff} based on the partial modeling is higher than full modeling, with this difference increasing with increasing temperatures. Between the partial and full modeling are the alternate calculations, which use the earlier explained method of calculation. Because the calculation method considers the volume and length specificities of each model, the predicted k_{eff} is closer to the same values for both models. For the lower channel emissivity, the original calculation has roughly the same slope as the partial calculations; however, for the higher channel emissivity, the original calculation has a much larger slope than either partial or full models. Comparing Figure 3-3 to Figure 3-4, the significance of increasing the channel emissivity can be seen. The higher channel emissivity leads to a significantly higher k_{eff} prediction, especially at higher temperatures due to the increased radiation heat transfer.

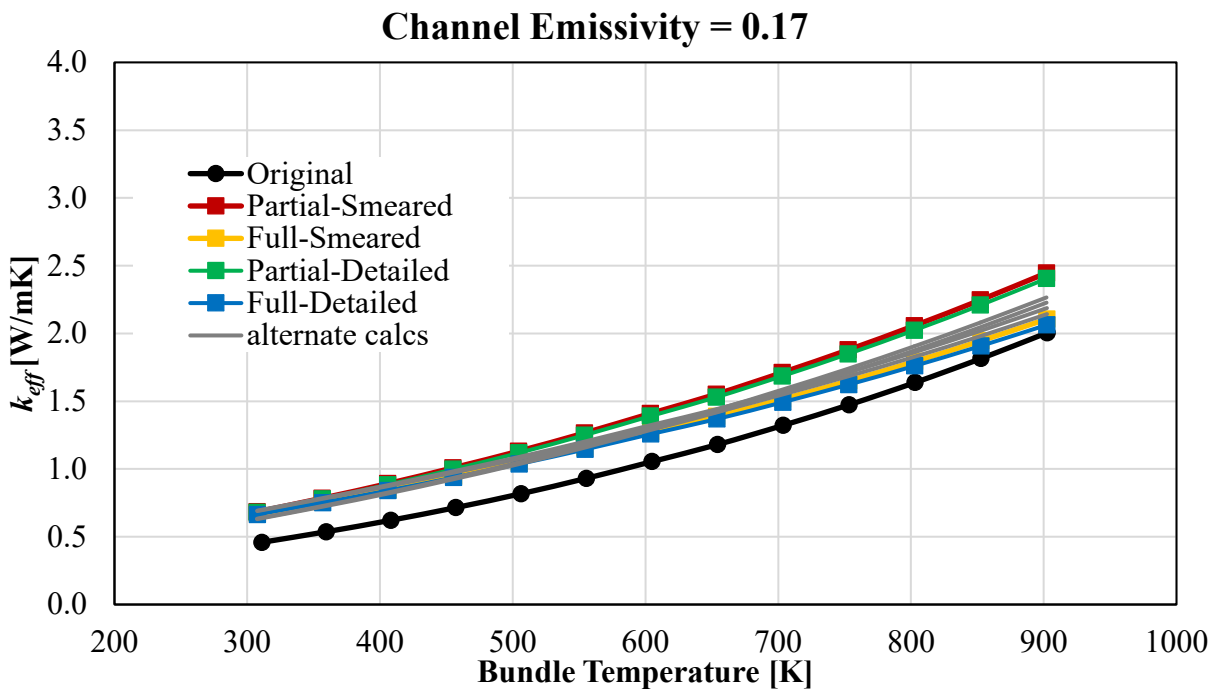

Figure 3-3. Effective thermal conductivities for the original calculation, each modeling type, and alternate calculations for channel emissivity = 0.17

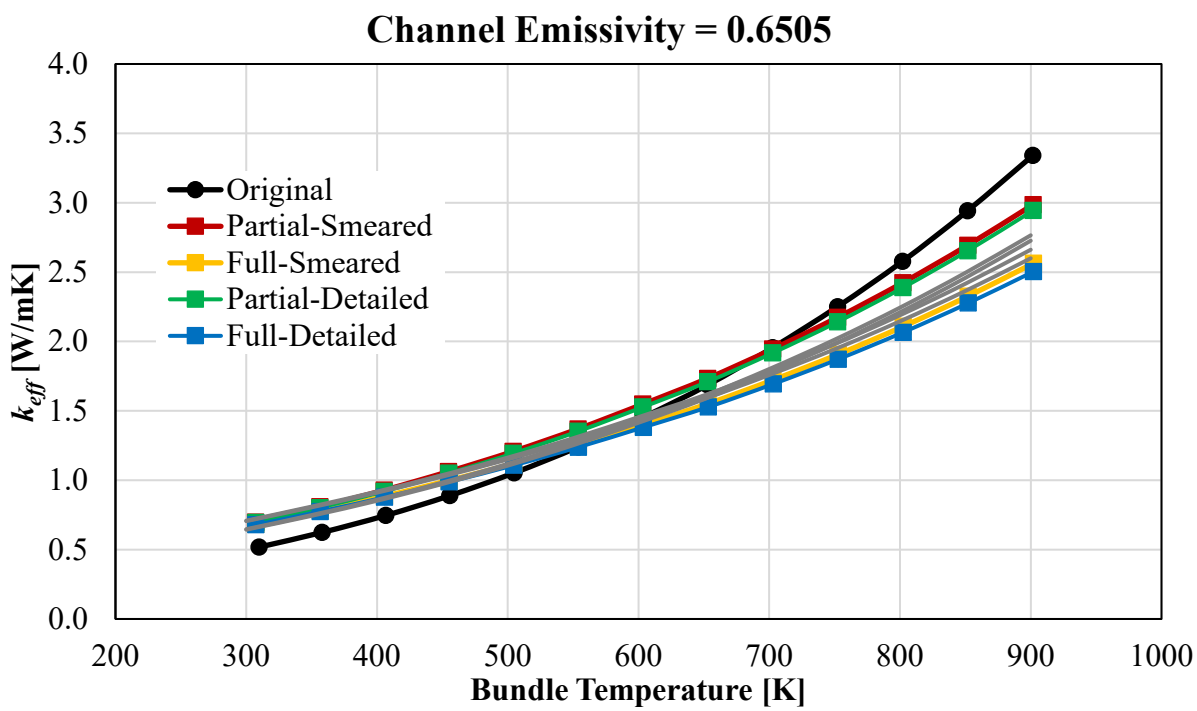

Figure 3-4. Effective thermal conductivities for the original calculation, each modeling type, and alternate calculations for channel emissivity = 0.6505

Figure 3-3 and Figure 3-4 also depict clear differences between the original calculation and these modeling techniques. To understand the differences between the original calculation and the

ANSYS/Fluent calculations, the additional modeling techniques to mimic the original STAR-CCM+ calculation were tested. The k_{eff} calculated by these models is shown in Figure 3-5 and Figure 3-6 with comparisons with the original, Partial-Detailed model and its alternate calculation for channel emissivities of 0.17 and 0.6505, respectively.

Figure 3-5 shows that the Partial-Long-Smeared-NoCladding model has the best agreement with the original calculation for a channel emissivity of 0.17, but Figure 3-6 shows that the Partial-Smeared-NoCladding model has the best agreement with the original calculation for a channel emissivity of 0.6505. Neither adjustment to the models gives perfect agreement with the original calculation, but they are significantly more similar to the original calculation than the Partial-Detailed model.

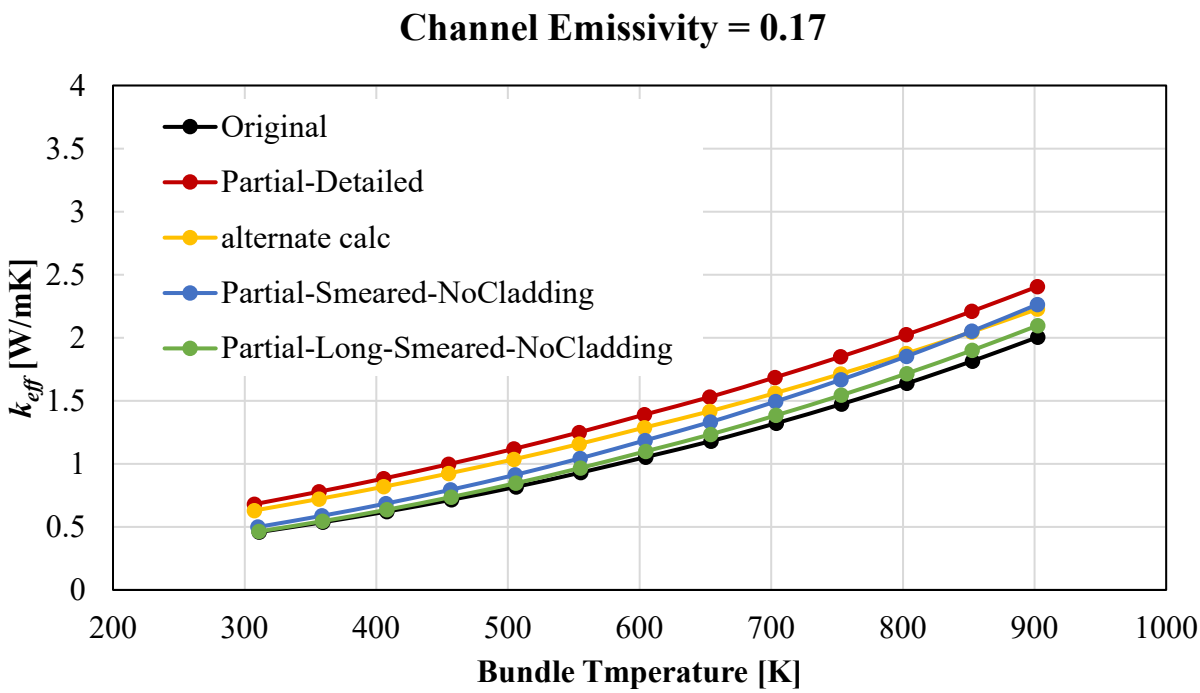

Figure 3-5. Effective thermal conductivity for modeling techniques replicating STAR-CCM+ modeling for channel emissivity = 0.17

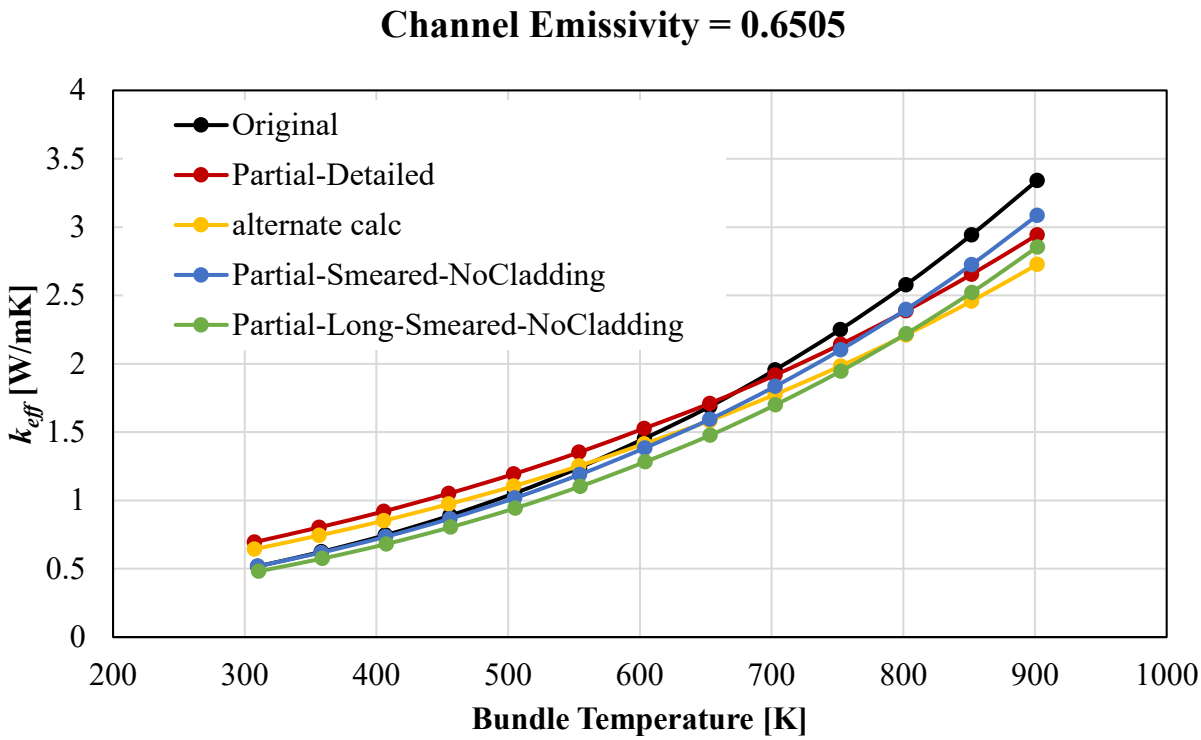

Figure 3-6. Effective thermal conductivity for modeling techniques replicating STAR-CCM+ modeling for channel emissivity = 0.6505

Since k_{eff} is more sensitive to small changes in PCT at higher wall temperatures, Figure 3-7 was generated to compare the PCT change from the original calculation for each model for both emissivities versus wall temperature. From this figure, we can see that PCT prediction for each of the models and emissivities gets closer to the original prediction at higher wall temperatures. All predictions, regardless of emissivity or model, are within one kelvin of the original prediction at a wall temperature of 900 K, despite the Partial-Detailed model at an emissivity of 0.17 predicting a PCT over 7 K lower than the original. One interesting result is that the Partial-Smeared and Partial-Long-Smeared models at alternate emissivities mirror each other across $\Delta PCT \approx 0.3$ K.

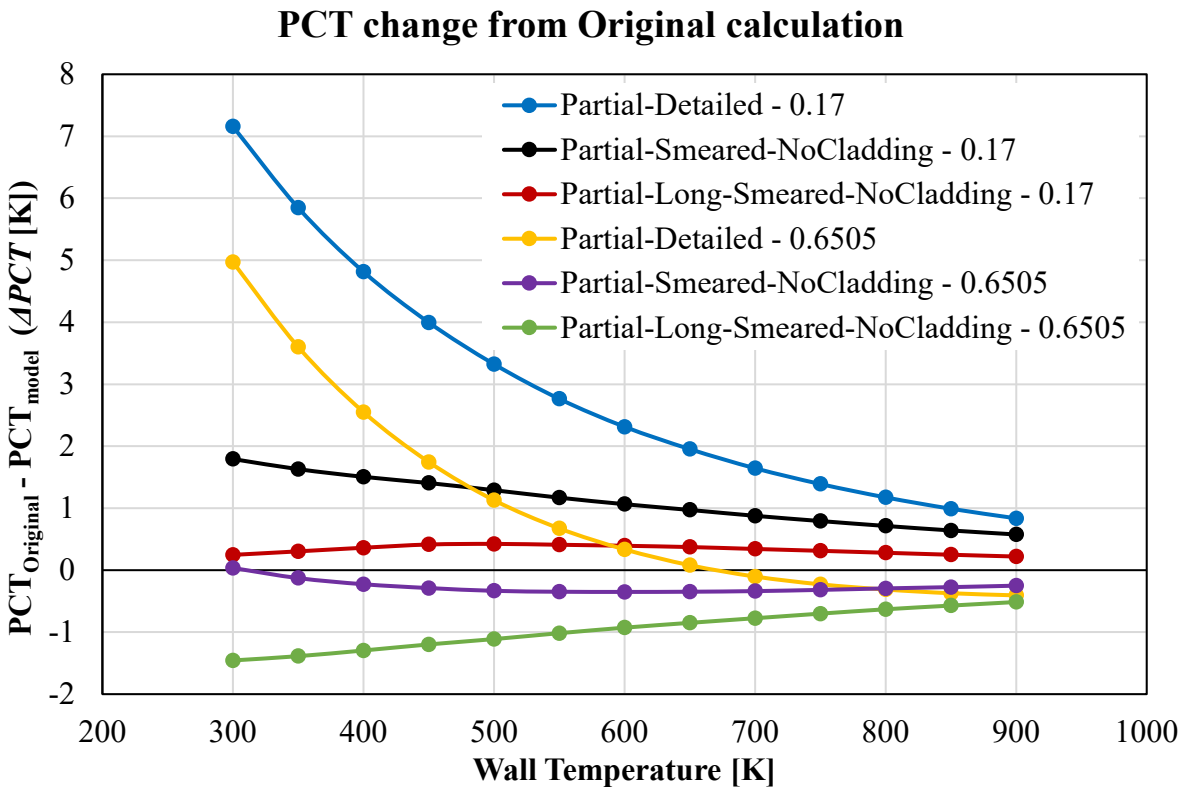

Figure 3-7. Peak cladding change for different modeling techniques from original k_{eff} calculation

These initial observations indicated that modeling the rods as either detailed or smeared had little effect on PCT prediction and in turn the k_{eff} calculation. The partial or full rod modeling did have a significant effect along with the channel emissivity. The full detailed model and the partial detailed model were chosen for the sensitivity studies and uncertainty quantification. This will allow some investigation into fuel pellet diameter and cladding thickness that isn't as straightforward with the smeared model.

3.4 Uncertainty Quantification

3.4.1 Error due to Iteration and Discretization

The first portion of analysis involves the consideration of error due to iteration and discretization. With strict convergence criteria combined with the monitoring of physical parameters, iterative error is negligible compared to discretization error. Convergence was considered when the energy residual was reduced to less than 10^{-10}. PCT was also monitored for steady state behavior.

For the mesh sensitivity study, four meshes were generated with coarse (13,040 elements), nominal (20,549 elements), fine (36,456 elements), and very fine (60,635 elements) meshes. Simulations were run to calculate the GCI on the PCT at each wall temperature (Oberkampf and Roy 2010). PCT was chosen as the parameter of interest because it is the direct output of the model and is subjected to the mesh sensitivities without distortion. The GCI is a measure of relative error due to spatial discretization. The GCI is defined as

$$GCI = \frac{F_S \varepsilon}{r^p - 1} \qquad \text{(Eq. 2)}$$

where F_s is the factor of safety, p is the order of convergence, and ε is the relative error, which is further defined as

$$\varepsilon = \frac{f_2 - f_1}{f_1}. \quad \text{(Eq. 3)}$$

f_1 is the PCT predicted by the finest mesh, while f_2 is the PCT predicted by the coarser meshes. The effective grid refinement ratio, r, is defined as

$$r = \left(\frac{N_1}{N_2}\right)^{1/D} \quad \text{(Eq. 4)}$$

where N_1 is the number of mesh elements in the finest mesh, N_2 is the number of elements in the coarser mesh, and D is the dimensionality of the system. To avoid artificially small error estimates, it's recommended that r exceeds 1.3 (Oberkampf and Roy, 2010).

For these simulations, $F_s = 1.25$, $p = 2$, and $D = 2$. Table 3-2 shows the GCI estimates for a wall temperature of 300 K. Figure 3-8 shows the results of these simulations and calculations for the coarse, nominal, and fine mesh at each wall temperature. The coarse mesh has much larger error at lower wall temperatures compared to the other meshes, but this error decreases quickly. There is a slight rebound in error at higher temperatures for the nominal and coarse meshes. The fine mesh has a consistently decreasing error as wall temperature increases. Overall, all spatial discretization errors are below 0.5 K with almost all errors below 0.2 K. This is approximately an order of magnitude below uncertainty resulting from cladding emissivity uncertainty and is therefore neglected in further efforts to calculate uncertainty.

Table 3-2. Associated calculations for GCI and estimated error for Tw = 300 K

Model	N_1	N_2	f_1	f_2	r	ε	GCI	Error [K]
Coarse	60635	13040	430.04	431.43	2.16	0.003233	0.001107	0.478
Nominal	60635	20549	430.04	430.67	1.72	0.001462	0.000501	0.216
Fine	60635	36456	430.04	430.38	1.29	0.000794	0.000272	0.117

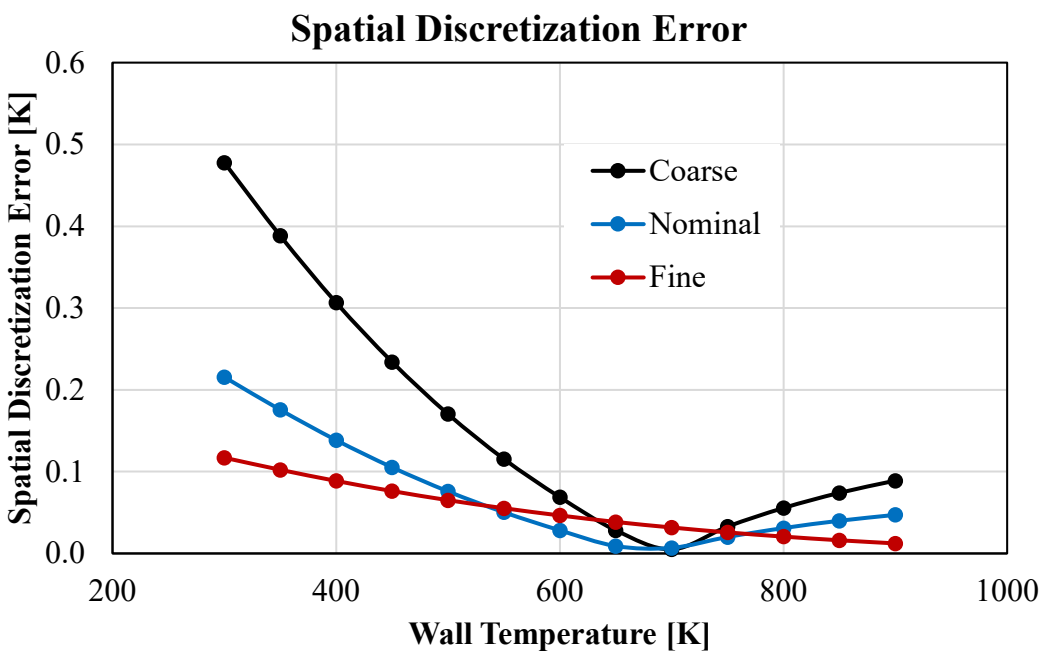

Figure 3-8. Error due to spatial discretization for three different meshes as calculated by the GCI

3.4.2 Rod and Cladding Thickness Tolerancing

Rod and cladding tolerancing was investigated for its effect on the k_{eff} calculations. The true tolerances of these Incoloy rods were not provided, but tolerancing for typical fuel rods and cladding is extremely tight. For this investigation, the 3σ manufacturing uncertainties of the fuel rods from the PB-2 BWR were found with the fuel radius and cladding thickness within 0.013 mm and 0.04 mm, respectively (Ivanov 2013). While the uncertainty for the PB-2 rods is assumed to be normally distributed, continuous distributions would have required remeshing for each run, which was not compatible with the ANSYS Workbench.[a] Thus, two other combinations of rod and cladding dimensions were chosen. A big model used the nominal fuel pellet diameter + 3σ and the nominal fuel cladding thickness + 3σ. The water rod also had tolerancing that maximized its area by reducing its inner diameter (nominal − 3σ) and increasing its outer diameter (nominal + 3σ). This increased the solid fraction of the assembly while decreasing the volumetric heat generation rate due to an increase in fuel pellet area. A little model was created by doing the opposite: minimizing the fuel volume (nominal pellet diameter − 3σ) and minimizing solid area (nominal cladding thickness − 3σ, nominal water rod inner diameter + 3σ, nominal water rod outer diameter − 3σ). This caused a PCT difference of 2.2 K between the big and little models at a wall temperature of 300 K, with that difference decreasing to 0.4 K at a wall temperature of 900 K. Figure 3-9 shows the k_{eff} profiles for each of the tolerancing models. No significant difference in k_{eff} is shown between the models because of the insensitivity to PCT changes at low wall temperatures, where the strongest effects of tolerancing are seen.

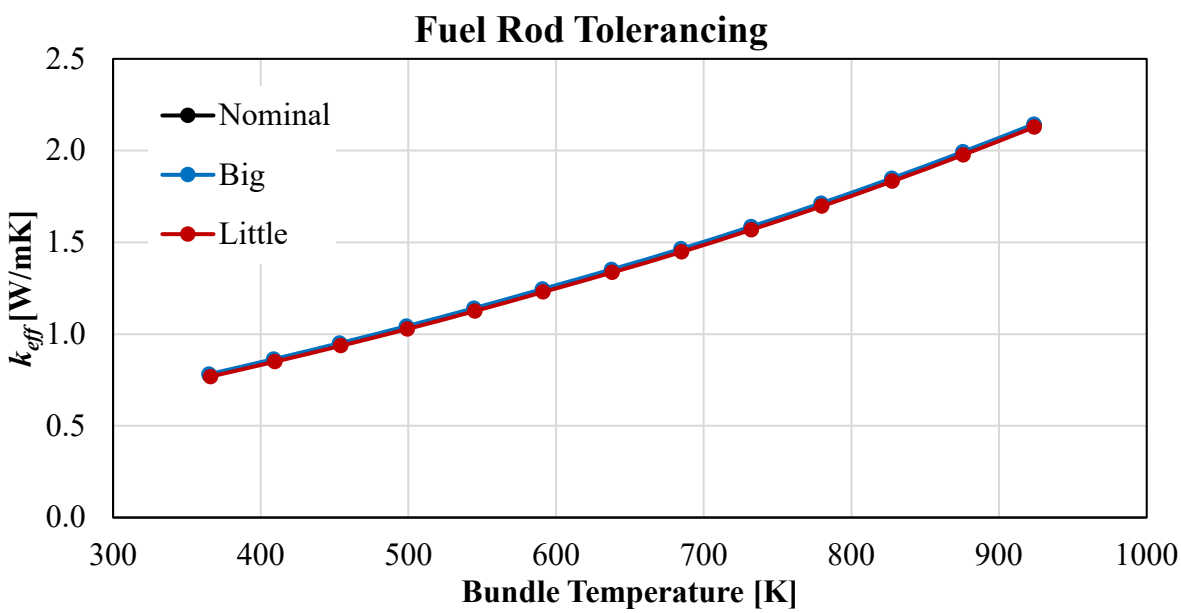

Figure 3-9. Fuel rod and cladding tolerancing effects on k_{eff}

[a] Possibly due to parallel nature of the runs.

3.4.3 Cladding Emissivity

The effect of cladding emissivity uncertainty was investigated. For the heater rod cladding in the DCS, the DCS handbook states that the Incoloy cladding is "pre-oxidized to a very dark color so an emissivity of 0.9 should be assumed" (Lindgren and Durbin 2017). The emissivity of spent fuel cladding is oftentimes modeled with an emissivity of 0.8 regardless of the specific alloy. Experimental data compiled for the creation of an emissivity prediction code indicates a slight temperature dependence, but a much larger range from approximately 0.6 to 0.95 fuel emissivity . For these sensitivity studies, emissivities 0.6, 0.8, 0.9, and 0.98 were investigated. Figure 3-10 shows the results from these simulations. The k_{eff} profiles show larger sensitivity to cladding emissivity at higher temperatures and lower emissivities leading to lower k_{eff} predictions, as expected. Because of the higher-than-usual assumed nominal emissivity, the uncertainty is assumed to capture values of cladding emissivity between 0.7 and 0.98 for the uncertainty calculation.

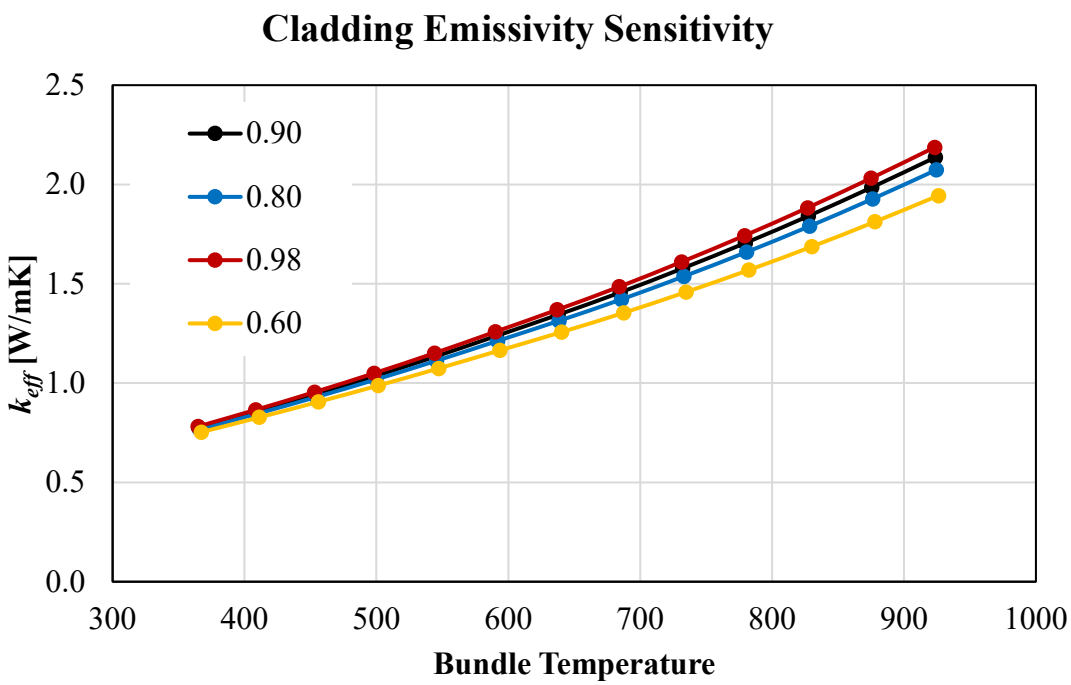

Figure 3-10. Fuel rod cladding emissivity effects on k_{eff}

3.4.4 Channel Emissivity

Figure 3-3 through Figure 3-6 show the significant effects of channel emissivity on k_{eff} for channel and water rod emissivities of 0.17 and 0.6505. The curves display significantly different behavior with the higher emissivity leading to steeper slopes for the curve. Based on these k_{eff} profiles and available experimental data, each elevation will have a unique range of channel emissivity values to sample.

3.5 Effective Thermal Conductivity and Uncertainty Calculations

The effective thermal conductivity and its uncertainty were calculated. Uncertainty due to rod and cladding thickness tolerancing, cladding emissivity, and channel emissivity were used to calculate the resulting k_{eff} uncertainty. A uniform distribution was assumed for each of the parameters. The channel and cladding emissivity were perturbed byusing the standard, continuous distribution associated with LHS sampling in Dakota. The cladding and fuel rod volume required discrete sampling, so the nominal, big, and little sizes previously described were used. Fourteen different k_{eff} curves were generated, associated with the experimental data for the channel emissivity. The channel emissivity sampling bounds were

between the highest and lowest measured emissivities for elevations with multiple measurements. For elevations with only one measurement, the average of the range of measurements of the two adjacent elevations were used to create the bounds centered around the single measurement, as shown in Table 3-1. The k_{eff} curve isn't dependent on heat generation, but the heat generation of 5kW was chosen as that is also the full DCS case being investigated. To create a reasonable curve, four wall temperatures were used for sampling: 300 K, 500 K, 700 K, and 900 K. For each wall temperature, 15 simulations were run with 5 simulations from each tolerancing size. Overall, 60 simulations at each elevation were run, for a total of 840 Fluent simulations.

The channel emissivity, cladding emissivity, and fuel size inputs for the runs were generated in Dakota using the LHS method. The fuel size (which is due to fuel and cladding tolerance) was then replaced with the discrete values. The parameter values were entered into Fluent and run until convergence was reached. The PCT outputs from Fluent for each height and wall temperature were entered into Dakota. Dakota ran the statistics on the PCT at each wall temperature and height and generated an average and standard deviation, σ. The average $\pm 2\sigma$ (95% confidence interval) was used for the upper and lower bounds of uncertainty. Eq. 1 was then used to calculate the average k_{eff} at each of the four temperatures for the average, upper bound, and lower bound PCTs, creating three k_{eff} curves for each height, as shown in Figure 3-11.

A few features are made evident in Figure 3-11. First, the k_{eff} uncertainty is temperature dependent and increases with increasing bundle temperature. Additionally, just as the k_{eff} is sensitive to elevation (due to changing channel box emissivity), so is its uncertainty. Table 3-3 contains the polynomials for the curve-fit of the k_{eff} curves. It also describes the bounds of the elevations for which the polynomials were implemented. Table 3-4 describes the upper and lower values of uncertainty for each of the curves as a function of average bundle temperature.

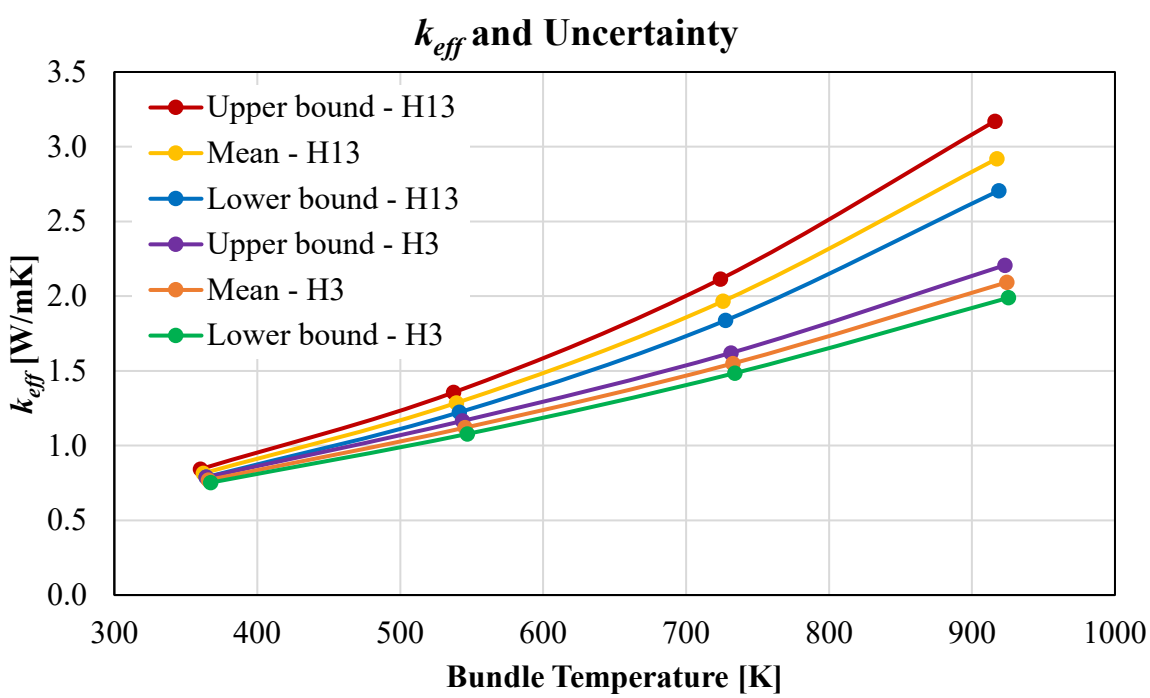

Figure 3-11. k_{eff} curves for two heights and their upper and lower uncertainty bounds

Table 3-3. Curve-fit polynomials for k_{eff} calculated at each height with the elevations the polynomial was implemented between in the DCS model

			Coefficients		
Name	Elevations (m)		z2	z1	z0
H1	0	0.1524	1.134E-06	9.993E-04	1.300E-01
H2	0.1524	0.4572	1.080E-06	1.053E-03	1.160E-01
H3	0.4572	0.762	1.118E-06	1.008E-03	1.291E-01
H4	0.762	1.0668	1.148E-06	9.882E-04	1.322E-01
H5	1.0668	1.3716	1.293E-06	8.852E-04	1.526E-01
H6	1.3716	1.6764	1.574E-06	6.561E-04	2.038E-01
H7	1.6764	1.9812	1.877E-06	4.474E-04	2.435E-01
H8	1.9812	2.286	1.910E-06	4.277E-04	2.468E-01
H9	2.286	2.5908	2.101E-06	3.146E-04	2.647E-01
H10	2.5908	2.8956	3.078E-06	−1.457E-04	3.227E-01
H11	2.8956	3.2004	3.194E-06	−2.331E-04	3.400E-01
H12	3.2004	3.5052	3.234E-06	−2.702E-04	3.504E-01
H13	3.5052	3.81	3.178E-06	−2.050E-04	3.326E-01
H14	3.81	3.9624	2.933E-06	−6.319E-05	3.107E-01

Table 3-4. Uncertainty percentages for each keff polynomial as a function of average bundle temperature.

	Lower Uncertainty (%)				Upper Uncertainty (%)			
	Average Bundle Temperature (K)				Average Bundle Temperature (K)			
Name	364	543	730	921	364	543	730	921
H1	1.93	3.65	4.58	5.61	1.86	3.40	4.19	5.05
H2	2.31	3.42	4.48	5.79	2.21	3.20	4.11	5.19
H3	2.41	4.01	4.55	5.48	2.30	3.72	4.17	4.94
H4	2.03	3.53	4.45	5.40	1.95	3.30	4.09	4.87
H5	2.35	3.43	4.78	5.73	2.24	3.21	4.36	5.14
H6	1.79	3.03	4.87	6.10	1.73	2.85	4.44	5.44
H7	2.52	3.85	5.02	6.78	2.40	3.57	4.57	5.97
H8	1.75	4.02	6.03	6.73	1.69	3.72	5.38	5.93
H9	2.42	3.75	6.02	7.14	2.31	3.49	5.37	6.25
H10	3.00	5.34	6.97	8.62	2.83	4.82	6.12	7.35
H11	3.41	5.04	6.80	8.37	3.19	4.58	5.99	7.17
H12	2.85	5.32	7.05	8.75	2.70	4.81	6.18	7.45
H13	3.38	5.42	7.52	8.60	3.17	4.89	6.54	7.34
H14	2.49	5.43	7.16	8.21	2.37	4.90	6.26	7.05

3.6 Predicted PCT and Uncertainty

The polynomials that describe k_{eff} in the 3-D, porous STAR-CCM+ DCS model used in previous uncertainty investigations was adjusted to match Table 3-2 (Suffield 2020a, 2020b). Because Dakota perturbs within a constant range, a constant value of uncertainty must be chosen, despite the knowledge that it is elevation and temperature dependent. Table 3-4 lists an upper value of 7.52%, corresponding to the maximum uncertainty for an average bundle temperature of 730 K. It was chosen because it encompasses the PCT and is a bounding uncertainty value. For each simulation, a value for uncertainty will be chosen below that value, with either a normal or uniform distribution, so it is a reasonable upper bound.

As with previous work, the 5 kW and 800 kPa internal pressure case for the DCS was investigated. Experimental uncertainties were used for power, ambient temperature, and helium pressure (Lindgren and Durbin 2017). The axial porous viscous coefficient and the emissivity of carbon steel were assumed (Suffield et al. 2020a). An LHS method with 250 samples was conducted within the uncertainty bounds of each parameter. The sampling was run for both normal and unform distributions of uncertainty. The PCT was used as the response parameter and Dakota calculated the mean and standard deviation. Figure 3-12 shows the probability distribution function (PDF) calculated using the mean and standard deviations of the results from previous work, results from the updated k_{eff} and its uncertainty, along with the experimental results and their uncertainty. No significant changes are seen between the results from previous work and the current results, indicating that the previously used k_{eff} and its uncertainty were approximated with sufficient detail in addition to giving confidence to the current work.

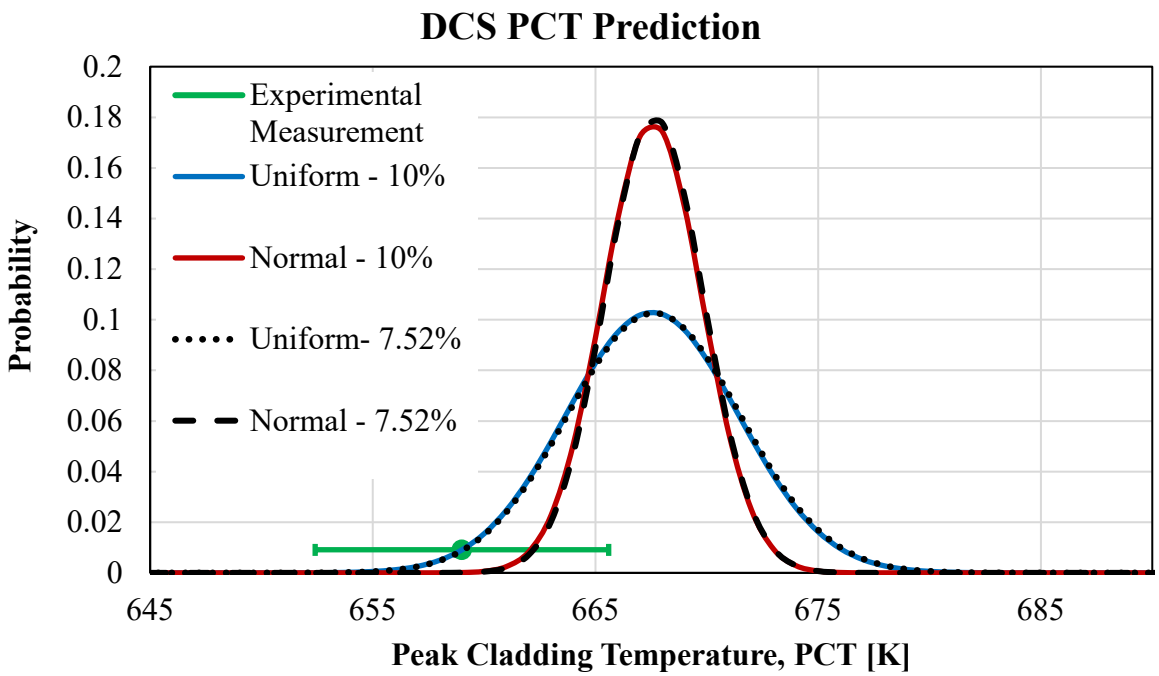

Figure 3-12. PDFs from previous work and current work with experimental measurement of the PCT

3.7 Key Results

The radial k_{eff} and its uncertainty of the fuel region in the DCS were investigated. Previous work indicated that the radial k_{eff} is a sensitive parameter to predict PCT. To calculate the k_{eff} and its uncertainty, detailed 2-D models of the fuel assembly were created in ANSYS Fluent. Different modeling techniques were

investigated for their impact on PCT and k_{eff}, and differences between previous profiles and current profiles were investigated. Next, convergence and discretization errors were estimated. Sensitivity studies for the impact of fuel and cladding tolerancing, channel emissivity, and cladding emissivity on k_{eff} were conducted. Profiles for k_{eff} and its uncertainty were created at the 14 axial locations of experimental channel emissivity data. These results showed that the k_{eff} and its uncertainty are elevation dependent (due to the elevation dependent channel box emissivity and partial rods) as well as temperature dependent. Finally, these k_{eff} profiles and a constant value of uncertainty were implemented in the DCS model, along with previously determined uncertainties, to estimate PCT uncertainty in the DCS for comparison with experimental data. The results of DCS PCT prediction showed no significant changes with previous results, which are in good agreement with experimental results when experimental uncertainty is considered.

This page is intentionally left blank.

4. SENSITIVITY ANALYSES FOR HIGH BURNUP DEMONSTRATION

The SFWST research and development program of the Department of Energy (DOE) is conducting an HBU fuel storage demonstration for a storage module in the North Anna Nuclear Power Station's Independent Spent Fuel Storage Installation (ISFSI). The storage module selected for this demonstration was an Orano TN-32B cask. The main goals of this test are to provide confirmatory data for model validation and potential improvement, support license renewals and new licenses for ISFSIs, and support transportation licensing for HBU SNF (EPRI 2014). Initial test results are described in Waldrop (2019).

Measurements of fuel temperatures in the TN-32B cask were recorded continuously since thermocouple (TC) lances were first put in place while the cask was still full of water. Fuel temperatures and intermittent measurements of cask surface temperatures followed steps taken in the drying process, including cask draining, blowdowns, vacuum drying, and backfilling with helium. The cask was then kept in the decontamination bay for two weeks to allow time to reach thermal equilibrium. Measurements at that point were used for comparison with blind model predictions of fuel and cask surface temperatures from three participating organizations. Results of that round robin modelling effort are described in Csontos (2020). Pacific Northwest National Laboratory (PNNL) models used in that exercise are described in Fort et al. (2019a). PNNL also compared model predictions with fuel temperatures measured during the vacuum drying transient. That work is described in Fort et al. (2019b).

Sensitivity calculations are presented in this section for steady state and transient models of this cask. The steady state models were used to estimate the equilibrium temperature achieved during the two-week "thermal soak" in the decontamination bay. Sensitivity to input parameters for the steady state models are presented in Section 4.1. Transient calculations were used to estimate peak fuel temperatures reached during the vacuum drying process. Sensitivity studies for the transient models are presented in Section 4.3.

4.1 Steady State Models

The models used in this study were an updated version of those used in the initial round robin modeling exercise for the HBU demonstration (Csontos 2020). The international benchmark is a modeling activity organized by the Electric Power Research Institute (EPRI) Extended Storage Collaboration Program. The goal of this modeling activity was to produce estimates from a broader set of participants of the same fuel and cask surface temperatures in the initial round robin modeling exercise. However, in the international benchmark, participants were provided a non-proprietary description of the TN-32B cask along with a common set of inputs required to model the storage cask and conditions in the decontamination bay (Akkurt and Csontos 2020). The goal of the first phase of the international benchmark was to produce steady state temperature estimates using the prescribed inputs. A large number of participants submitted results using five different codes, and those results will be described in an upcoming EPRI report. Results for PNNL's contribution to that modeling activity are described in Fort et al. (2020). The next phase in the international benchmark will address sensitivity to model inputs. Initial work toward that effort plus investigation of additional parameters are described in this section.

Model results are presented for the two STAR-CCM+ models that were used in the original work: a detailed model that has an explicit representation of the fuel assemblies and a porous media model that represents each fuel assembly and surrounding gas as a homogenized mixture. A correction to the porous media model is described first. This is followed by a description of sensitivity results for both STAR-CCM+ models.

4.1.1 Updates to the Porous Media Model

Among the model inputs provided in the international benchmark problem statement are values for gap thicknesses between cask components. These gas-filled gaps result in thermal resistances that are important for estimating the maximum value and distribution of component temperatures. Initial

sensitivity runs with the STAR-CCM+ porous media model showed that the gap specified between the liner base and gamma shield was not working correctly. The result was that runs with this model used a much smaller gap than intended. This error was corrected so that the porous and detailed models both had equivalent gap interfaces at that location.

Before this correction, the gap set at the liner base was the same as the 0.001-inch gap used to represent the interference fit on the sides of the liner. The liner base gap specified in the problem statement was much larger, 0.125 inch. The interface error was included in the porous model results presented in Fort et al. (2020) and submitted to the international benchmark. This explains why the slope in the axial profiles of the fuel assembly lance temperatures in that report differed between the two STAR-CCM+ models. Figure 4-1 compares the explicit and corrected porous model results for the lance temperatures in hot basket location (cell 14, assembly 57A). The axial slope is now consistent. The magnitude of difference from measured values are also comparable.

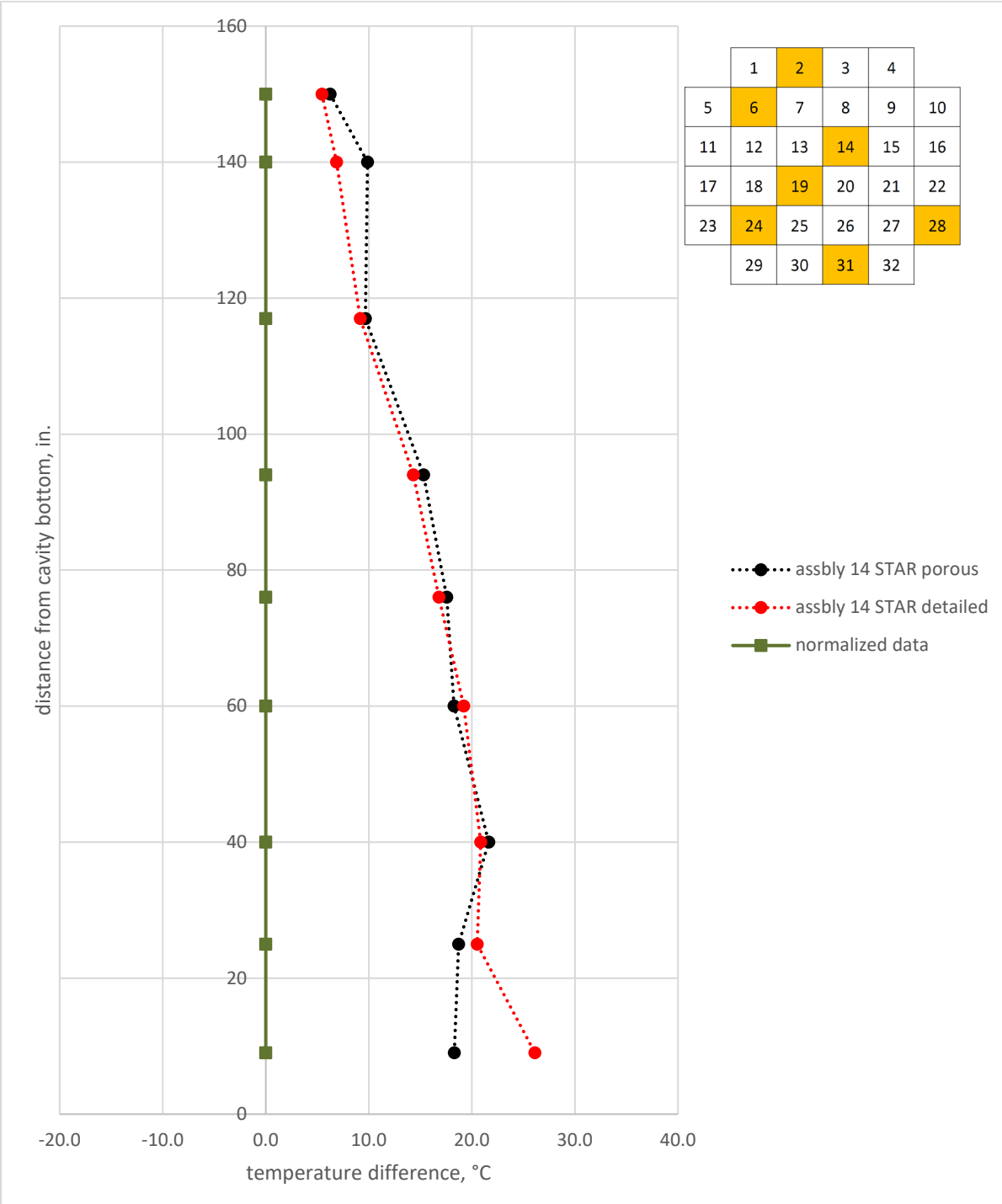

Figure 4-1. Difference between STAR-CCM+ model predictions and measurements of fuel temperatures for basket cell 14; 0.125-inch gap between liner base and gamma shield

Figure 4-2 compares the same Cell 14 profiles for the tight (0.001-inch) gap. Again, slopes are consistent between the two models. Note also that this parameter changed results in a profile that is closer to that of the measurements.

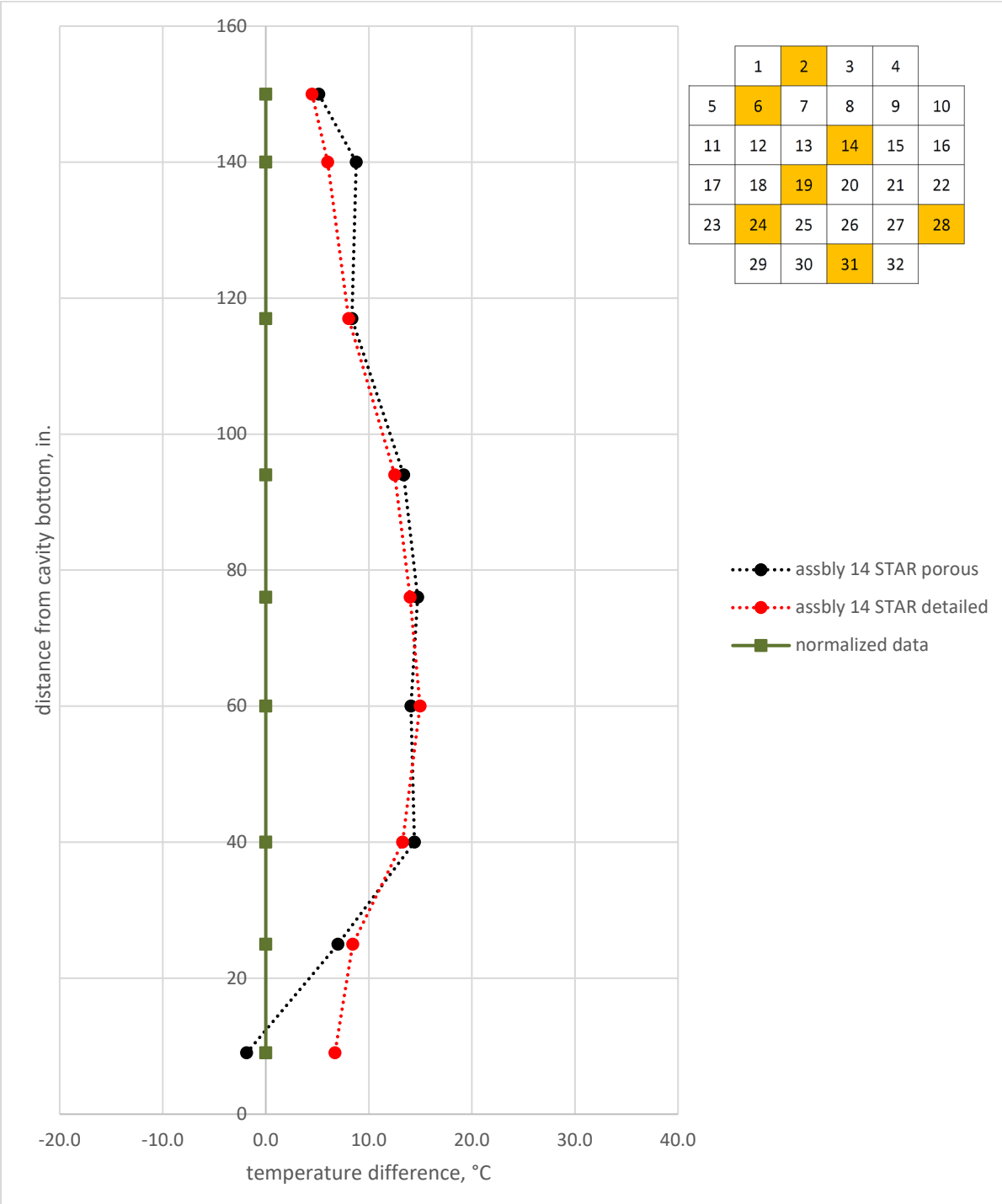

Figure 4-2. Difference between STAR-CCM+ model predictions and measurements of fuel temperatures for basket cell 14; 0.001-inch gap between liner base and gamma shield

Figure 4-3 compares porous and detailed model predictions for the other two TC lance positions represented in the 1/8th section detailed model. These are Cells 2 and 28, which are both on the outside of the basket. The differences does not agree as well for the porous model. Agreement may be expected to be better for the detailed model, except that these outer cells are only approximated in their locations in the 1/8th sector model. Decay heats of adjacent cells are not the same as they would be in their exact

location. A full 360° detailed model would be best, but apparently, the symmetry approximation works well in the current model. Based on the level of agreement between the corrected porous and explicit models, sensitivity studies were performed with the porous model alone to save time and computational resources.

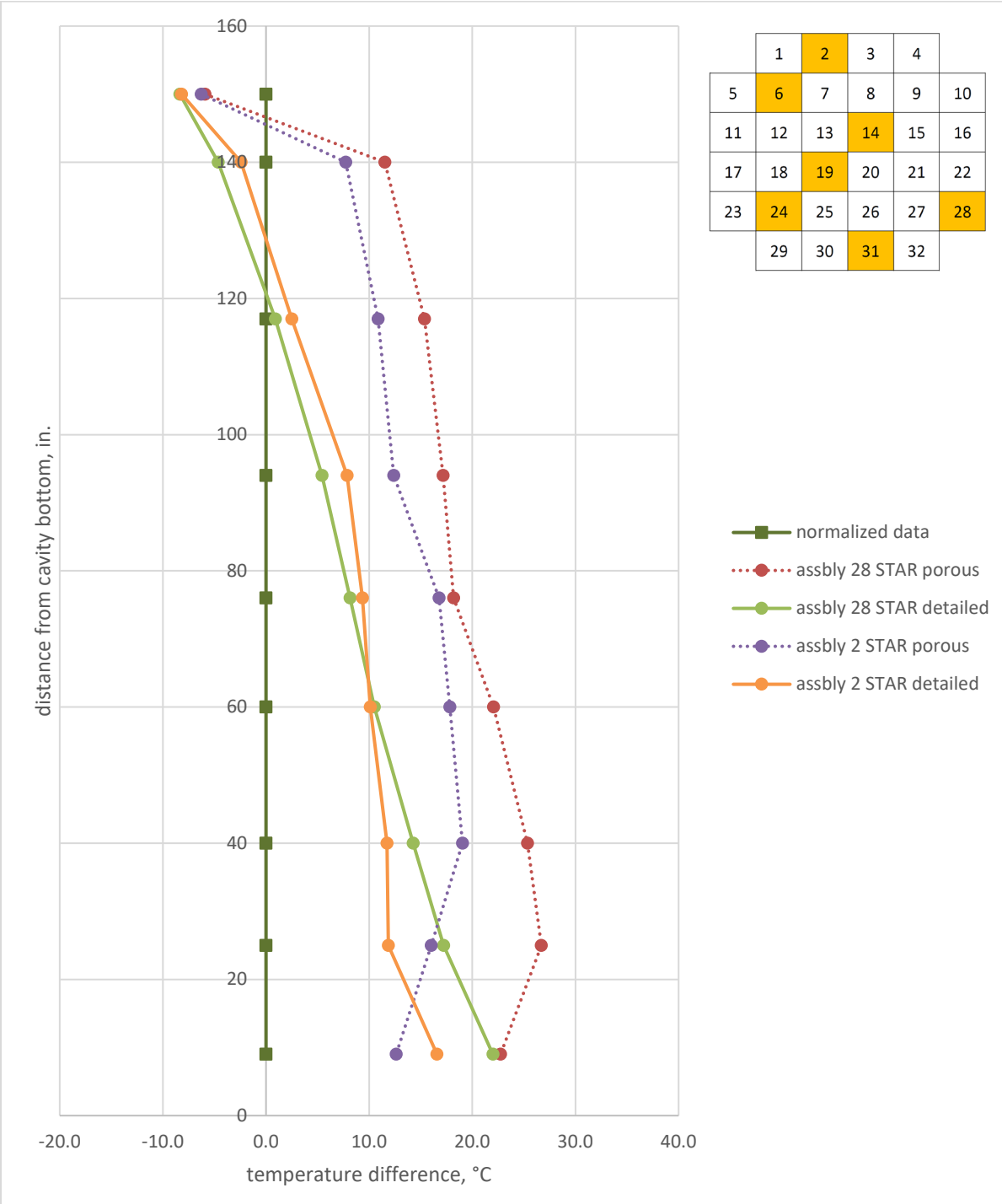

Figure 4-3. Difference between STAR-CCM+ model predictions and measurements of fuel temperatures for basket cells 2 and 28; 0.125-inch gap between liner base and gamma shield

4.1.2 Sensitivity Runs

Sensitivity runs were completed for a variety of model parameters. The list of cases is shown in Table 4-1 along with case identifiers used in plots. Parameters and values discussed for all Phase 2 participants are shown in bold font. Values specified for use in the International Benchmark problem description for all participants will be referred to as *baseline* parameter values.

Table 4-1. Sensitivity cases

case id	definition	parameter values
baseline	corrected porous benchmark	-
bg	gap between liner base and shield	**bgp, bgm** (0.125 +/− 0.025 in.); bg025 (0.025); bg001 (0.001)
amb	ambient temperature	**ambp, ambm** (75°F +/− 15°F) (23.9 °C +/− 8.3 °C)
rg	gap between transition rails and basket	**rgp, rgm** (0.1 +/− 0.05)
nsr	neutron shield resin thermal conductivity	nsrp (25% over baseline); nsr1 (6 × baseline)
nsg	gap between neutron shield box and gamma shield and between box and outer shell	nsg001 (0.001 in., which is 1/10 of value used in baseline model)
dh	decay heat	**dhp, dhm** (baseline +/− 5%)

Plotted results are shown in this section for each case for the TC lance positions in Cell 14 and for the "A" set of cask surface measurements, as defined in Figure 4-4. The choice of the hot basket cell is obvious. The "A" set of cask surface measurements was chosen for comparison as it includes measurements higher and lower on the cask that are beyond the extent of the neutron shield on the gamma shield itself.

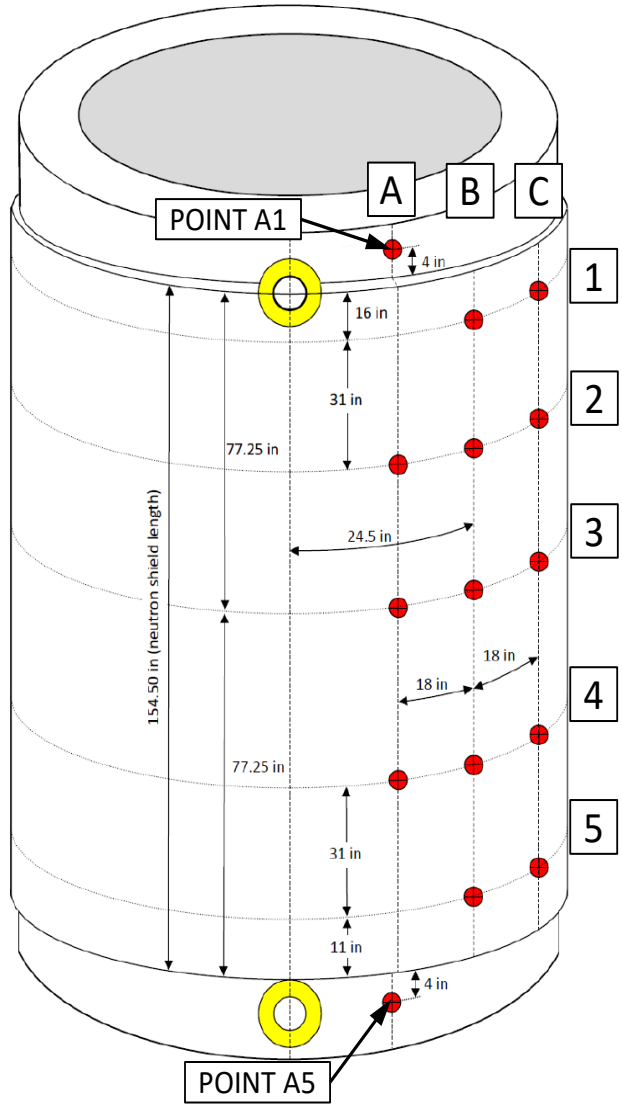

Figure 4-4. Definition of cask surface temperature measurement locations

4.1.2.1 Gap at Liner Base

The baseline gap between the liner base and gamma shield is conservatively set to 0.125 in. The difference between the predicted and measured temperatures at the Cell 14 TC lance positions is shown in Figure 4-5. The profile for the baseline model suggests insufficient heat transfer through the cask base. Reducing the gap at the liner base compensates for this. Note that the thermal boundary condition at the base of the cask is also a factor that should be considered in future runs.

The difference between predicted temperatures and the first row of measurements on the surface of the cask are shown in Figure 4-6. The bpm and bgp sensitivity results are not included in this plot as they are indistinguishable from the corrected baseline. While the base gap changes make a significant difference to axial temperatures within the fuel assemblies, they make little difference to surface temperatures.

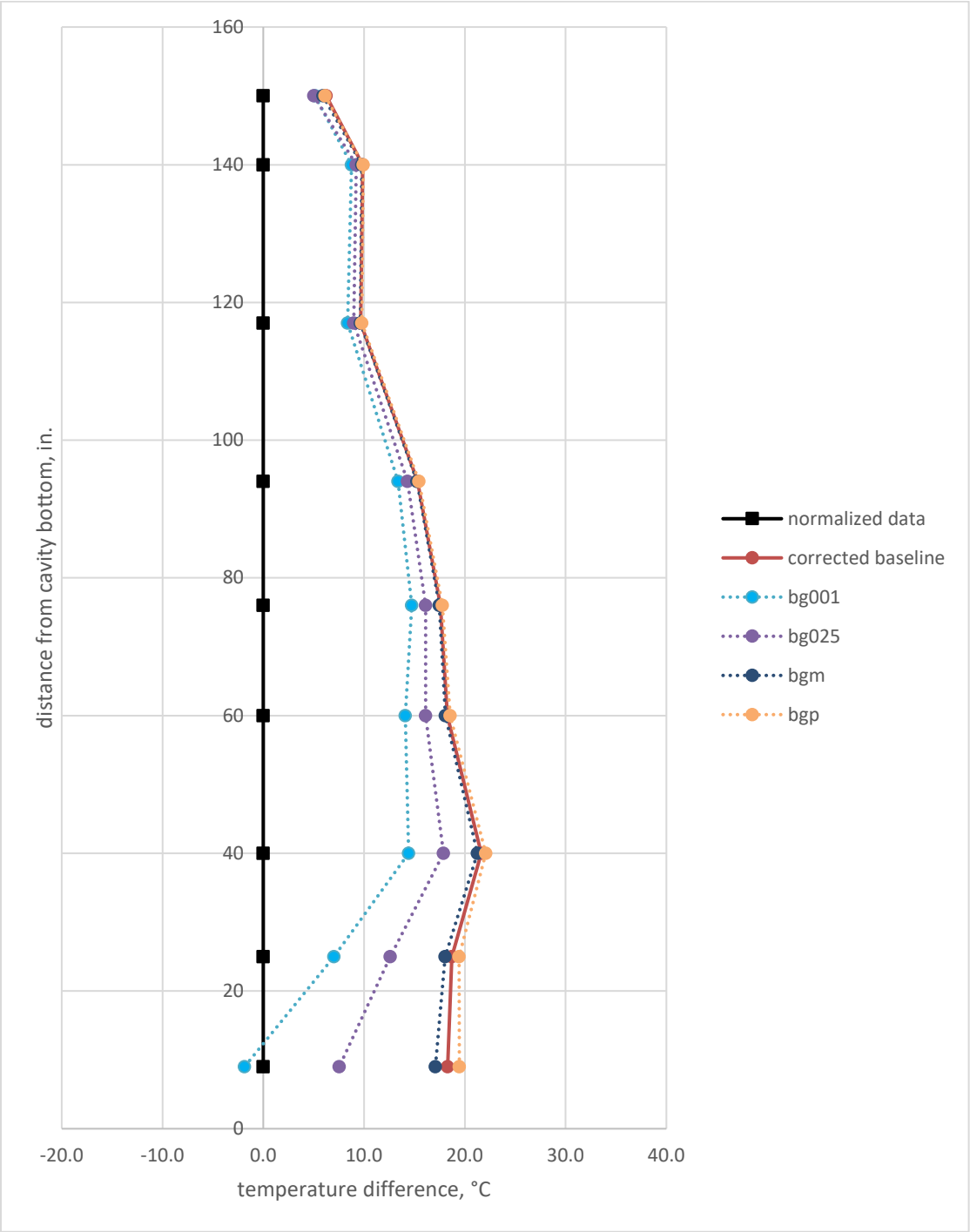

Figure 4-5. Difference between STAR-CCM+ porous model predictions and measurements of Cell 14 fuel temperatures for basket cells; sensitivity to gap between liner base and gamma shield

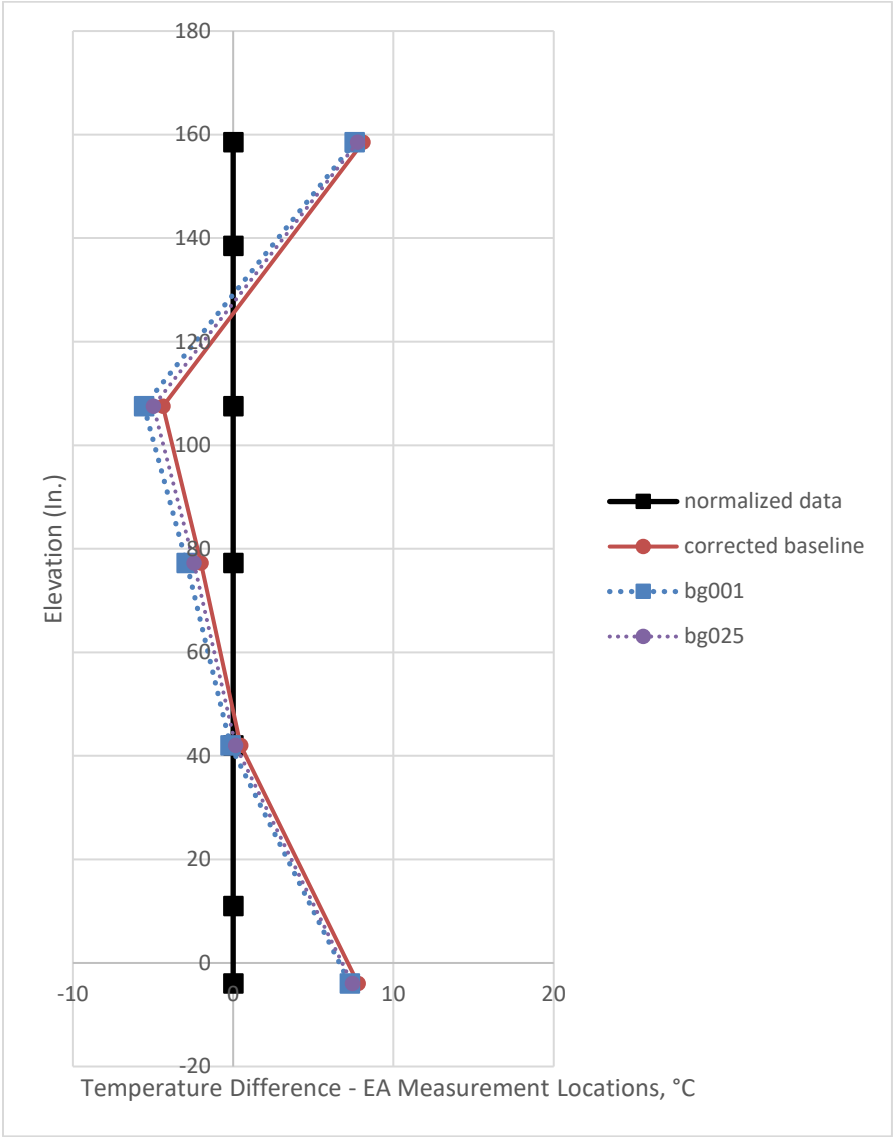

Figure 4-6. Difference between STAR-CCM+ porous model predictions and measurements of "A" cask surface temperatures for basket cells; sensitivity to gap between liner base and gamma shield

4.1.2.2 Thermal Radiation Included in Base Gap

As mentioned previously, inclusion of thermal radiation at this gap interface uses the field functions that PNNL developed. The calculation is based on the approximation for small gaps used in COBRA-SFS. Cell 14 lance temperature differences are shown in Figure 4-7. The addition of thermal radiation to the baseline gap thickness is shown to have about the same impact as reducing the gap thickness by 0.025 in. Although surface temperatures change little with base gap thickness, the change observed with base gap radiation is also about the same as with a base gap thickness reduction of 0.25 in.

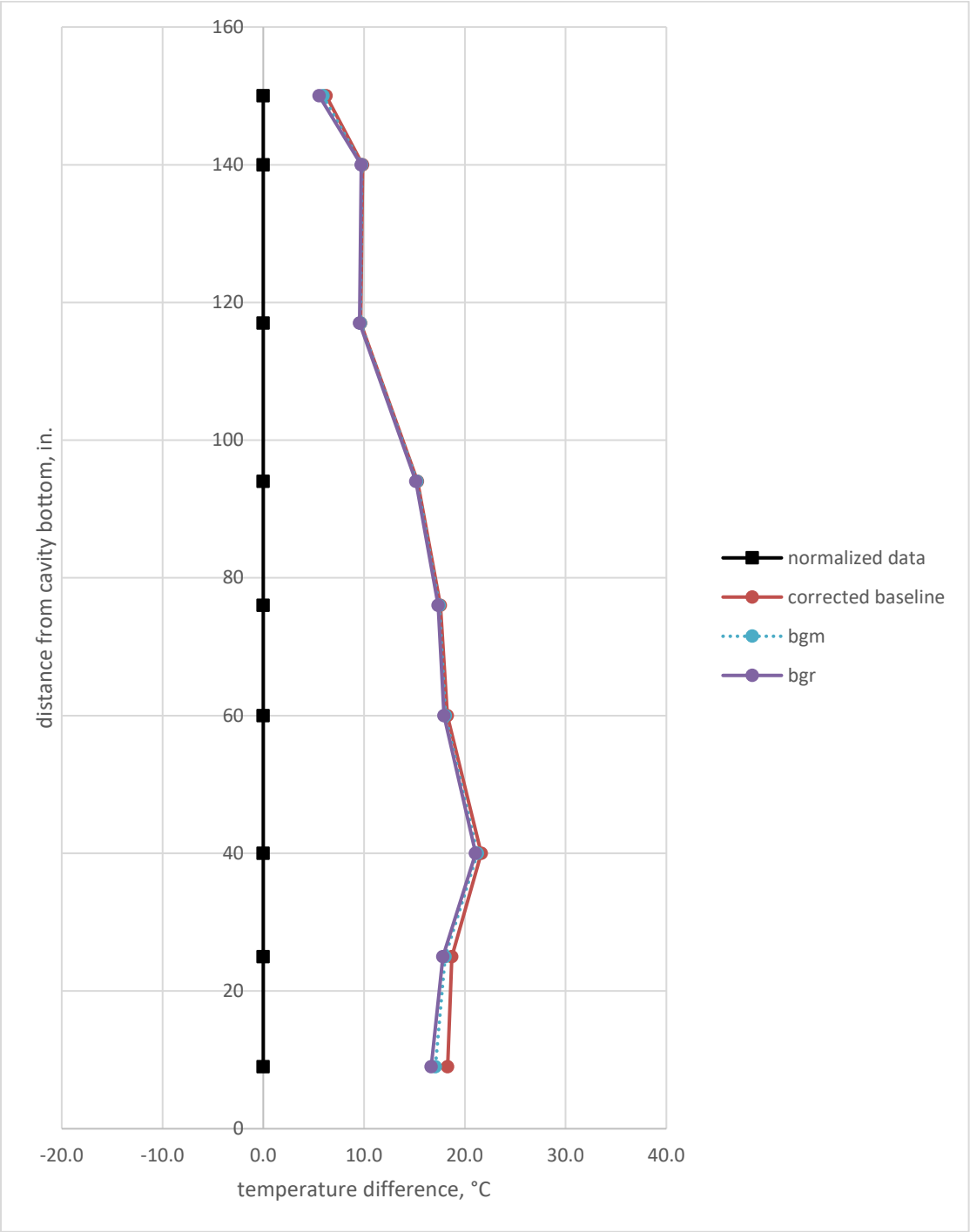

Figure 4-7. Difference between STAR-CCM+ porous model predictions and measurements of Cell 14 fuel temperatures for basket cells; sensitivity to inclusion of thermal radiation in gap between liner base and gamma shield

4.1.2.3 Ambient Temperature

Ambient temperature changes of +/− 15°F are expected to result in a significant change in cask temperatures, but is it "1 for 1"? Cell 14 fuel temperature differences for this case are shown in Figure 4-8 and cask surface temperature differences are shown in Figure 4-9. The magnitude of change in assembly

lance temperatures is visibly the same for all axial. The change is between 5°C and 6°C. For the cask surface temperatures, the positive and negative change is equal and consistently between 6°C and 7°C. But at none of these positions is it "one for one" with ambient temperature change.

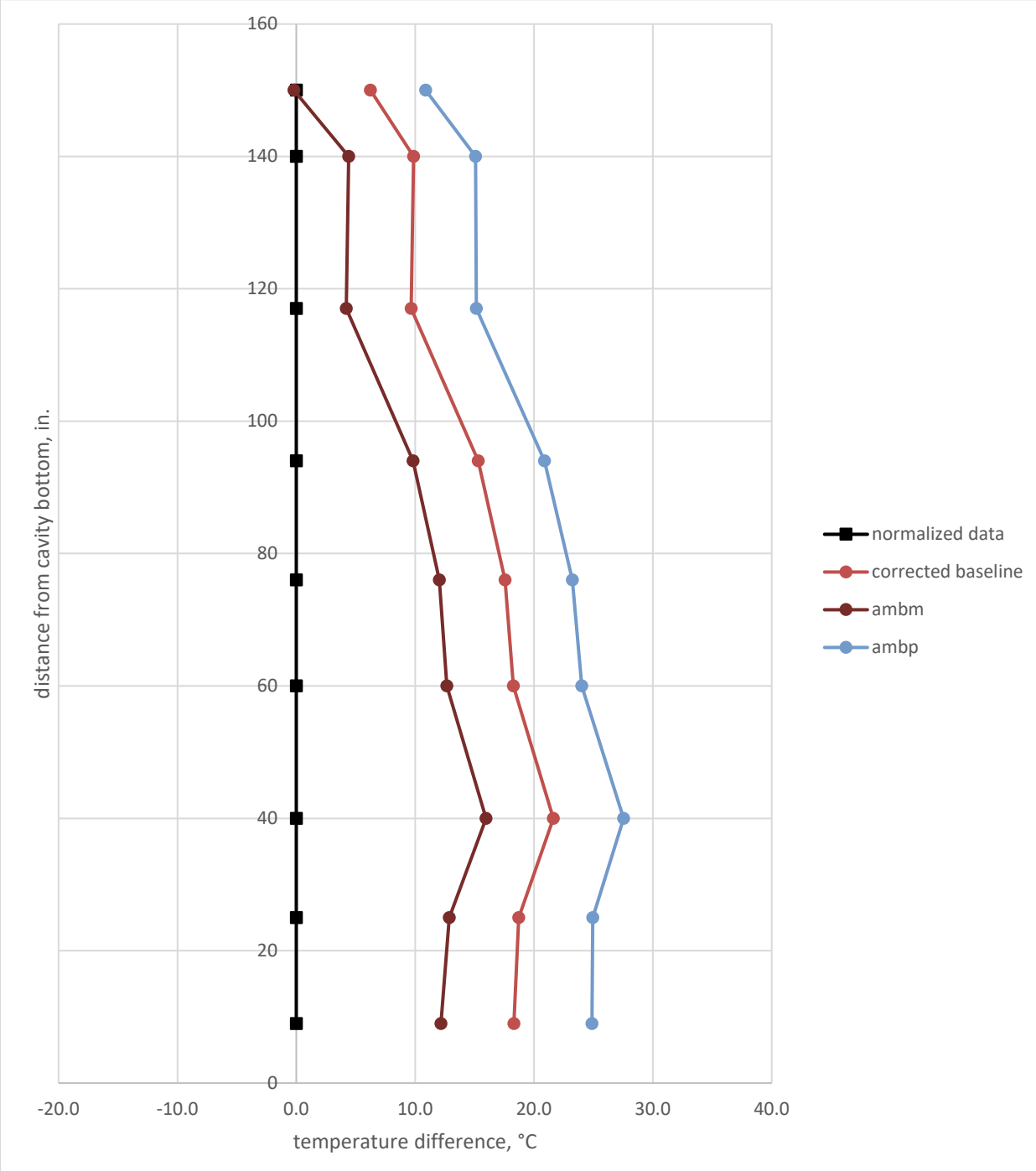

Figure 4-8. Difference between STAR-CCM+ porous model predictions and measurements of Cell 14 fuel temperatures for basket cells; sensitivity to ambient temperature

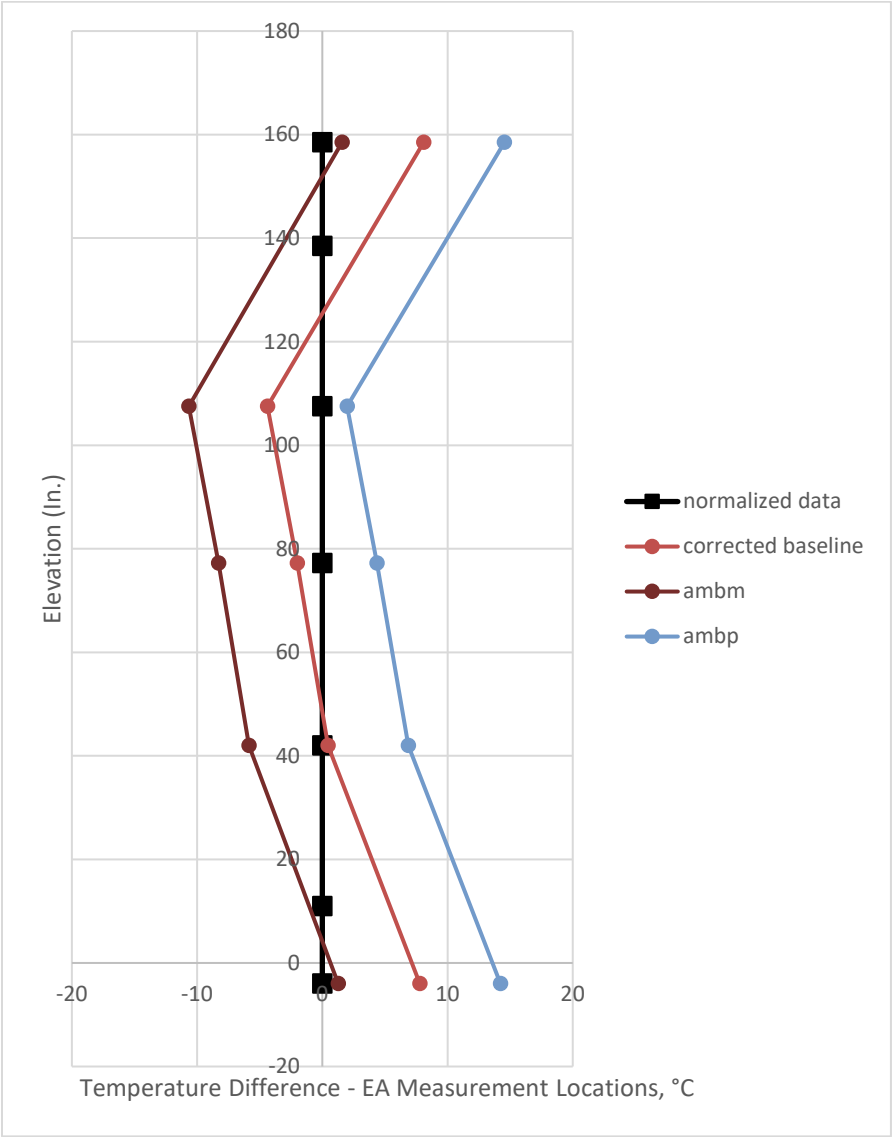

Figure 4-9. Difference between STAR-CCM+ porous model predictions and measurements of "A" cask surface temperatures for basket cells; sensitivity to ambient temperature

4.1.2.4 Gap Between Transition Rails and Basket

The impact of rail gap thickness changes of +/− 0.05 in. to the 0.1 in. base case is considered next. Cell 14 lance temperature differences are shown in Figure 4-10 and cask surface temperature differences are shown in Figure 4-11.

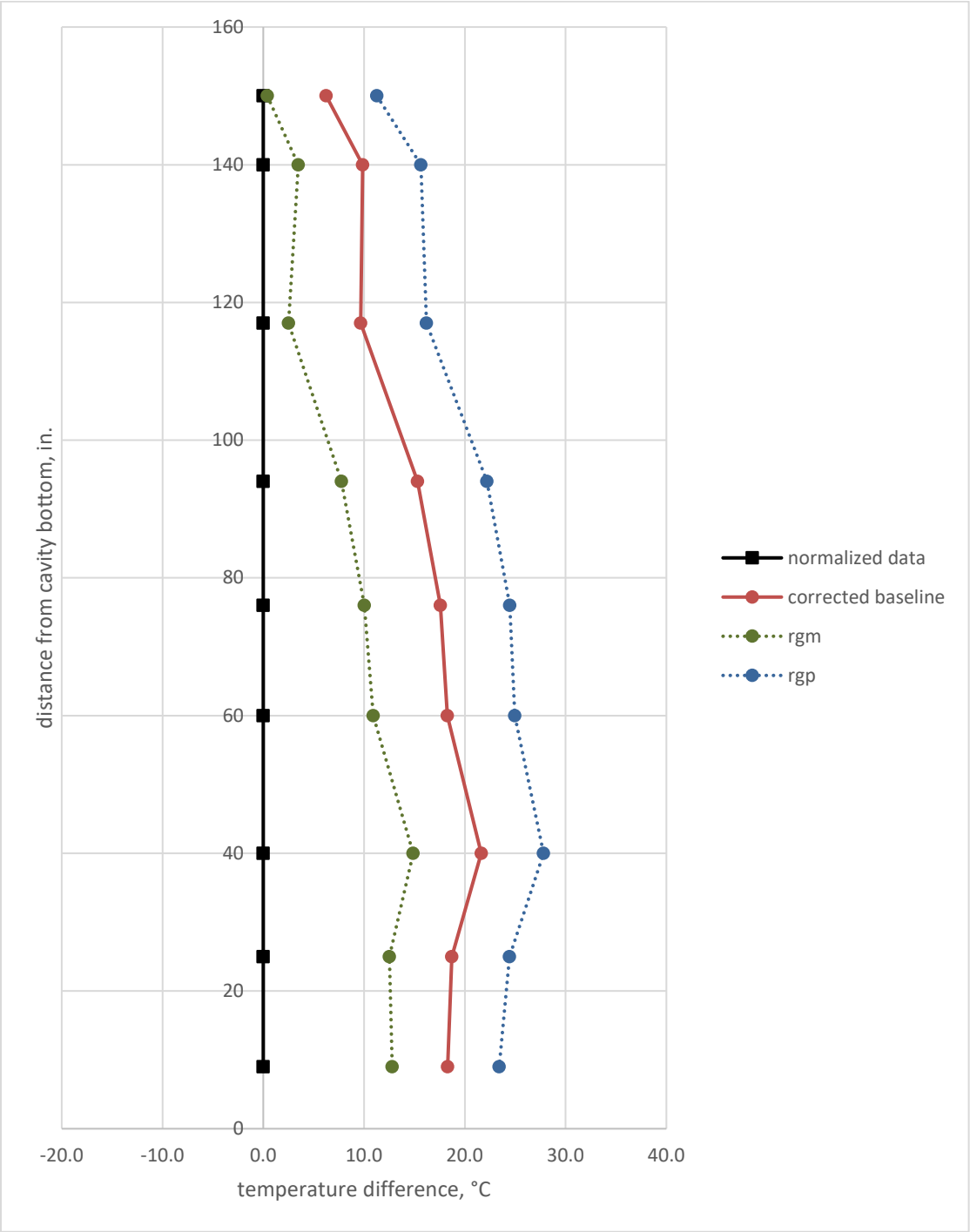

Figure 4-10. Difference between STAR-CCM+ porous model predictions and measurements of Cell 14 fuel temperatures for basket cells; sensitivity to gap resistance between basket and transition rails

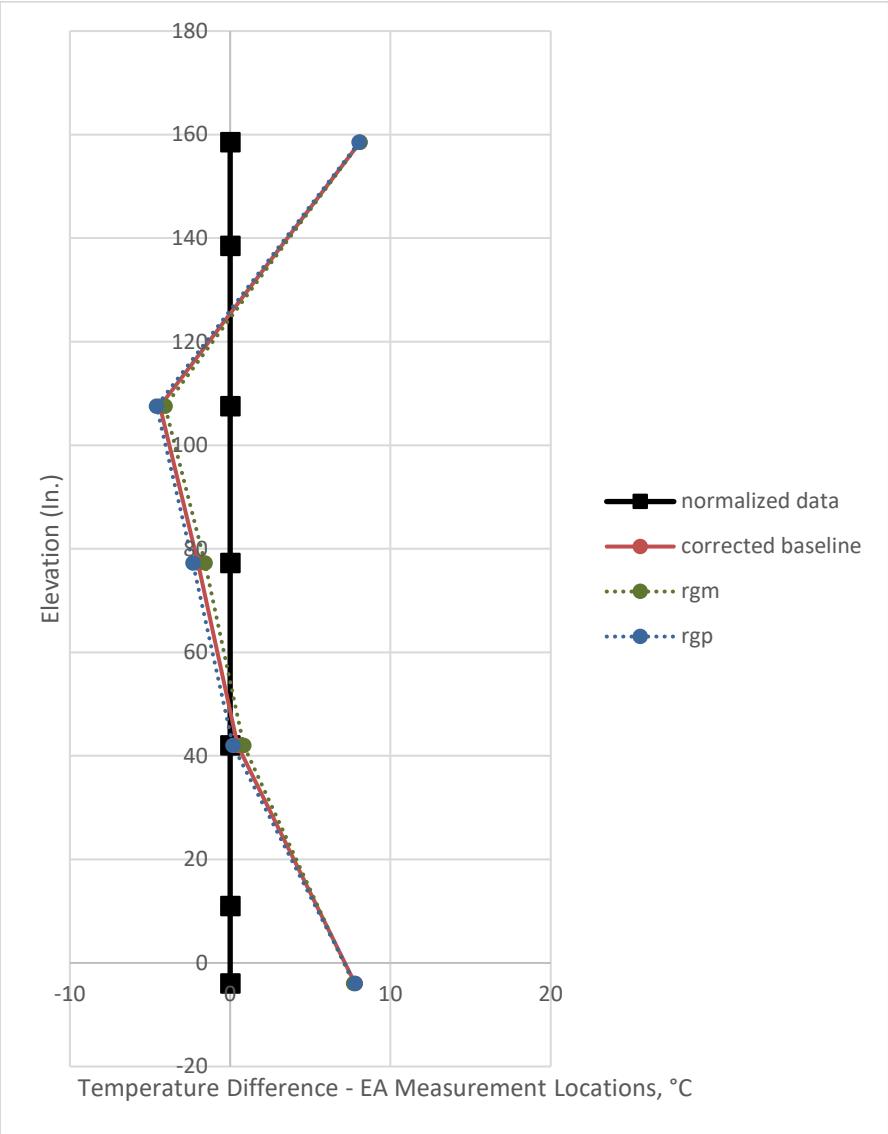

Figure 4-11. Difference between STAR-CCM+ porous model predictions and measurements of "A" cask surface temperatures for basket cells; sensitivity to gap resistance between basket and transition rails

4.1.2.5 Decay Heat

Decay heat changes of +/− 5% resulted in significant changes in cask temperatures. Cell 14 lance temperature differences are shown in Figure 4-12 and cask surface temperature differences are shown in Figure 4-13. A 5% change in decay heat is shown to have a very large impact on fuel temperatures in comparison with the 15°F change in ambient temperature. The change in decay heat produced less impact on the cask surface temperatures.

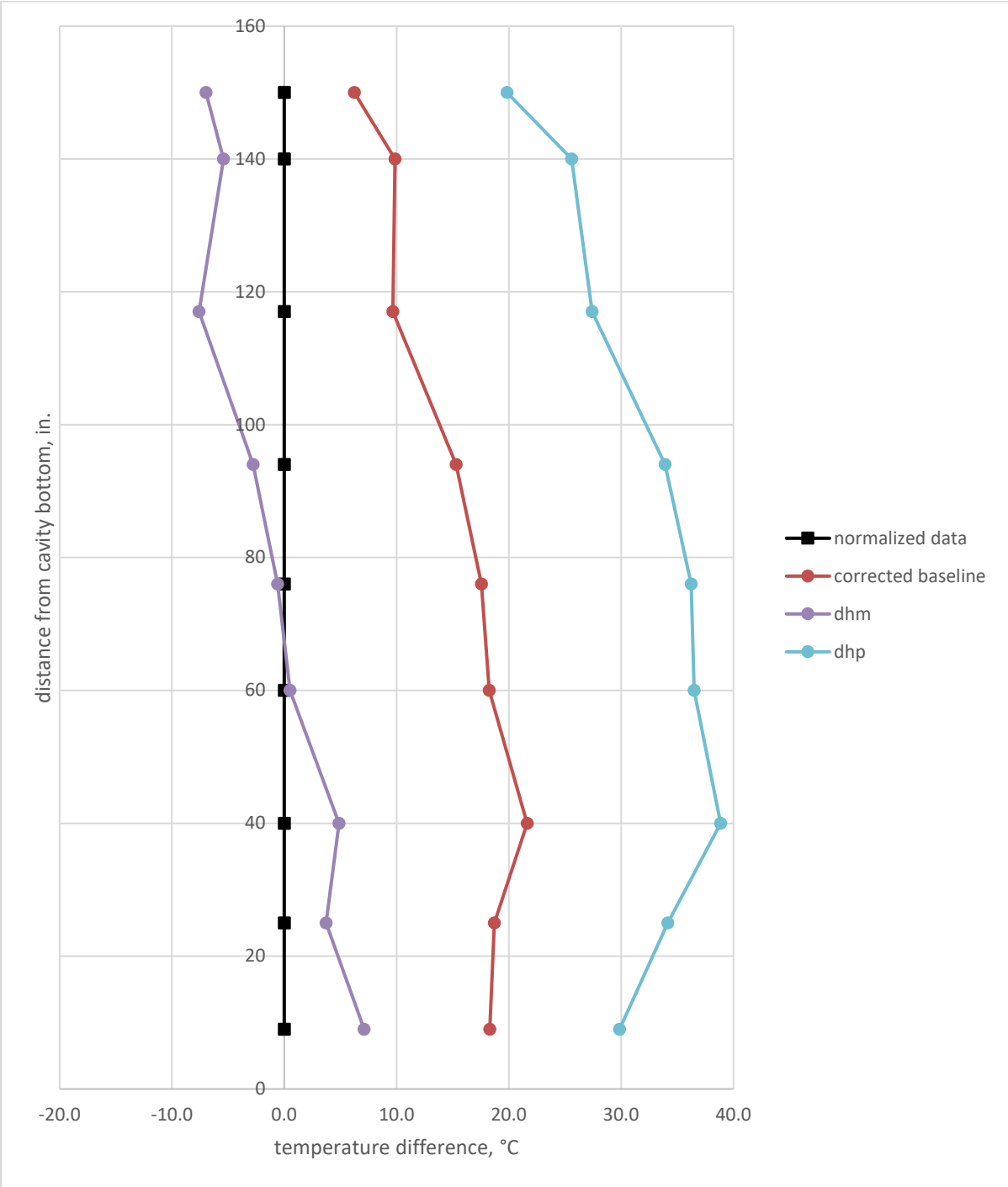

Figure 4-12. Difference between STAR-CCM+ porous model predictions and measurements of Cell 14 fuel temperatures for basket cells; sensitivity to decay heat loading

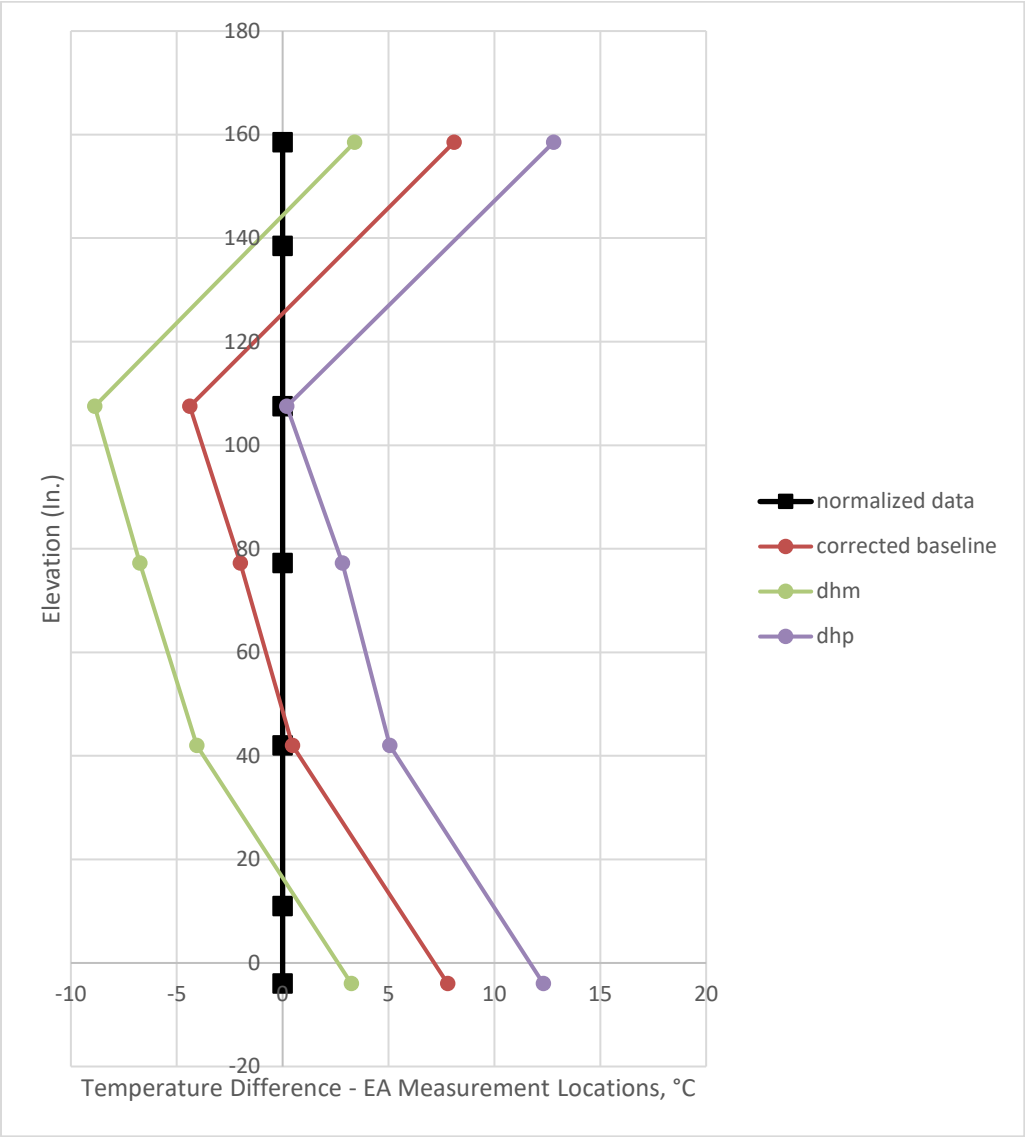

Figure 4-13. Difference between STAR-CCM+ porous model predictions and measurements of "A" cask surface temperatures for basket cells; sensitivity to decay heat loading

4.1.2.6 Neutron Shield

In the international benchmark results and previous HBU demo modeling results, surface temperatures were underpredicted by the STAR-CCM+ models on the neutron shield and more significantly overpredicted above and below the shield on the neutron shield. There are two component parameters that are in question in the thermal model of the neutron shield: 1) resin thermal conductivity and 2) gap resistance between the thin-walled aluminum boxes and the gamma shield on the inside and the outer shell. The conductivity of the aluminum used in the boxes is well known, as is the conductivity of the carbon steel components. Since the baseline gap is already small (0.01 in.), it did not appear to be a first choice for sensitivity runs, but the resin thermal conductivity could be.

The polyester resin is modeled with the thermal conductivity value of 0.173 W/m-K. Literature values can be found for polyester resin at 0.22 W/m-K (Yaman and Taga 2018), and that higher value was run as a first case. Since the resin is loaded with B_4C to form the neutron shield, the effective thermal conductivity should be different than pure resin. Literature values of conductivity for copper particles embedded in a

similar resin were much higher (Yaman and Taga 2018). One literature source was found for thermal conductivity of B_4C (HEDL 1973). It gives a value of approximately 30 W/m-K, which is similar to carbon steel. Therefore, the effective conductivity of the B_4C loaded resin is certainly higher than the pure resin, but by how much is unknown. A case was run at 1 W/m-K as an initial estimate, although the actual value is expected to be larger. Results of varying the neutron shield resin thermal conductivity are shown in Figure 4-14 and Figure 4-15. For the range of values considered, neutron shield resin had a small effect on both fuel and cask surface temperatures.

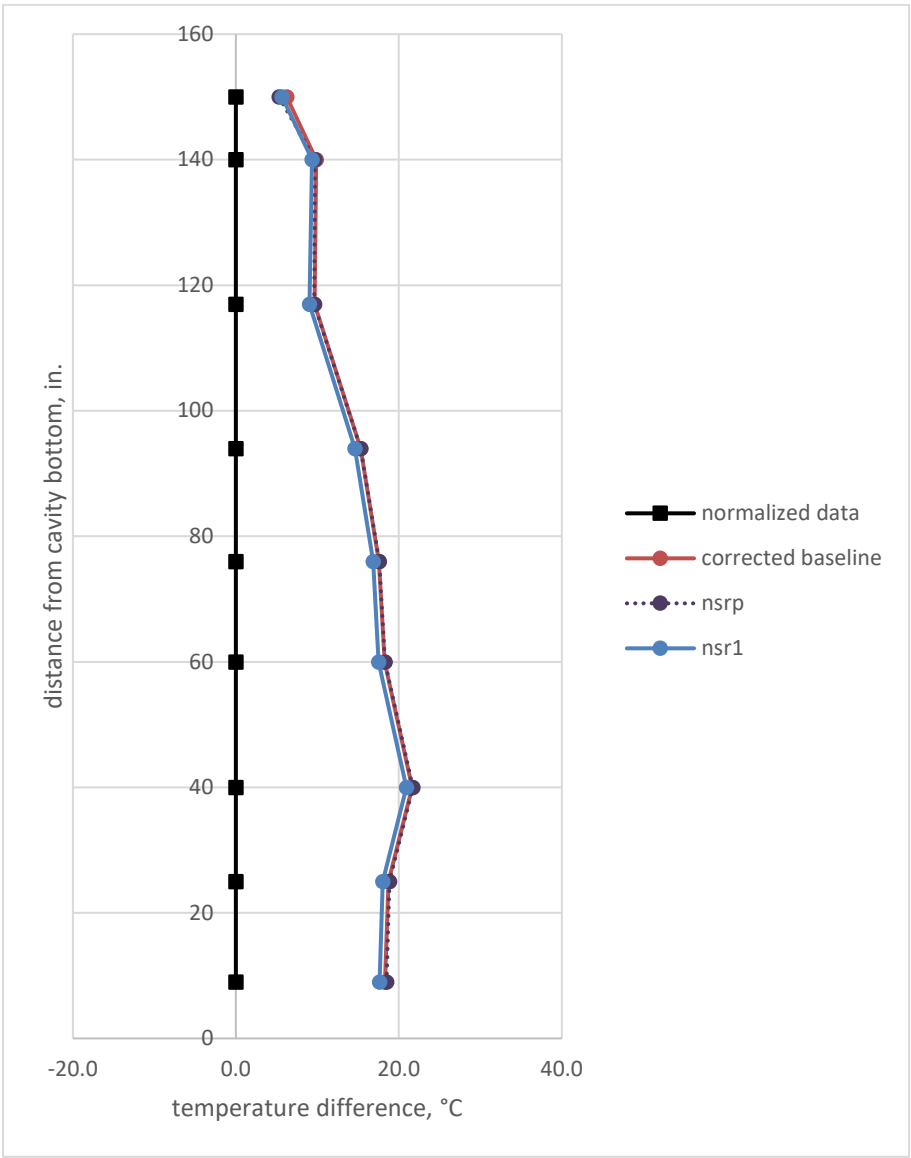

Figure 4-14. Difference between STAR-CCM+ porous model predictions and measurements of Cell 14 fuel temperatures for basket cells; sensitivity to neutron shield resin thermal conductivity

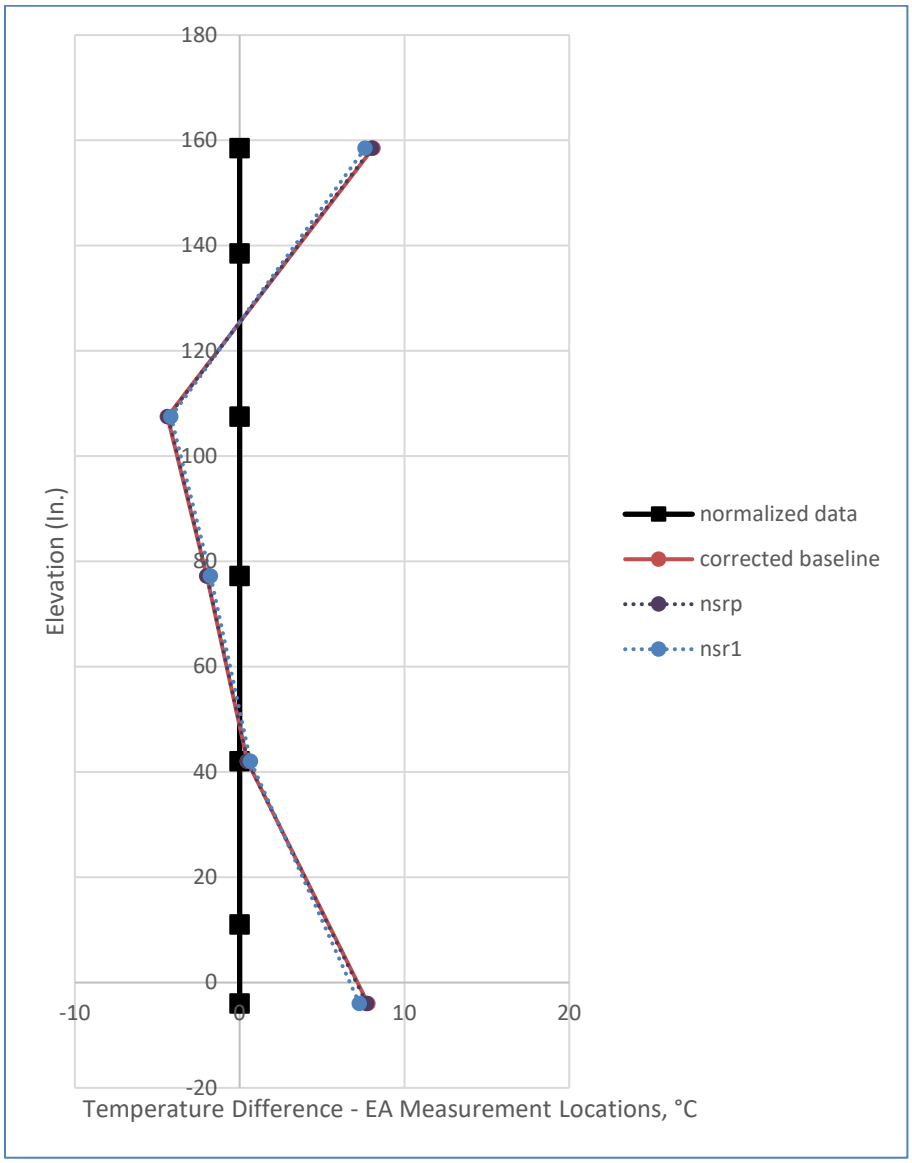

Figure 4-15. Difference between STAR-CCM+ porous model predictions and measurements of "A" cask surface temperatures for basket cells; sensitivity to neutron shield resin thermal conductivity

The gap resistance on either side of the neutron shield box is the other parameter in question. Without knowledge of the manufacturing process, it is reasonable to assume that gaps would be minimized. Also, gaps that were present would tighten or potentially close due to thermal expansion. The thin-walled aluminum boxes are compliant relative to the thicker steel shells, so a thinner gap may be justified. A value of 0.001 in. is small but not unreasonably so. That value was chosen for the sensitivity run (nsg001).

Results for variation in gaps on both sides of the neutron shield aluminum boxes are shown in Figure 4-16 and Figure 4-17. The reduction from 0.01 to 0.001 in. has a larger impact than the change in resin thermal conductivity. Measurement agreement improved at all TC locations in the fuel, as did the magnitude and distribution of temperatures on the cask surface. The smaller gap resulted in greater heat transfer through the neutron shield and correspondingly reduced the amount driven axially to the ends of the gamma shield.

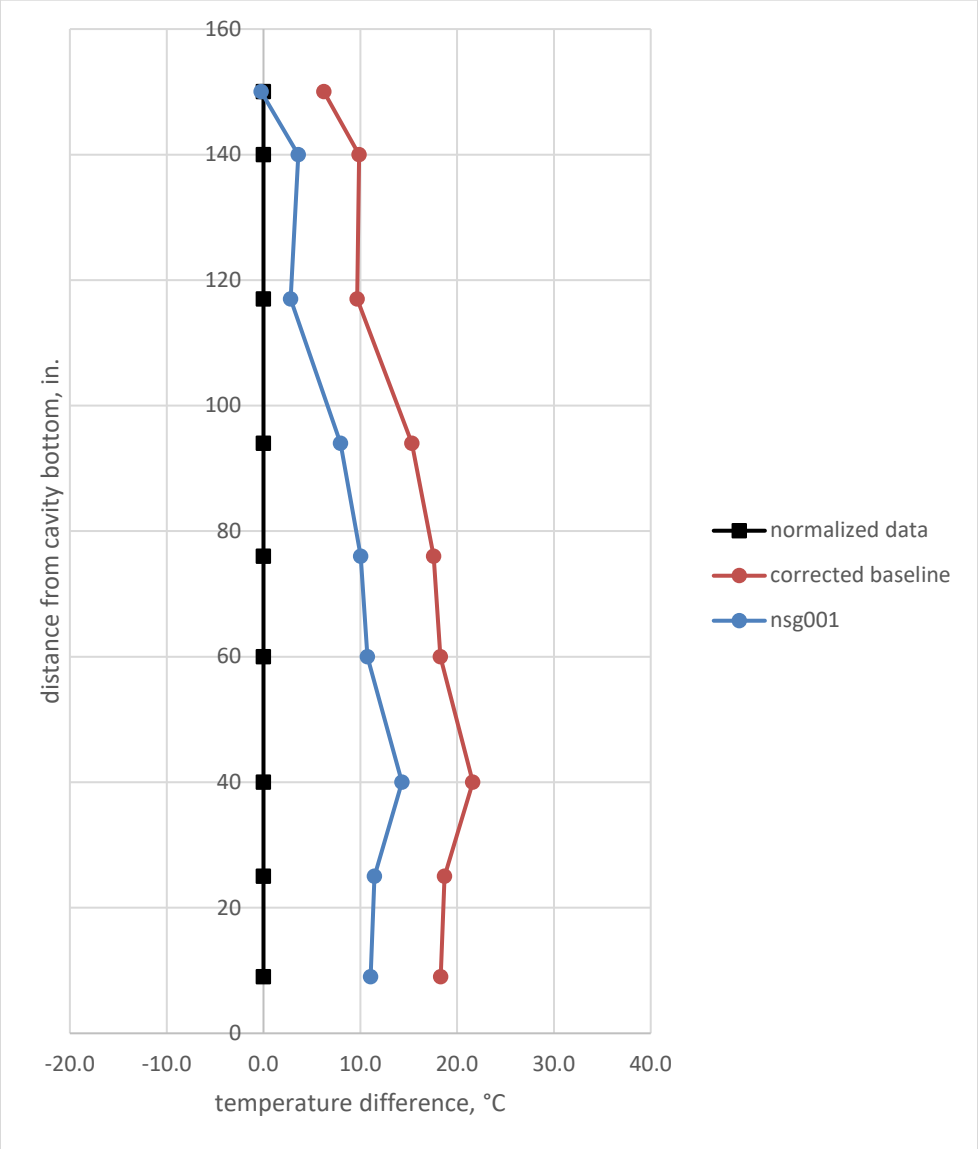

Figure 4-16. Difference between STAR-CCM+ porous model predictions and measurements of Cell 14 fuel temperatures for basket cells; sensitivity to gap thicknesses on both sides of the neutron shield boxes

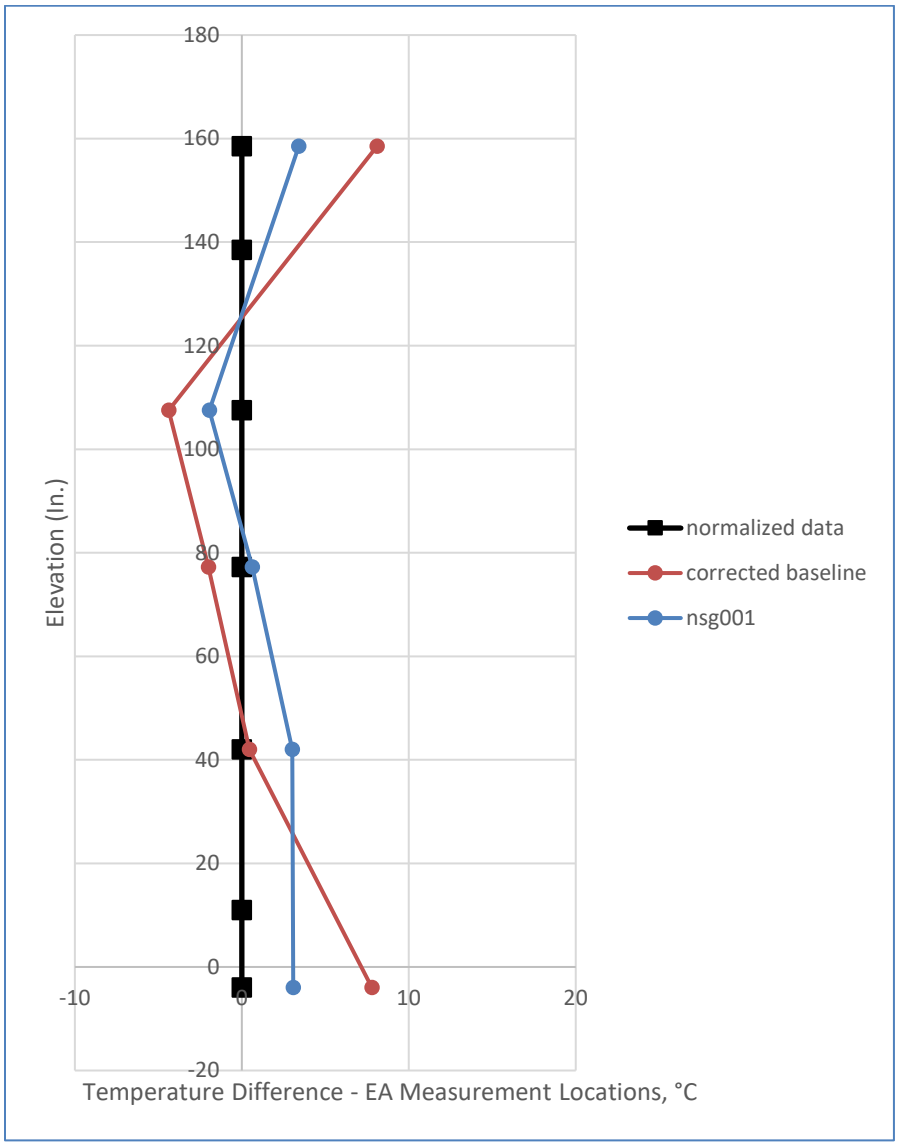

Figure 4-17. Difference between STAR-CCM+ porous model predictions and measurements of "A" cask surface temperatures for basket cells; sensitivity to gap thicknesses on both sides of the neutron shield boxes

This relative difference in sensitivity to these neutron shield parameters may be surprising, but it can be related to the thermal conditions in the fuel basket. The gaps on both sides of the neutron shield basket are important because it is a resistance common to the bulk of the heat transfer from the spent fuel to the environment. In contrast, the path *through* the neutron shield can be either along the highly conductive aluminum box walls, or across the much lower conductivity resin. What happens there is analogous to heat transfer in the loaded basket when the basket wall is highly conductive. The neutron shield resin thermal conductivity is in the same range as the effective thermal conductivity used for the homogenized fuel region in the porous model.

4.2 Representation of Sensitivity Results

A common way to compare all cases is needed. An obvious choice is the change in the difference from the peak measured temperature. In the experiment, the peak temperature was measured in Cell 14 at the TC position 94 inches above the base of the case cavity. A second measure would be helpful to reflect the

change in axial gradient, especially toward the bottom of the cask. For that, the second TC location up from the bottom on the same Cell 14 lance was arbitrarily chosen. That TC is at 25 inches above the base of the cask cavity. Table 4-2 summarizes temperature differences between STAR-CCM+ porous model predictions and measurements at those two locations, abbreviated 14/94 and 14/25.

Table 4-2. Summary of differences in porous model predictions from measurements

	Maximum (14/94)		Lower (14/25)		
Case	Diff from measured	Diff from baseline	Diff from measured	Diff from baseline	Ratio of Diffs 25/94
baseline	15.3	0	18.7	0	-
ambm	9.8	-5.5	12.9	-5.8	1.1
ambp	20.9	5.6	24.9	6.2	1.1
bg001	13.4	-1.9	7.1	-11.6	6.1
bg025	14.3	-1	12.6	-6.1	6.1
bgm	15.3	0	18.1	-0.6	-
bgp	15.5	0.2	19.4	0.7	3.5
bgr	15.2	-0.1	17.8	-0.9	9.0
dhm	-2.8	-18.1	3.7	-15	0.8
dhp	33.9	18.6	34.1	15.4	0.8
nsg001	8	-7.3	11.5	-7.2	1.0
nsr1	14.9	-0.4	18	-0.7	1.8
nsrp	15.3	0	18.9	0.2	-
rgm	7.8	-7.5	12.5	-6.2	0.8
rgp	22.2	6.9	22.4	3.7	0.5

The final column in Table 4-2 reflects the relative change in temperature at the lower measurement location versus that at the hottest elevation. The largest values result from the changes at the base of the cask, either by adding thermal radiation to the gap resistance or by changing the gap thickness.

4.3 Transient Models

Initial results for models of vacuum drying of the HBU demonstration cask were published in Fort et al. (2019b). These included results for a COBRA-SFS model and for two STAR-CCM+ models: one was a detailed model that used an explicit representation of the fuel assemblies and the other used effective properties in a porous media representation of the fuel. These STAR-CCM+ models have been updated for the present study.

Updates to the transient models are described in Section 4.3.1. Sensitivity results are presented in Section 4.3.2 to illustrate the impact of assumptions made for the initial condition corresponding to cask removal from the pool.

4.3.1 Model Updates

The objectives of the model updates were to improve the representation of the experiment and to achieve consistent results between the two models. The models were also updated to use the inputs consistent with the international benchmark activity. The differences in cask geometry were expected to have little impact on temperature predictions for the vacuum drying transient and were left unchanged.

4.3.1.1 Detailed Model

To be consistent with model improvements made in the international benchmark, changes made to the detailed vacuum drying model include:

- Specific carbon steel properties used for the liner and gamma shield
- Thermal radiation added to the boundary condition at the base of the cask.

The large gap resistance between the liner base and gamma shield (1/8 inch) was retained for consistency with the international benchmark.

For parameters specific to the transient calculation, the 100°F pool temperature assumed for the initial condition was left unchanged. The simulation time with water in the cask was shortened to 20 h based on the time log in Waldrop (2019).[b] Finally, the model's application of the decay heat distribution was corrected. The total decay heat is the same as previous

4.3.1.2 Porous Media Model

Updates to the porous model were consistent with those listed above for the detailed model.[c] There were several additional changes specific to the porous media model:

- Changed unheated portions of fuel assemblies from fluid to porous media
- Corrected the fuel region effective thermal conductivity

The first change allowed a more accurate representation of the flow losses in the unheated portions of the fuel assembly. More importantly, it allowed the mass and heat capacity of those sections to be correctly represented in the transient.

In the STAR-CCM+ superficial velocity formulation, transient energy change is scaled by the porosity, σ

$$\frac{\partial}{\partial t}\int_V \left(\sigma(\rho E)_{fluid} + (1-\sigma)\left(\rho C_p\right)_{solid} T\right) dV$$

This is necessary to compute temperature change in a region composed of fluids and solids with different densities and heat capacities. However, this complicates the treatment of thermal conductivity in the homogenized fuel rod and gas region that represents the fuel assembly. Typically, a radial effective thermal conductivity, k_{eff}, is used to represent the combined effects of thermal radiation and conduction from the fuel rods to the walls of the fuel compartment. In this formulation, k_{eff} includes the contribution of conductivity through the gas. In STAR-CCM+ separate values for the fluid and solid fractions of the porous media are used. In a steady state simulation, the solid phase thermal conductivity can be set equal to k_{eff} and the porosity is set to zero to eliminate the repeated contribution of the fluid phase. For a transient simulation this is not possible, but the following correction to the solid thermal conductivity accomplishes the desired result,

$$k_{solid} = k_{eff}/(1-\sigma) - \sigma k_{fluid}$$

[b] See Table 5-1 of Waldrop, 2019.

[c] Final reviews found that porous models used a small gap resistance (0.001-inch) between the liner base and gamma shield. This is expected to have only a very small impact (< 1°C) on maximum temperatures presented in Figure 3-18.

This correction was applied to the radial and axial effective thermal conductivity in the porous media model results in this report.

4.3.2 Model Comparison and Initial Sensitivity Runs

Simulations described in the original study (Fort et al. 2019) were repeated with the updated models. Model results were compared for two cases: one with a helium atmosphere in the cask cavity during vacuum drying, the other with steam. Results for both were compared with measured temperatures in the fuel.

4.3.2.1 Thermal Properties during Vacuum Drying

The base case run in both models used atmospheric helium for blowdowns. As in the original study, forced convection associated with the gas injection was not modeled, neither was repeated gas injections, but natural convection in the fill gas was included. Once vacuum drying began, the only change in the base case was to turn off convection to simulate conditions in the low-pressure gas. The sensitivity case switched the thermal conductivity of the gas phase to steam at the beginning of vacuum drying. Gas density and heat capacity were left unchanged, assuming these changes are negligible relative to the solid components of the fuel and cask. Also, the axial k_{eff} for the fuel region was unchanged in both models. Based on the greater thermal conductivity of helium, this would overpredict axial heat transfer for the sensitivity case, but since this is not the dominant direction of heat loss, this is also assumed to have a small impact on the results.

Figure 4-18 compares the explicit and porous model results for two measurement locations on the lance temperatures in hot basket location (Cell 14, assembly 57A). The fuel temperature is typically the highest at these axial positions. Temperature magnitudes and temporal variation for both models are consistent for the updated models. The magnitude of difference from measurements are also comparable. Note that the base case using helium properties gives a much better representation of the rate of temperature increase during vacuum drying than does the sensitivity case using steam. This is different than conclusions drawn from our initial modeling of this experiment (Fort et al. 2019).

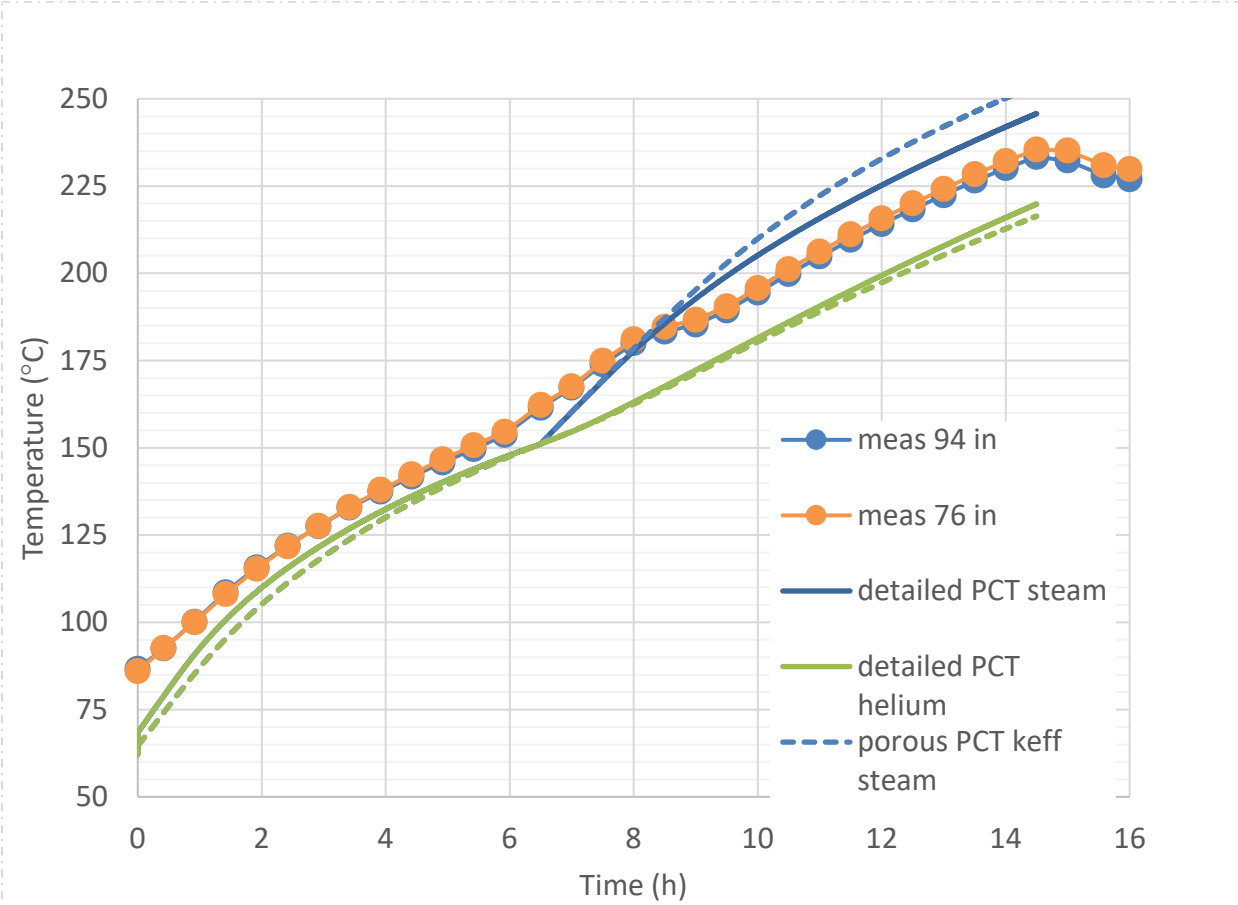

Figure 4-18. Comparison of model results for measurement locations in Cell 14

The model temperatures at the start of this transient are lower than measured. The next sensitivity case looks at potential reasons for this.

4.3.2.2 Rerun of Detailed Case Starting from Lid Placement in Pool

The starting temperature for both models is based on temperature rise in the water inside of the cask cavity. Fuel temperatures after the 20 h transient following removal from the pool are well under measured values (Figure 4-18).

The initial condition for results shown in Figure 4-18 assumed cask and fuel at a pool temperature of 100°F. That temperature was an estimate. This assumption of water in the cask being at the same temperature as the pool is consistent with the lid not being placed until just prior to removal. However, the lid was placed on the cask while still in the pool and the cask was not fully out of the water for another 2.75 h (Waldrop 2019). During that time, the water inside the cask will increase in temperature subject to thermal losses from the cask to the pool water. Is that temperature increase significant relative to the underprediction shown in Figure 4-18? A sensitivity run was performed for that time period to find out.

This simulation was performed with the detailed model using the model for the 20 h that water is in the cask after it is removed from the pool, transferred and placed in the decontamination bay, up to the point where cask draining begins. For this 2.75 h transient within the pool, the run time was shortened and the exterior boundary was set to the pool temperature of 97°F (Waldrop 2019).

During the time in the pool, PCT increased from the 36.1°C (97°F) initial condition to 48.3°C (119°F). For this simulation, any increase in the water conductivity due to convection was ignored, which seems reasonable for small temperature differences. This makes up 12°C of the up to 21°C difference between the model predictions and measurements at the beginning of the plot in Figure 4-18. The original transient for the cask out of the pool (Figure 4-18) does not model water convection and instead uses a multiplier of 3.66, based on use with the COBRA-SFS code for gas in the cask cavity. This is likely an overestimate for the effect of convection within the liquid-filled cask. An additional sensitivity case will be run for a reduction in this multiplier to determine how much of an impact that would make on the remaining difference between measured and predicted fuel temperatures during heating of the cask water.

A sensitivity case was run with a reduced multiplier 2 × k_H_2O (1.24 W/m-K) once the cask is out of the pool. The PCT at the end of that simulation was 86.4°C, which agrees very well with the starting point of the measured temperatures in Figure 4-18.

Water convection can be modeled directly using the porous model. While it does not have an explicit representation of the fuel, the increase in peak temperature should be useful. The 2.75 h transient using the porous model with the same pool water temperature as the boundary condition gives a PCT of 45.2°C or an increase of 9°C. While not as high as the 12°C increase predicted with the detailed model without convection, the porous model can be argued to provide a more realistic estimate of peak temperature. Running this same model for the additional 20 h time in the 61°F (16°C) decontamination bay ambient gives a PCT of 66.4°C.

The question of which simulation result, porous with convection or detailed without convection, is closer to the actual case cannot be conclusively answered until a detailed simulation is run *with* convection. Repeated tests with STAR-CCM+ have not been successful as the segregated solver quickly diverges. Restarting from a developed thermal solution, reduced underrelaxation values, and a further refined mesh have all been attempted without success.

4.3.3 Implications for Uncertainty

Sensitivity runs made in comparison to an experimental result allow model refinement by using physically justifiable changes to improve the agreement with the measured result. With the improved model, predictions of similar cases that have not been tested can be simulated with greater confidence. Sensitivity runs made in the absence of an experimental result show the range of possible solutions. Whether or not the sensitivity cases encompass the actual result depends on identification of the most important parameters and effects.

For the vacuum drying transient, the possibility of a predominately steam or helium atmosphere was investigated. The experiment suggests the latter, but without that result, we would expect the actual case to be between those two simulation results. Different cases were considered for generating initial fuel temperatures in the water filled cask. The experimental result suggests the non-convecting, detailed model result is closer, but without the measurements, the actual case would be expected to fall between these simulation results, unless there are some other significant effects not tested that would shift the predictions outside of this range. In any case, the difference is relatively small between predictions for the initial fuel temperature, prior to draining the cask. The property differences during the actual drying produce a larger variation in results that would encompass the uncertainty in the initial condition.

This page is intentionally left blank.

5. UNCERTAINTY QUANTIFICATION FOR HIGH BURNUP DEMONSTRATION RESEARCH PROJECT CASK

An uncertainty analysis was run with the high burnup demonstration research project cask models to determine the uncertainty in the temperature predictions and provide a range over which the predicted temperatures are expected to vary. The uncertainty analysis was run using the software Dakota (Dakota 2021). Dakota was developed by SNL with a variety of capabilities, including uncertainty quantification and parametric analyses. Dakota is connected to the simulation software, in this case STAR-CCM+ or COBRA-SFS, allowing the user to choose parameters for perturbation.

An LHS statistical method was used to run the uncertainty analysis and determine the 95–95 error bars associated with each component temperature predicted with the thermal models. The error bars represent the range over which the predicted component temperatures may vary. The error bars were calculated from the Dakota results for the overall mean, and the 95% confidence interval (CI) high and low means and standard deviation (σ), which removes the assumption of symmetry. The equations for calculating the lower and upper error bars are:

$$\text{lower} = 2\sigma_{95CI_lower} + (\text{overall}_{mean} - \text{lower_95CI}_{mean}) \quad (3)$$

$$\text{upper} = 2\sigma_{95CI_upper} + (\text{upper_95CI}_{mean} - \text{overall}_{mean}) \quad (4)$$

Five different perturbation parameters were used for the LHS analysis and are listed in Table 5-1. The parameters were assumed to have a uniform distribution based on the min and max values listed in Table 5-1.

Table 5-1. Perturbation parameters

Parameter	Min	Max
Ambient Temperature	22.8°C	25°C
Decay Heat	−2%	+2%
Rail-Basket Gap	0.01 in	0.19 in
Base Gamma Shield to Liner Gap	0.01 in	0.125 in
Neutron Shield Can to Shell Gaps	0.001 in	0.02 in

The five parameters in Table 5-1 were reasoned to be the most significant in determining system temperature uncertainty based in parameter sensitivity testing in Section 4.1. The minimum and maximum values in Table 5-1 were based on a best estimate of uncertainty in each parameter.

The measured temperatures during testing in the decontamination bay are shown in Figure 5-1. Measurements were made above and below the work platform, and that platform is near the top of the cask. In modeling to date (Fort et al. 2019a, Fort et al. 2020), the average measured temperature below the work platform has been used in boundary conditions because most of the heat transfer is through the sides of the cask. The difference between measured temperatures above and below the work platform is significant as is the magnitude of diurnal variation due to ventilation from outdoors. The parameter range for ambient temperature in Table 5-1 may appear small, given these differences; however, the 23.9°C (75°F) average value of measured temperature below the work platform is consistent over the last three days of the thermal soak. The minimum and maximum values of ambient temperature in Table 5-1 are based on measurement uncertainty at that location. The difference in ambient temperature above the work platform or in the gap between the cask bottom and floor are not part of the uncertainty in ambient

temperature, because they represent separated environmental regions, and the side cask temperature can be assumed to have an overwhelming influence on component temperatures compared to the temperature above the cask.

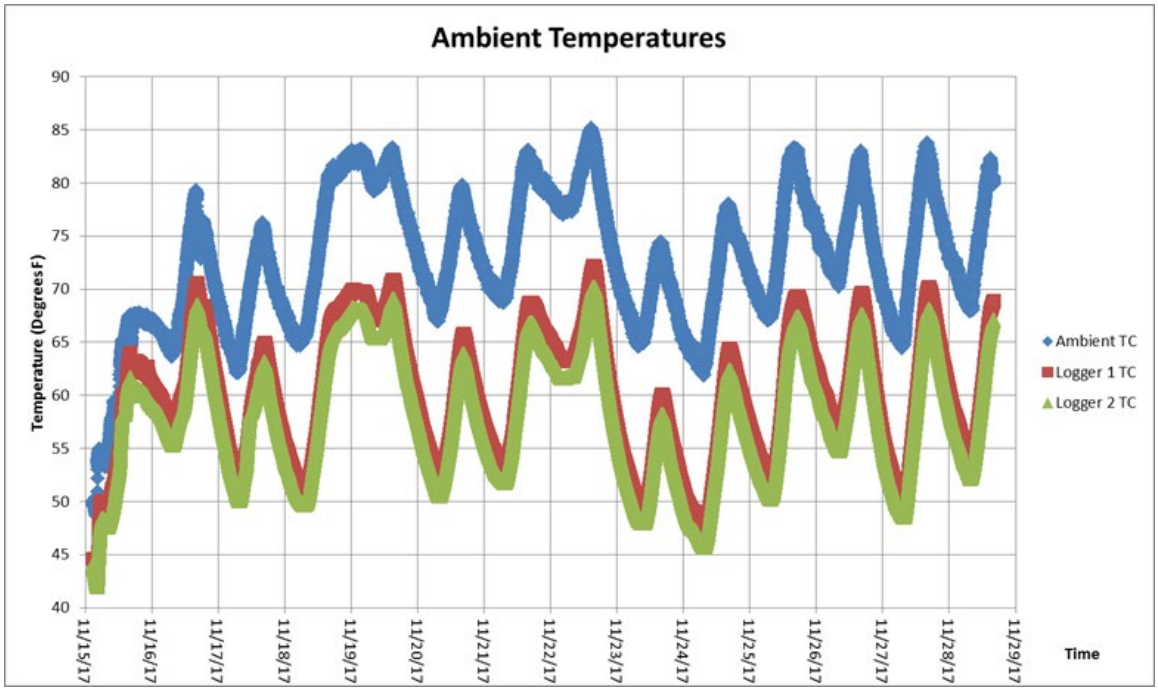

Figure 5-1. Air temperature in the decontamination pit (ambient TC) and above the work platform (logger 1 and 2 TC)

The minimum/maximum range for decay heat in Table 5-1 is based on expected uncertainty in ORIGEN calculations. The range between minimum and maximum values for the three gaps in Table 5-1 are each relatively large but reflect the lack of knowledge in their actual values. In general, the minimum values represent what may result from a nearly closed gap due to thermal expansion. The maximums represent expected gaps at ambient conditions.

5.1 STAR-CCM+

Dakota was connected to STAR-CCM+ and an uncertainty quantification of the high burnup demonstration research project cask model was conducted. A sensitivity study was performed to look at the number of cases needed to ensure that the error bars were not changing as the number of cases increased. The resulting PCT mean and error bars were used for the sensitivity analysis. An LHS analysis was performed for 10, 20, 50, and 70 cases. The resulting PCT mean and range for each analysis is plotted in Figure 5-2. Results show that while the mean is similar between the different analyses, the error bar range is reduced as the number of cases is increased. For the 50 and 70 case analyses, the resulting error bar range was within 1°C of each other, indicating the error bars were converged at 50 cases for the LHS analysis. The results also indicate that executing the analysis with a small number of total cases results in larger, or more conservative, 95–95 uncertainty intervals.

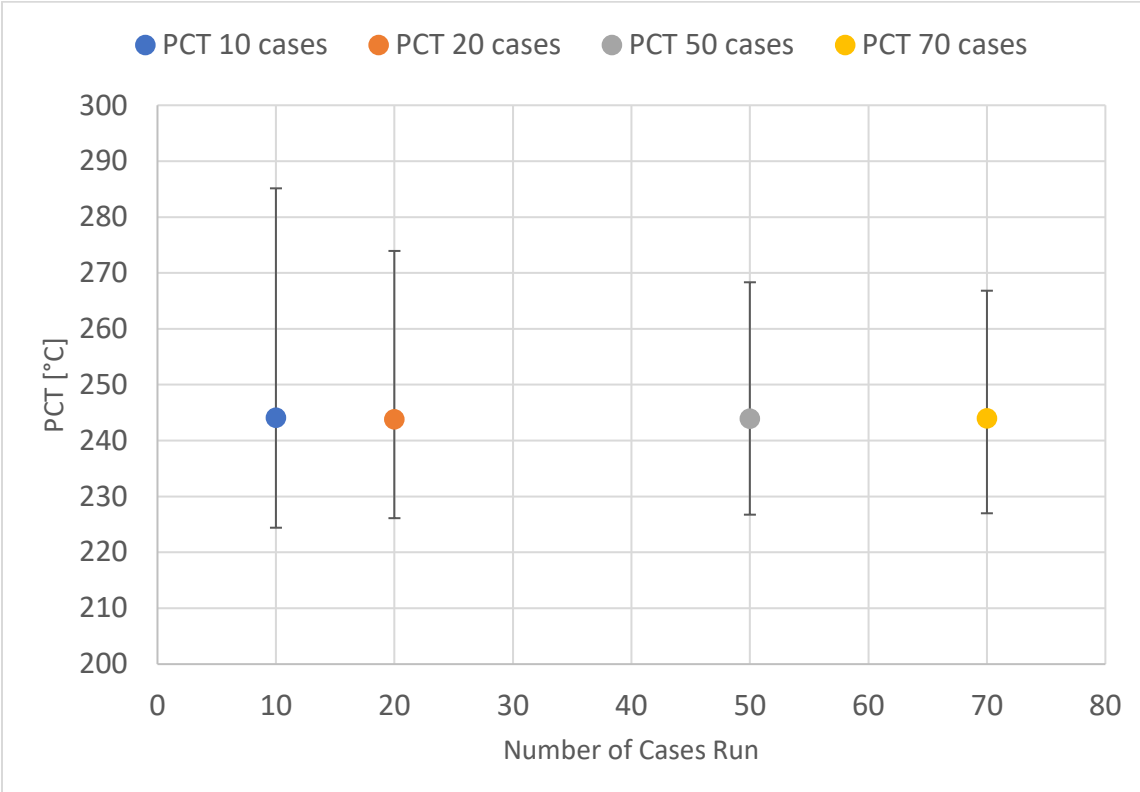

Figure 5-2. Number of cases sensitivity study results for PCT

The 70 cases analysis was used for the UQ of the High Burnup Demonstration STAR-CCM+ model. The LHS analysis provided temperature predictions for the fuel TCs (rods 3K7, 3U4, 3U6, 3U9, 5T9, 30A, and 57A), surface temperature measurements (A1-A5), and PCT. Temperature measurements from the High Burnup Demonstration (Fort 2019b, Fort 2020) are compared against the predicted canister and fuel temperatures predicted by the STAR-CCM+ model. The resulting mean component temperatures and error bar ranges predicted by the STAR-CCM+ model are given in Table 5-2. The PCT and cask surface temperature results are plotted in Figure 5-3 and Figure 5-4, respectively. There was not a PCT measurement to compare against, but the cask surface temperatures are plotted against the measurements in Figure 5-4. The STAR-CCM+ model predicts a much flatter canister profile than the measurements, with only the measurement temperatures of A3 and A4 falling within the temperature ranges predicted by the model.

Plots of the fuel TC temperature predictions and measurements are shown in Figure 5-5 through Figure 5-11. The error bars shown on the plots for each component temperature represent the potential range over which temperatures may vary due to uncertainties in the model inputs. The mean predicted PCT temperature is 244°C with a –17°C and +23°C range. The average mean temperature predicted at the canister TC locations is ~ 83°C with the range varying from −3°C to −5°C on the lower range and +4°C to +7°C on the upper range. For the fuel TCs, the mean temperature varied from 124°C to 243°C depending on TC location, and the temperature variation ranged from −11°C to −17°C on the lower end and +15°C to +23°C on the upper end. Overall, the measured temperatures are within the ranges predicted by the STAR-CCM+ model. The exception is the 3U6 lance which the model overpredicted temperatures for the lower elevation TCs.

Table 5-2. Results for STAR-CCM+ High Burnup Demonstration Model LHS Analysis

Component	STAR-CCM+ Model			Measurements (°C)
	Mean (°C)	Lower 95–95 Bar (°C)	Upper 95–95 Bar (°C)	
3K7 - TC9	142.8	12.8	17.3	150.6
3K7 - TC8	176.8	14.2	19.2	170.2
3K7 - TC7	200.3	16.0	21.6	190.7
3K7 - TC6	205.1	17.0	23.0	194.1
3K7 - TC5	209.4	16.9	22.9	194.2
3K7 - TC4	207.4	16.6	22.4	191.4
3K7 - TC3	198.1	15.4	20.8	181.3
3K7 - TC2	180.1	14.1	19.1	166.9
3K7 - TC1	141.5	12.2	16.5	132.8
3U4 - TC9	153.1	11.9	16.1	155.4
3U4 - TC8	184.7	13.3	18.0	177.7
3U4 - TC7	208.5	15.5	20.9	201.8
3U4 - TC6	212.4	16.5	22.2	207.2
3U4 - TC5	217.5	16.5	22.3	205.7
3U4 - TC4	213.3	16.1	21.8	201.3
3U4 - TC3	202.7	15.1	20.4	189.1
3U4 - TC2	187.5	13.9	18.7	171.7
3U4 - TC1	145.6	12.5	16.9	135.3
3U6 - TC9	124.0	10.9	14.7	130.8
3U6 - TC8	162.6	12.7	17.1	151.8
3U6 - TC7	187.8	14.9	20.1	173.4
3U6 - TC6	194.1	16.0	21.6	178.1
3U6 - TC5	194.5	16.2	21.9	177.6
3U6 - TC4	194.8	15.9	21.5	174.3
3U6 - TC3	187.9	15.0	20.2	164.4
3U6 - TC2	175.6	13.8	18.7	151.1
3U6 - TC1	141.3	12.0	16.2	121.6
3U9 - TC9	181.3	13.4	18.1	174.4
3U9 - TC8	209.1	14.4	19.5	195.9
3U9 - TC7	228.0	16.3	22.1	218.5
3U9 - TC6	235.2	17.2	23.2	223.3
3U9 - TC5	241.1	17.1	23.1	221.1
3U9 - TC4	234.9	16.5	22.3	215.2
3U9 - TC3	217.6	15.5	20.9	200.0
3U9 - TC2	197.5	14.5	19.6	180.8
3U9 - TC1	154.6	14.1	19.1	141.5

Component	STAR-CCM+ Model			Measurements (°C)
	Mean (°C)	Lower 95–95 Bar (°C)	Upper 95–95 Bar (°C)	
5T9 - TC9	144.9	13.1	17.6	150.7
5T9 - TC8	173.9	14.5	19.6	171.5
5T9 - TC7	192.0	16.3	22.1	194.2
5T9 - TC6	205.2	17.0	22.9	199.6
5T9 - TC5	205.7	17.3	23.4	198.0
5T9 - TC4	203.2	16.9	22.9	193.9
5T9 - TC3	193.3	15.6	21.1	181.8
5T9 - TC2	180.5	14.2	19.2	164.9
5T9 - TC1	141.0	12.2	16.4	131.9
30A - TC9	158.1	11.8	15.9	160.8
30A - TC8	190.8	13.3	18.0	183.9
30A - TC7	213.4	15.4	20.7	206.2
30A - TC6	221.7	16.2	21.9	209.3
30A - TC5	223.0	16.4	22.1	207.9
30A - TC4	220.5	16.0	21.5	203.7
30A - TC3	210.2	14.9	20.1	191.3
30A - TC2	191.1	13.8	18.7	174.3
30A - TC1	146.0	12.6	17.0	136.6
57A - TC9	182.8	13.0	17.6	178.3
57A - TC8	210.2	14.4	19.4	201.7
57A - TC7	233.6	16.0	21.6	225.4
57A - TC6	242.8	16.9	22.8	229.2
57A - TC5	242.8	16.9	22.8	227.2
57A - TC4	236.6	16.5	22.2	220.7
57A - TC3	224.0	15.3	20.7	205.6
57A - TC2	200.5	14.5	19.5	186.2
57A - TC1	155.1	14.1	19.1	143.8
PCT	243.9	16.9	22.9	-
A1	81.7	5.1	6.9	75.6
A2	83.0	3.0	4.0	87.8
A3	85.7	3.1	4.2	88.1
A4	82.9	2.9	3.9	82.8
A5	83.4	5.1	6.9	74.2

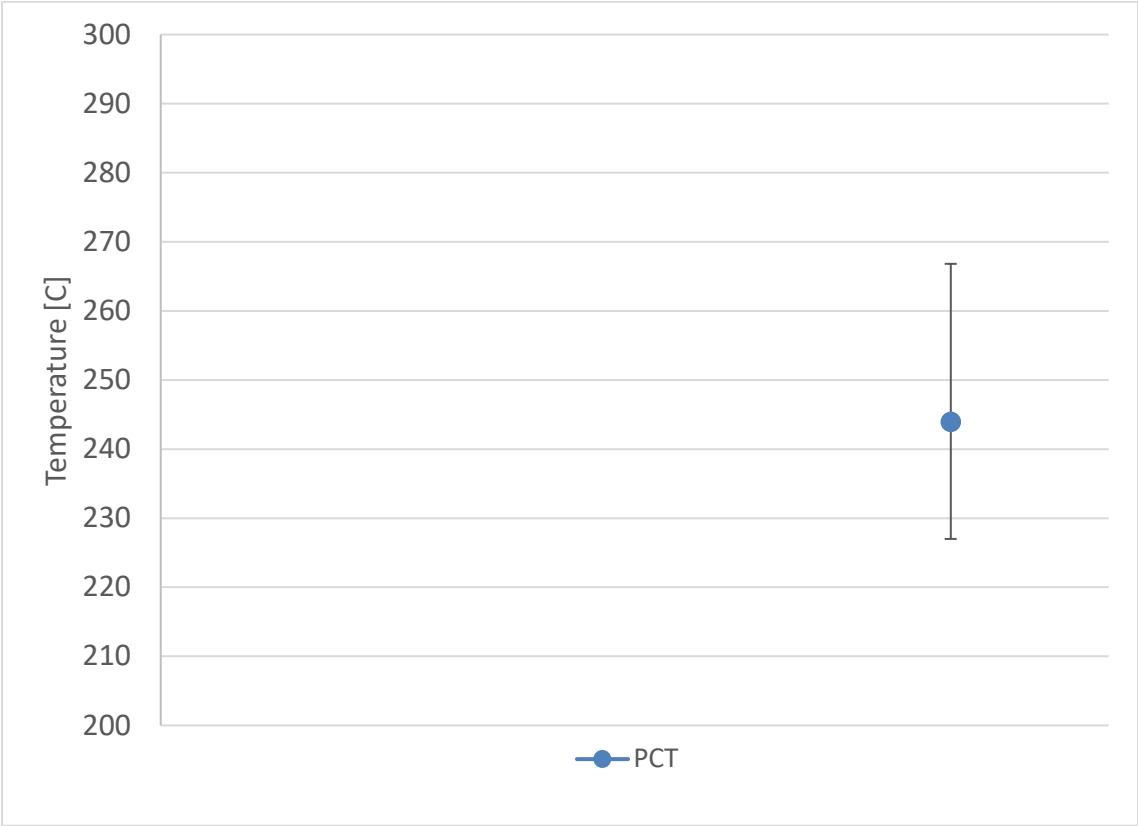

Figure 5-3. STAR-CCM+ High Burnup Demonstration model results for PCT

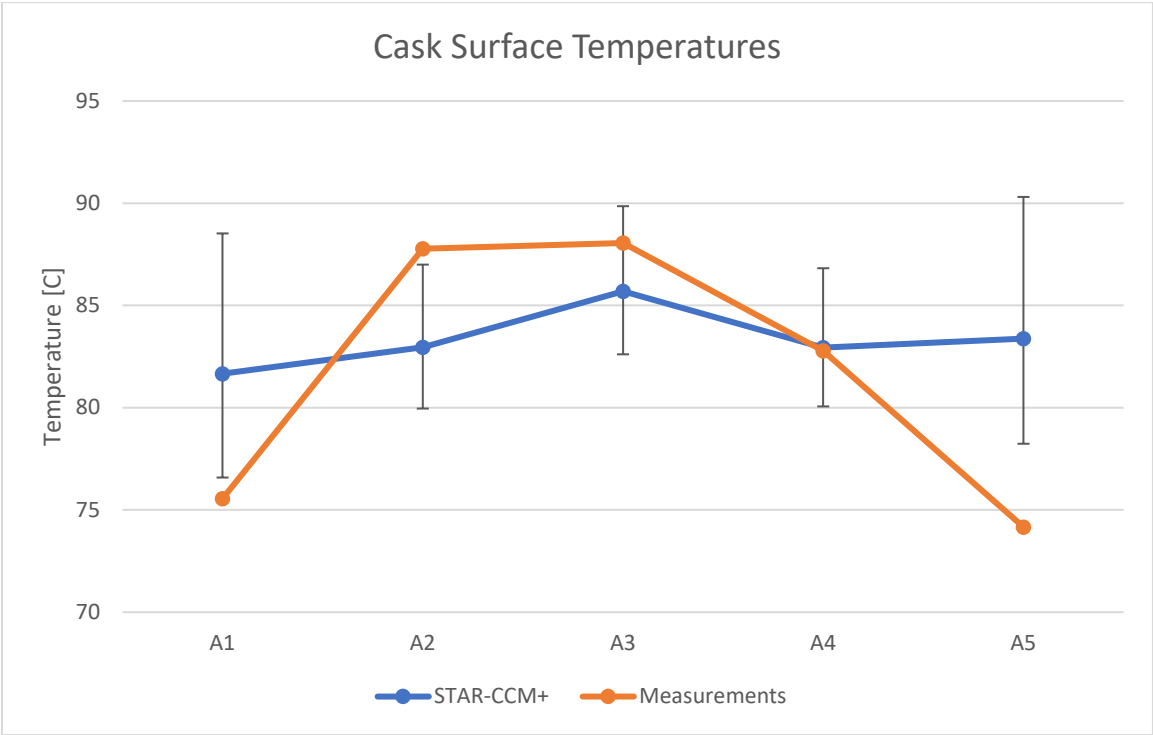

Figure 5-4. STAR-CCM+ High Burnup Demonstration model results for cask surface temperatures

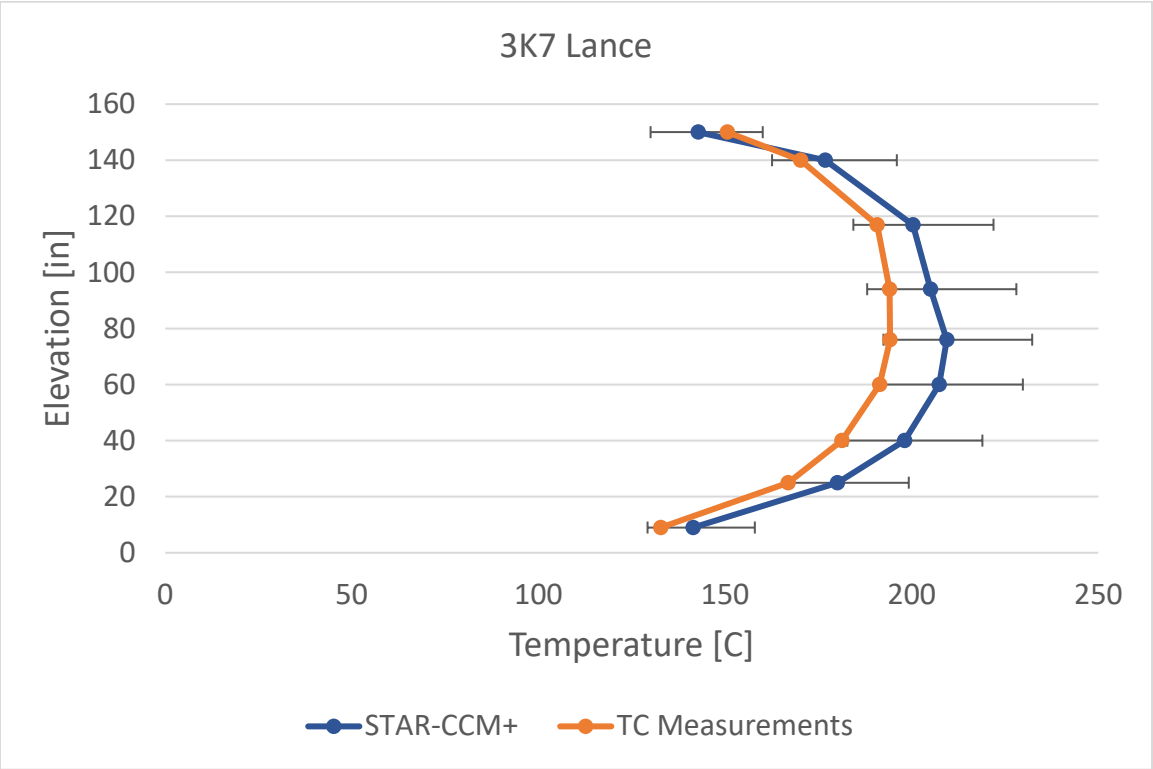

Figure 5-5. STAR-CCM+ High Burnup Demonstration model results for 3K7 fuel TCs

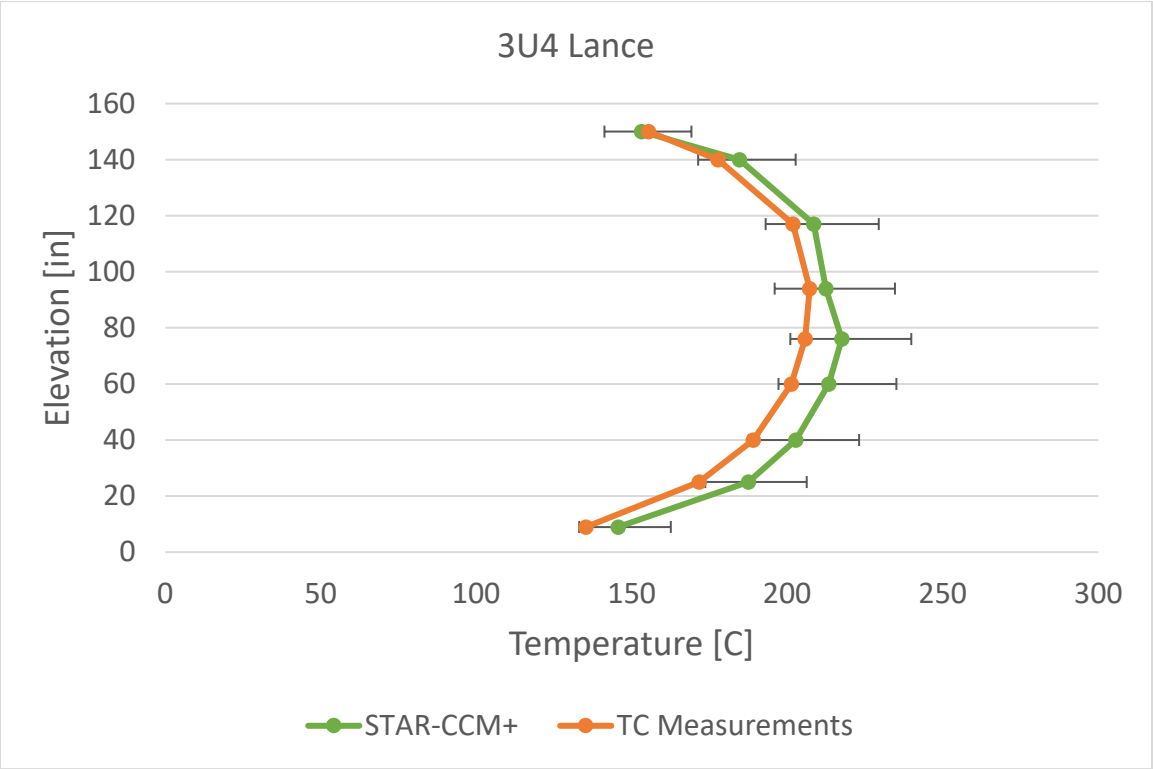

Figure 5-6. STAR-CCM+ High Burnup Demonstration model results for 3U4 fuel TCs

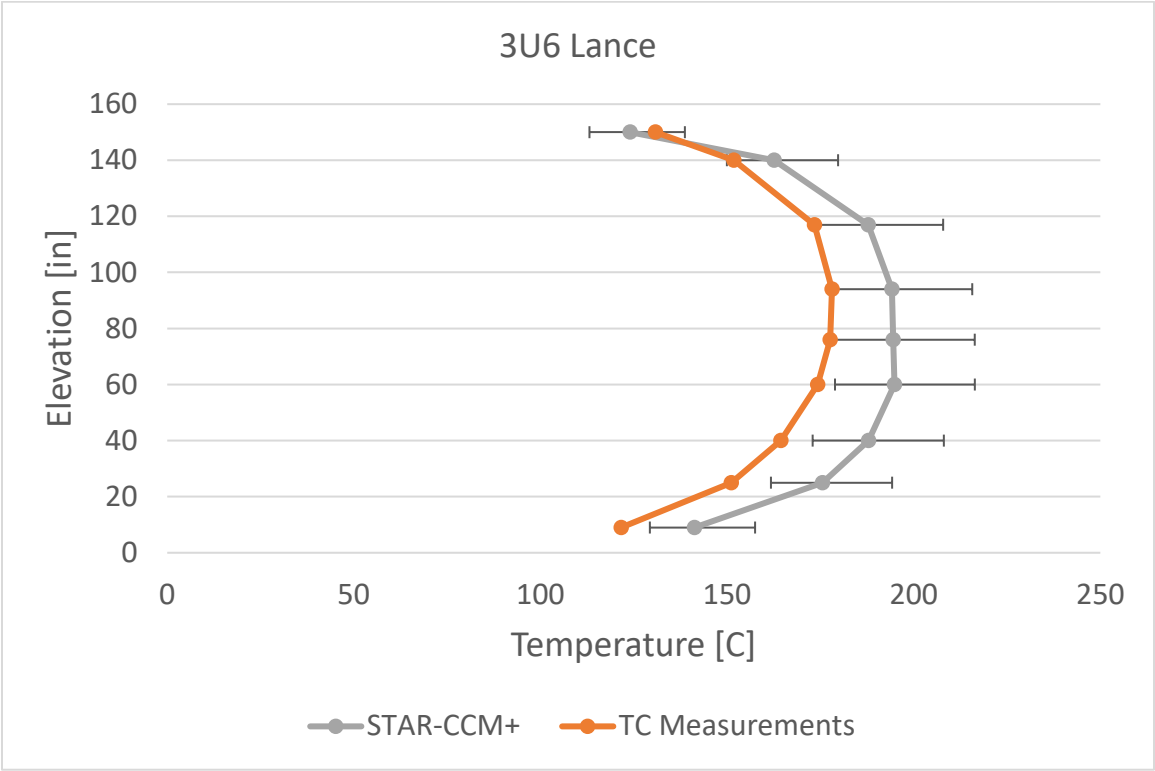

Figure 5-7. STAR-CCM+ High Burnup Demonstration model results for 3U6 fuel TCs

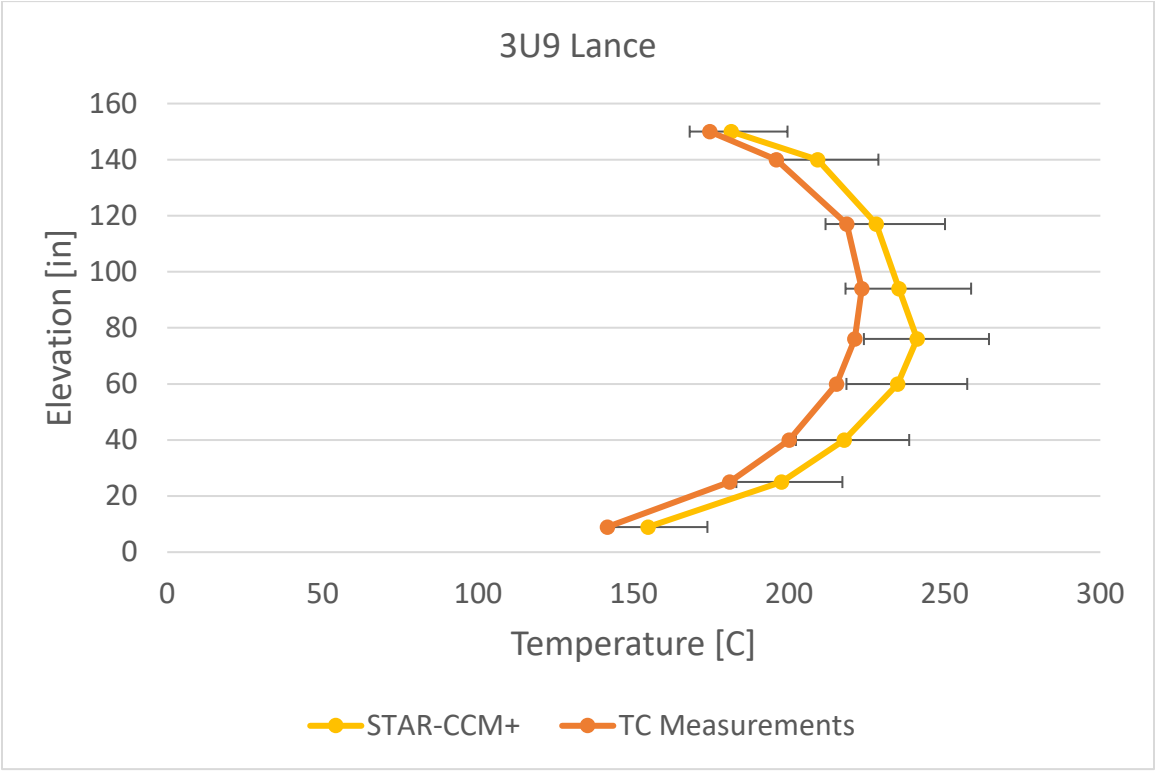

Figure 5-8. STAR-CCM+ High Burnup Demonstration model results for 3U9 fuel TCs

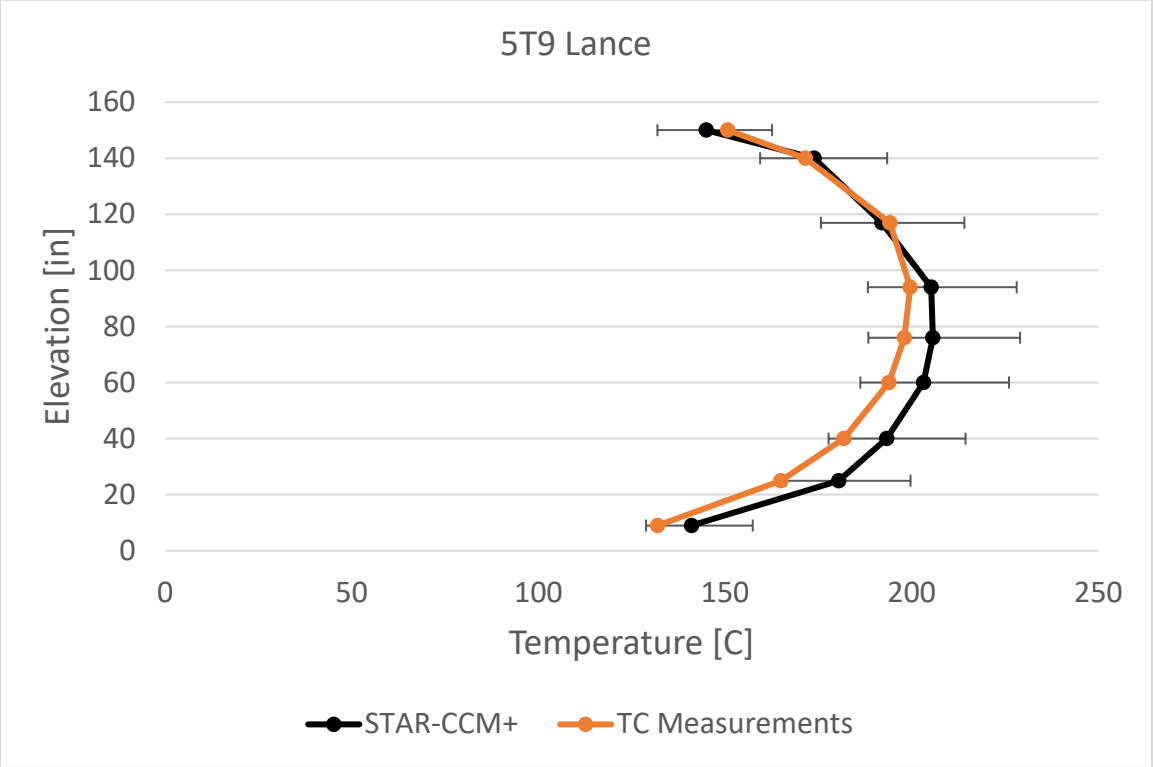

Figure 5-9. STAR-CCM+ High Burnup Demonstration model results for 5T9 fuel TCs

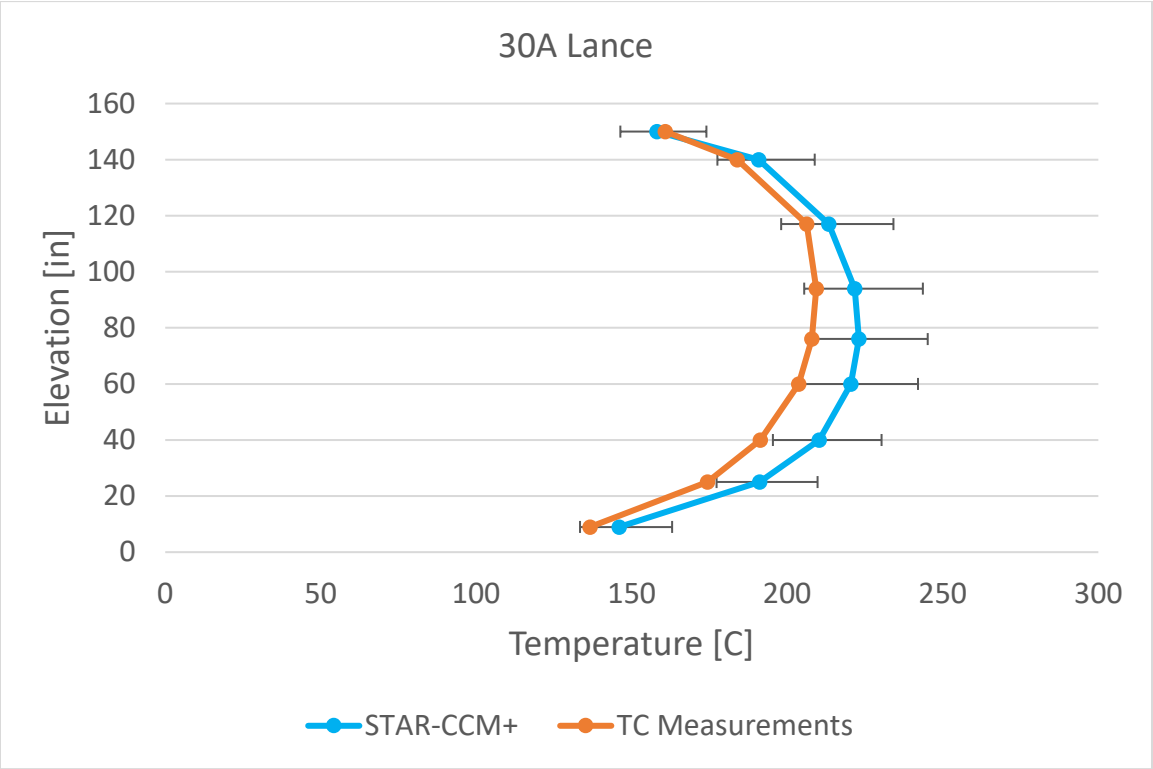

Figure 5-10. STAR-CCM+ High Burnup Demonstration model results for 30A fuel TCs

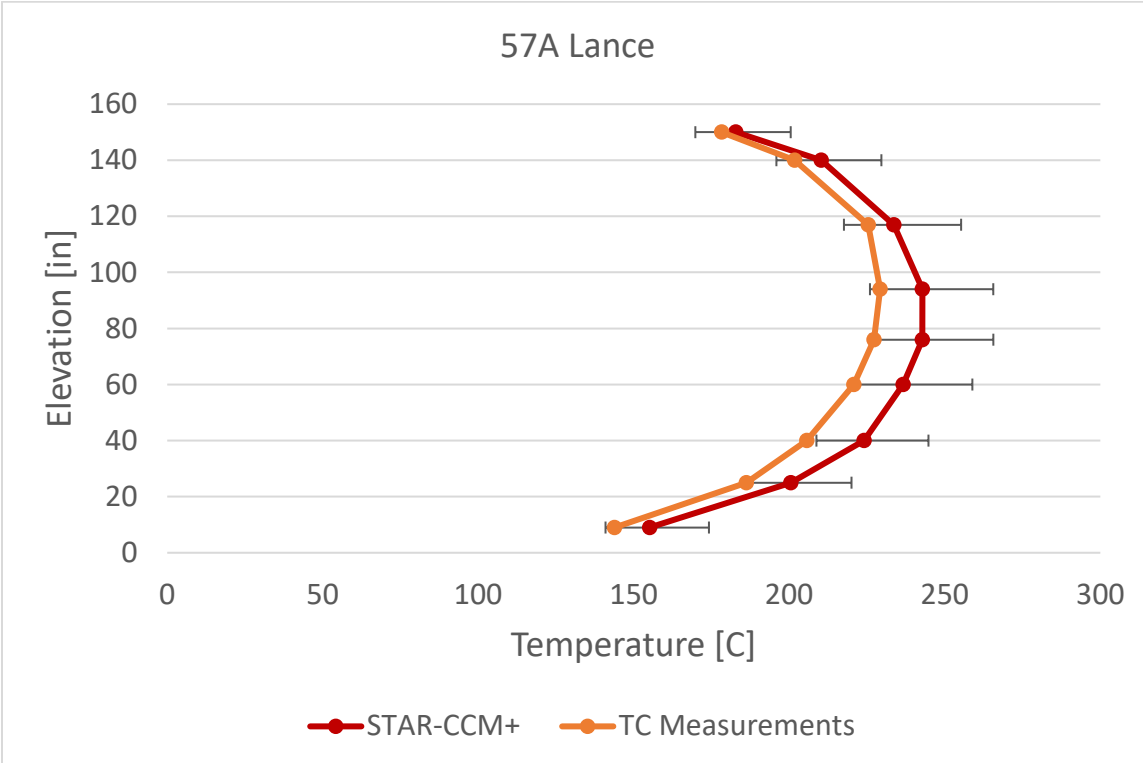

Figure 5-11. STAR-CCM+ High Burnup Demonstration model results for 57A fuel TCs

Table 5-3. STAR-CCM+ LHS UQ results

Response Function	Mean (°C)]	Lower 95–95 Error Bar (°C)	Upper 95-95 (°C)	TC Measurements (°C)
3K7_TC1	157.5	19.7	44.2	150.6
3K7_TC2	184.1	19.2	43.5	170.2
3K7_TC3	205.2	20.1	44.7	190.7
3K7_TC4	210.7	20.2	44.8	194.1
3K7_TC5	210.5	19.6	44.0	194.2
3K7_TC6	206.9	18.4	42.4	191.4
3K7_TC7	196.6	16.2	39.4	181.3
3K7_TC8	182.1	13.8	36.2	166.9
3K7_TC9	149.1	11.1	32.6	132.8
3U4_TC1	168.3	19.1	25.5	155.4
3U4_TC2	194.8	18.8	25.2	177.7
3U4_TC3	217.3	19.6	26.2	201.8

Response Function	Mean (°C)]	Lower 95–95 Error Bar (°C)	Upper 95-95 (°C)	TC Measurements (°C)
3U4_TC4	223.3	19.6	26.3	207.2
3U4_TC5	222.8	19.0	25.4	205.7
3U4_TC6	218.6	17.8	23.9	201.3
3U4_TC7	206.7	15.6	20.9	189.1
3U4_TC8	189.8	13.5	18.0	171.7
3U4_TC9	152.1	11.3	15.2	135.3
3U6_TC1	154.0	18.9	25.3	130.8
3U6_TC2	180.3	18.4	24.7	151.8
3U6_TC3	200.9	19.3	25.8	173.4
3U6_TC4	206.5	19.4	25.9	178.1
3U6_TC5	206.3	18.8	25.1	177.6
3U6_TC6	202.9	17.7	23.7	174.3
3U6_TC7	193.1	15.6	20.9	164.4
3U6_TC8	179.5	13.4	17.9	151.1
3U6_TC9	148.8	10.8	14.5	121.6
3U9_TC1	184.9	19.5	26.1	174.4
3U9_TC2	210.2	19.3	25.8	195.9
3U9_TC3	233.4	19.9	26.6	218.5
3U9_TC4	240.0	19.8	26.5	223.3
3U9_TC5	239.0	19.1	25.5	221.1
3U9_TC6	233.6	17.8	23.9	215.2
3U9_TC7	218.7	15.6	20.8	200.0
3U9_TC8	197.8	13.5	18.1	180.8
3U9_TC9	153.6	11.8	15.8	141.5
5T9_TC1	158.0	19.6	26.3	150.7
5T9_TC2	184.0	19.2	25.7	171.5
5T9_TC3	204.8	20.0	26.8	194.2
5T9_TC4	210.5	20.1	26.9	199.6
5T9_TC5	210.2	19.5	26.1	198.0
5T9_TC6	206.6	18.3	24.5	193.9
5T9_TC7	196.1	16.1	21.5	181.8
5T9_TC8	181.4	13.7	18.4	164.9
5T9_TC9	148.7	11.1	14.8	131.9
30A_TC1	171.7	19.2	25.7	160.8
30A_TC2	199.5	18.9	25.3	183.9

Response Function	Mean (°C)]	Lower 95–95 Error Bar (°C)	Upper 95-95 (°C)	TC Measurements (°C)
30A_TC3	222.7	19.6	26.2	206.2
30A_TC4	228.8	19.6	26.3	209.3
30A_TC5	228.3	19.0	25.4	207.9
30A_TC6	223.9	17.8	23.8	203.7
30A_TC7	211.6	15.6	20.8	191.3
30A_TC8	194.0	13.4	17.9	174.3
30A_TC9	153.7	11.4	15.2	136.6
57A_TC1	184.7	19.4	25.9	178.3
57A_TC2	211.7	19.1	25.6	201.7
57A_TC3	235.5	19.7	26.4	225.4
57A_TC4	242.1	19.7	26.4	229.2
57A_TC5	241.1	19.0	25.4	227.2
57A_TC6	235.9	17.8	23.8	220.7
57A_TC7	221.2	15.5	20.7	205.6
57A_TC8	200.3	13.5	18.1	186.2
57A_TC9	154.5	11.8	15.8	143.8

5.2 COBRA-SFS

The COBRA-SFS model used to generate results in this report was the same model used in previous High Burnup Demo Cask work (Fort et al. 2019a) with modifications to reflect the international round robin data specifications (Fort et al. 2020). To investigate the behavior of the model and find the relationship between calculated input uncertainty and number of simulations, the model was run in six different Dakota analyses from 25–150 samples in steps of 25 samples. This workflow allows analysis of the "ideal" number of simulations, although it is overall more inefficient than what would be used in a more typical application. Figure 5-20 shows an asymptotic behavior of the 95–95 uncertainty interval starting at 75 cases. This case count is copasetic with the STAR-CCM+ results and was used to generate all of the results in Section 5.2. Each TC measurement point is compared against the measured data in Figure 5-12 through Figure 5-18. The plotted error bars reflect a 95–95 confidence interval calculated in the same manner as Section 5.1. In nearly all cases, the plotted error bars encompass the measured data representing a good agreement between model and data. It is important to note that the uncertainty encompasses only input uncertainty in this case and also that the selected input values and ranges are for demonstration purposes and do not encompass a rigorous examination. The goal of this report is methodology development and demonstration.

Table 5-4. COBRA-SFS LHS UQ Results

Response Function	Mean (C)	Lower 95-95 Bar (C)	Upper 95-95 Bar (C)	TC Measurements (C)	Elevation (in.)
3K7_TC1	157.5	19.7	44.2	150.6	150.0
3K7_TC2	184.1	19.2	43.5	170.2	140.0
3K7_TC3	205.2	20.1	44.7	190.7	117.0
3K7_TC4	210.7	20.2	44.8	194.1	94.0
3K7_TC5	210.5	19.6	44.0	194.2	76.0
3K7_TC6	206.9	18.4	42.4	191.4	60.0
3K7_TC7	196.6	16.2	39.4	181.3	40.0
3K7_TC8	182.1	13.8	36.2	166.9	25.0
3K7_TC9	149.1	11.1	32.6	132.8	9.0
3U4_TC1	168.3	19.1	25.5	155.4	150.0
3U4_TC2	194.8	18.8	25.2	177.7	140.0
3U4_TC3	217.3	19.6	26.2	201.8	117.0
3U4_TC4	223.3	19.6	26.3	207.2	94.0
3U4_TC5	222.8	19.0	25.4	205.7	76.0
3U4_TC6	218.6	17.8	23.9	201.3	60.0
3U4_TC7	206.7	15.6	20.9	189.1	40.0
3U4_TC8	189.8	13.5	18.0	171.7	25.0
3U4_TC9	152.1	11.3	15.2	135.3	9.0
3U6_TC1	154.0	18.9	25.3	130.8	150.0
3U6_TC2	180.3	18.4	24.7	151.8	140.0
3U6_TC3	200.9	19.3	25.8	173.4	117.0
3U6_TC4	206.5	19.4	25.9	178.1	94.0
3U6_TC5	206.3	18.8	25.1	177.6	76.0
3U6_TC6	202.9	17.7	23.7	174.3	60.0
3U6_TC7	193.1	15.6	20.9	164.4	40.0
3U6_TC8	179.5	13.4	17.9	151.1	25.0
3U6_TC9	148.8	10.8	14.5	121.6	9.0
3U9_TC1	184.9	19.5	26.1	174.4	150.0
3U9_TC2	210.2	19.3	25.8	195.9	140.0
3U9_TC3	233.4	19.9	26.6	218.5	117.0
3U9_TC4	240.0	19.8	26.5	223.3	94.0
3U9_TC5	239.0	19.1	25.5	221.1	76.0
3U9_TC6	233.6	17.8	23.9	215.2	60.0
3U9_TC7	218.7	15.6	20.8	200.0	40.0

Response Function	Mean (C)	Lower 95-95 Bar (C)	Upper 95-95 Bar (C)	TC Measurements (C)	Elevation (in.)
3U9_TC8	197.8	13.5	18.1	180.8	25.0
3U9_TC9	153.6	11.8	15.8	141.5	9.0
5T9_TC1	158.0	19.6	26.3	150.7	150.0
5T9_TC2	184.0	19.2	25.7	171.5	140.0
5T9_TC3	204.8	20.0	26.8	194.2	117.0
5T9_TC4	210.5	20.1	26.9	199.6	94.0
5T9_TC5	210.2	19.5	26.1	198.0	76.0
5T9_TC6	206.6	18.3	24.5	193.9	60.0
5T9_TC7	196.1	16.1	21.5	181.8	40.0
5T9_TC8	181.4	13.7	18.4	164.9	25.0
5T9_TC9	148.7	11.1	14.8	131.9	9.0
30A_TC1	171.7	19.2	25.7	160.8	150.0
30A_TC2	199.5	18.9	25.3	183.9	140.0
30A_TC3	222.7	19.6	26.2	206.2	117.0
30A_TC4	228.8	19.6	26.3	209.3	94.0
30A_TC5	228.3	19.0	25.4	207.9	76.0
30A_TC6	223.9	17.8	23.8	203.7	60.0
30A_TC7	211.6	15.6	20.8	191.3	40.0
30A_TC8	194.0	13.4	17.9	174.3	25.0
30A_TC9	153.7	11.4	15.2	136.6	9.0
57A_TC1	184.7	19.4	25.9	178.3	150.0
57A_TC2	211.7	19.1	25.6	201.7	140.0
57A_TC3	235.5	19.7	26.4	225.4	117.0
57A_TC4	242.1	19.7	26.4	229.2	94.0
57A_TC5	241.1	19.0	25.4	227.2	76.0
57A_TC6	235.9	17.8	23.8	220.7	60.0
57A_TC7	221.2	15.5	20.7	205.6	40.0
57A_TC8	200.3	13.5	18.1	186.2	25.0
57A_TC9	154.5	11.8	15.8	143.8	9.0

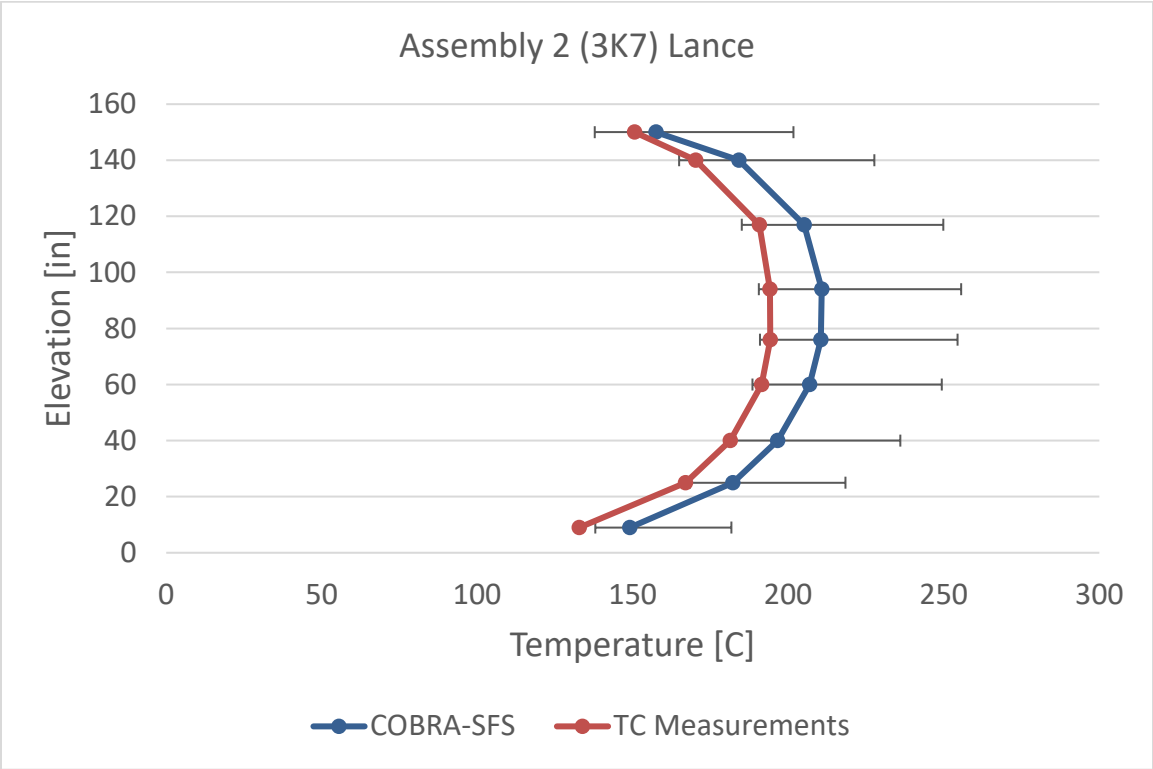

Figure 5-12. COBRA-SFS results assembly 2 (3k7) lance

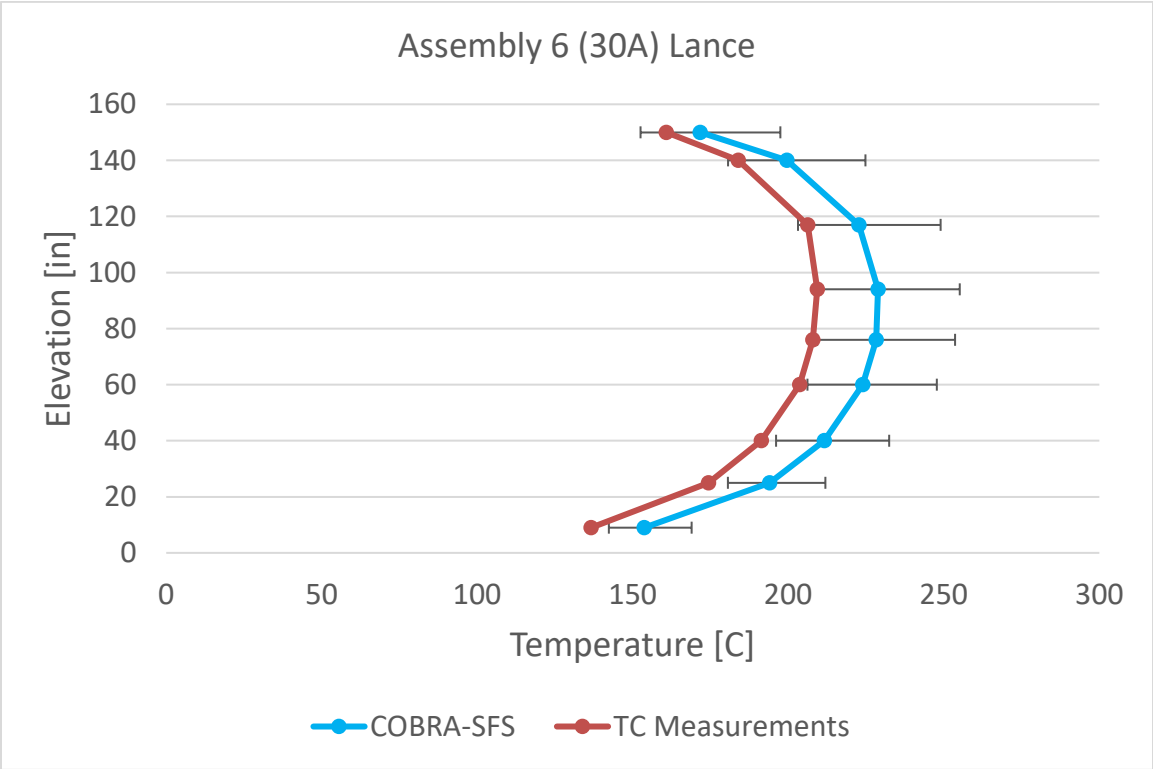

Figure 5-13. COBRA-SFS results assembly 6 (30A) lance

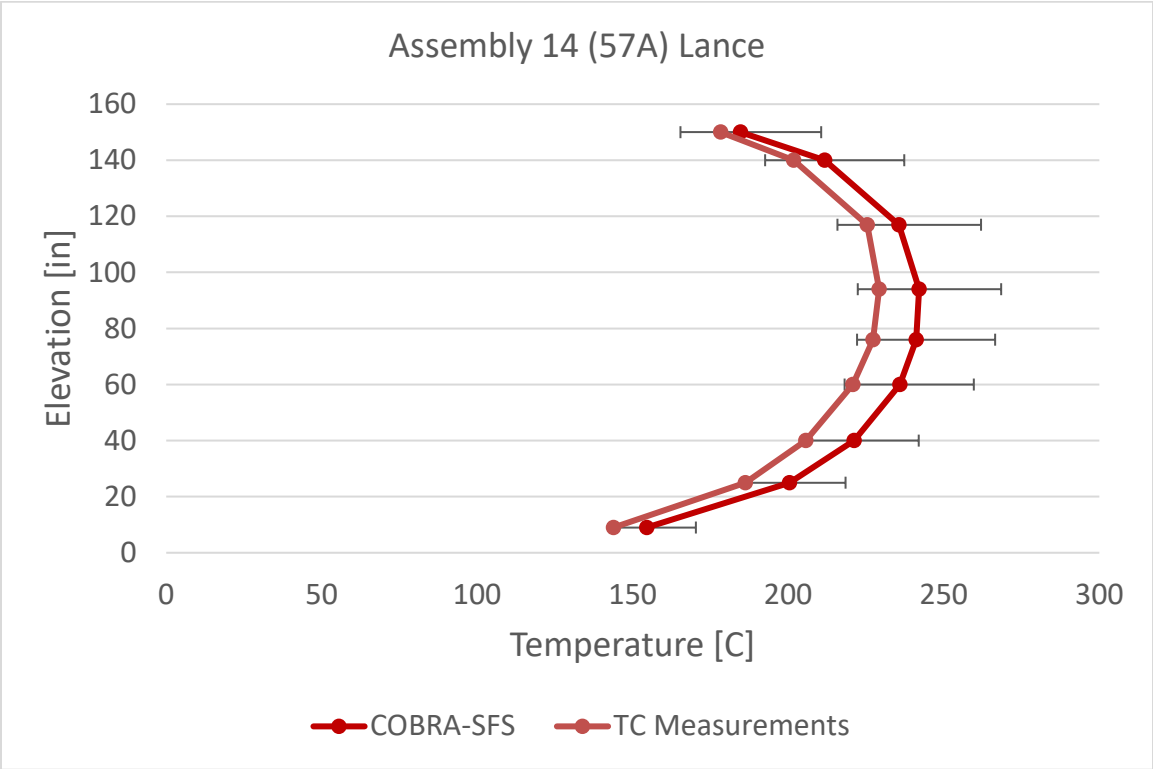

Figure 5-14. COBRA-SFS results assembly 14 (57A) lance

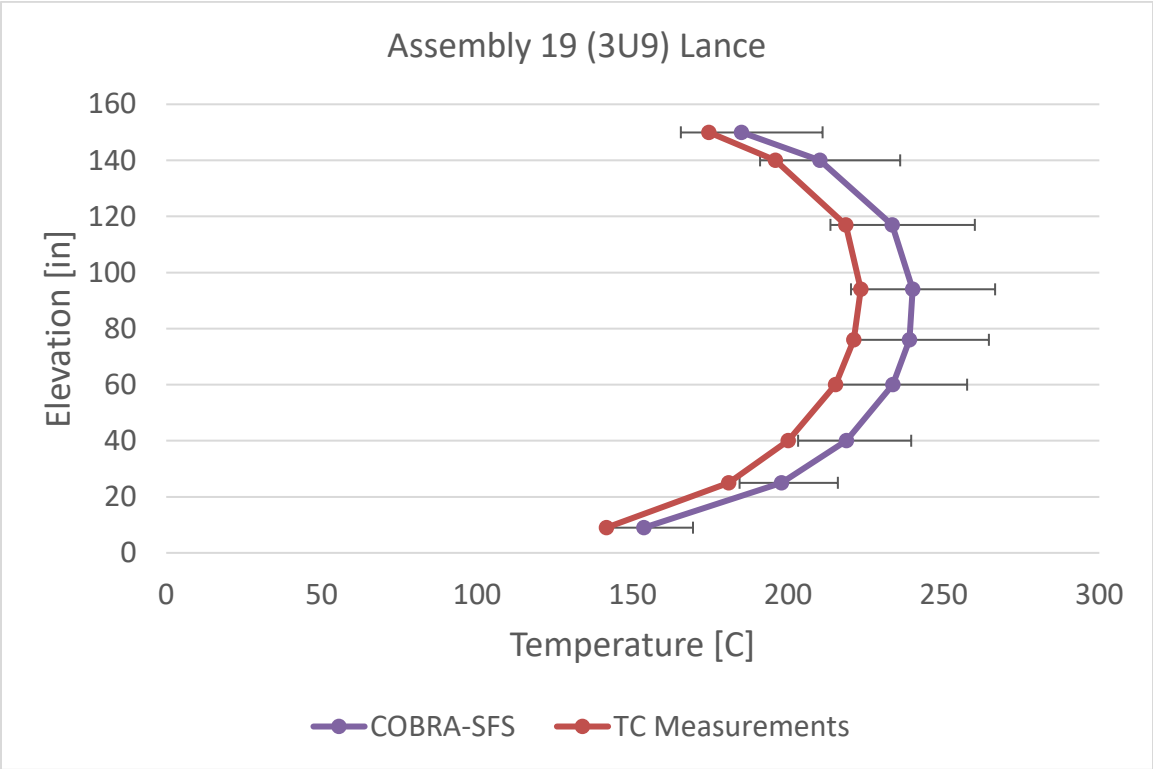

Figure 5-15. COBRA-SFS results assembly 19 (3U9) lance

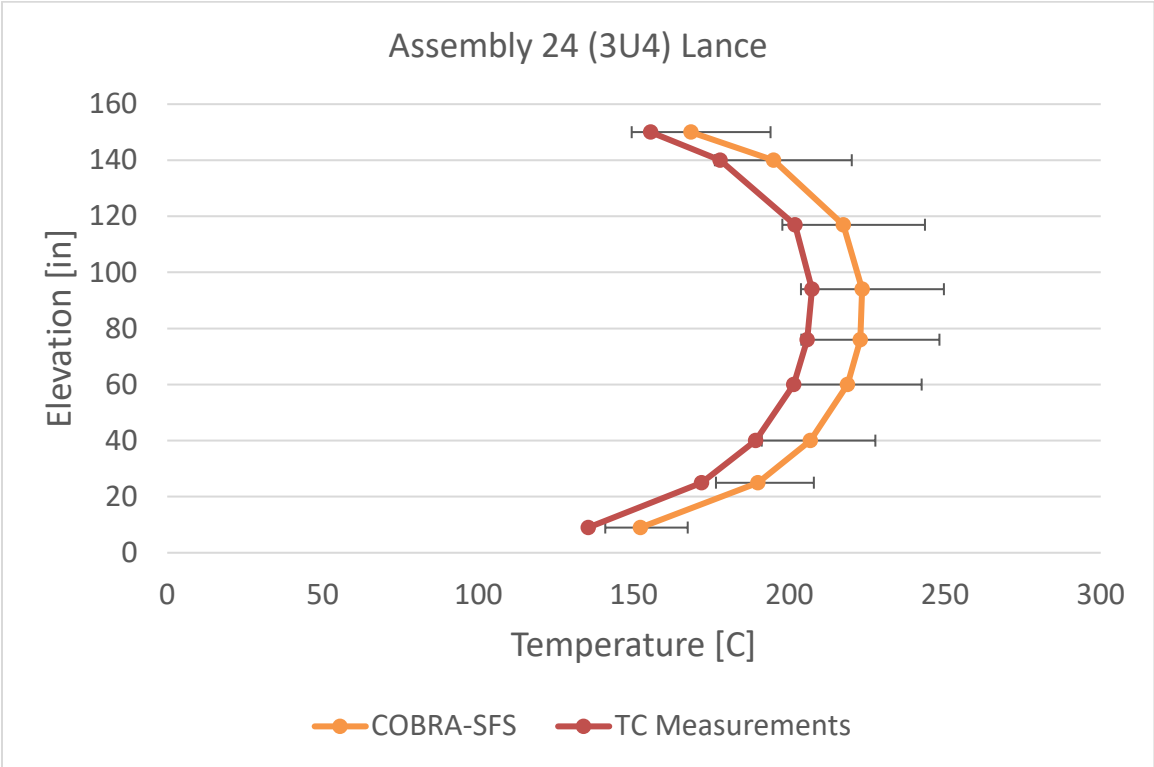

Figure 5-16. COBRA-SFS results assembly 24 (3U4) lance

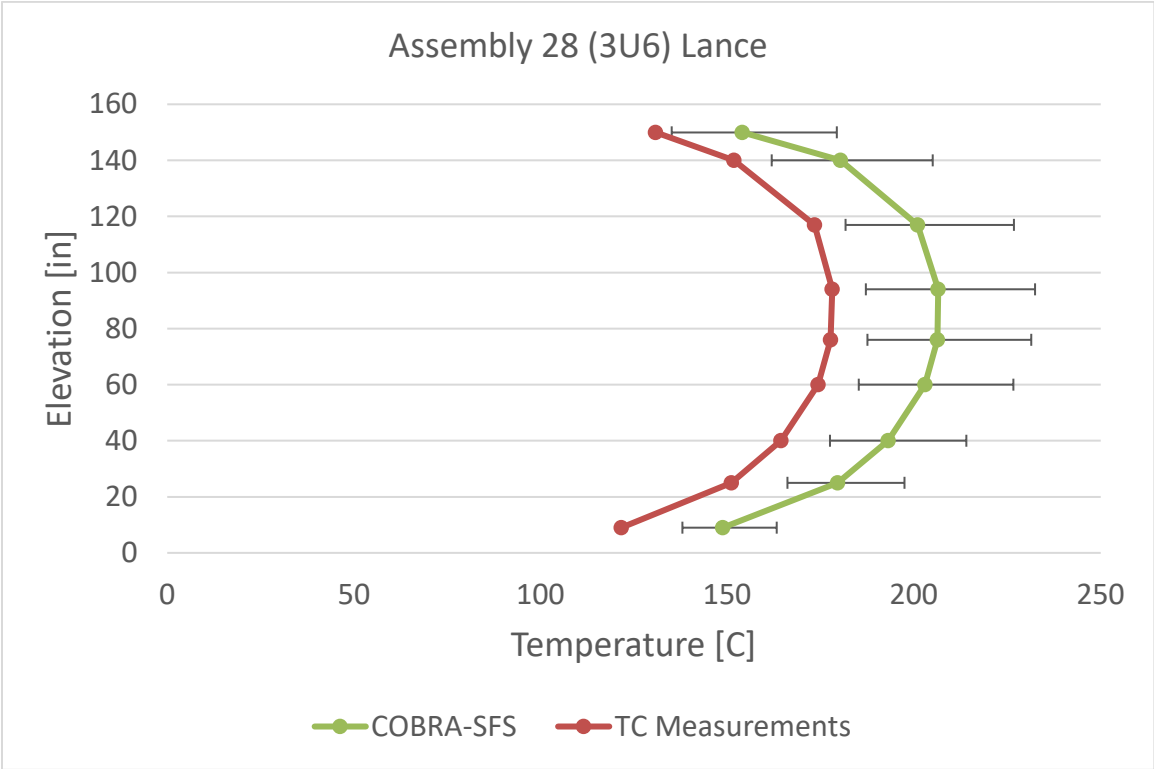

Figure 5-17. COBRA-SFS results assembly 28 (3U6) lance

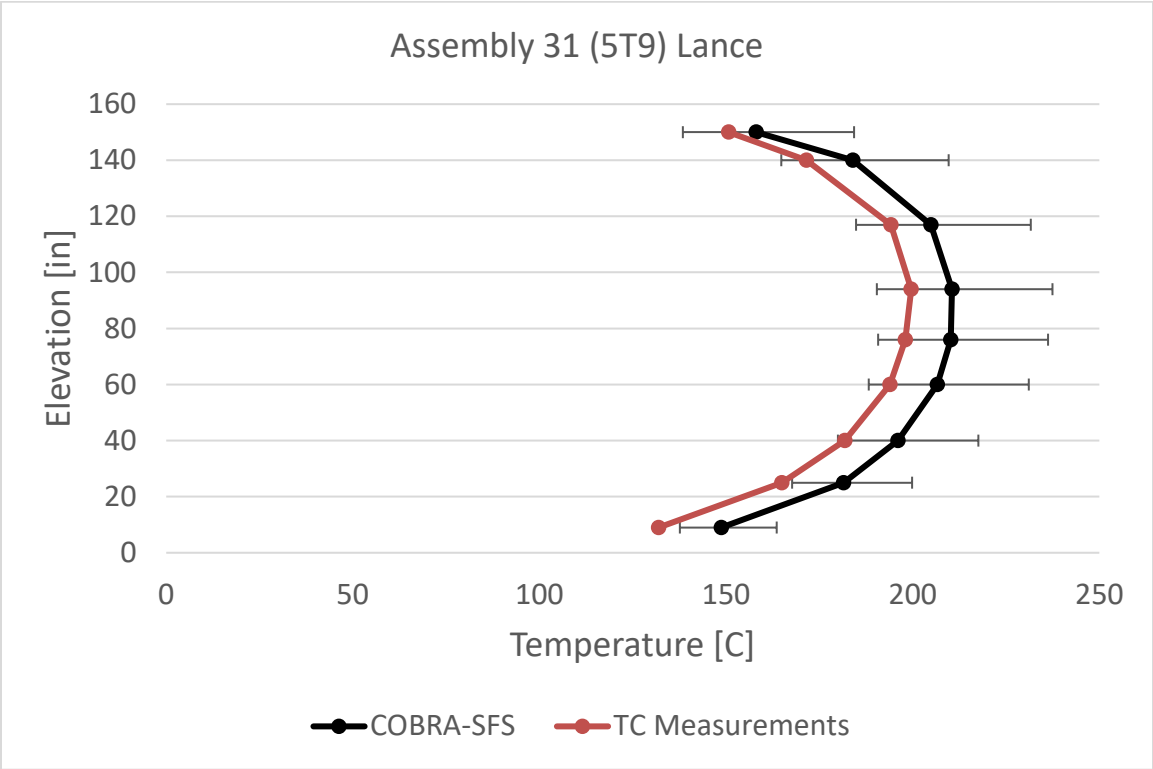

Figure 5-18. COBRA-SFS results assembly 31 (5T9) lance

5.3 Combined Uncertainty Results

This section shows some of the top-level results from the STAR-CCM+ and COBRA-SFS uncertainty quantification modeling. Figure 5-19 and Figure 5-20 show the PCT plotted with uncertainty vs the number of samples used in the analysis. This shows the relationship clearly between number of simulations and estimated input uncertainty with LHS. Another interesting result seen best in Figure 5-20 is the asymmetry of the uncertainty in PCT where the upper bound is farther from the mean than the lower bound especially when sample size is small. This asymmetry shows the advantage of an LHS UQ method where that data on the model's uncertainty would not be available through other UQ methodologies.

The other important result that is shown by comparing the two codes is the general similarity of the behavior of the two models. Both codes result in similar 95–95 confidence intervals and the range decreases with increasing sample size in a similar manner. Because of this similarity, this work is an example of how using two codes can successfully increase overall efficency. COBRA-SFS uses much fewer computing resources to run, as shown in section 5.4, and therefore is best suited to the type of exploratory uncertainty analysis demonstrated in this report. Although STAR-CCM+ was also used in a similar manner, it may not always be practical for larger models and for more results-focused applications. In this case, it is clear that COBRA-SFS can be used to determine an appropriate number of samples for the desired results. In this case, running over 50 samples has minimal benefit to shrinking the 95–95 interval. That knowledge can only be gained by running the models with over 100 samples. Using COBRA-SFS to test these scenarios, it becomes unnecessary to expend the extra time and resources running a STAR-CCM+ model to obtain the same information.

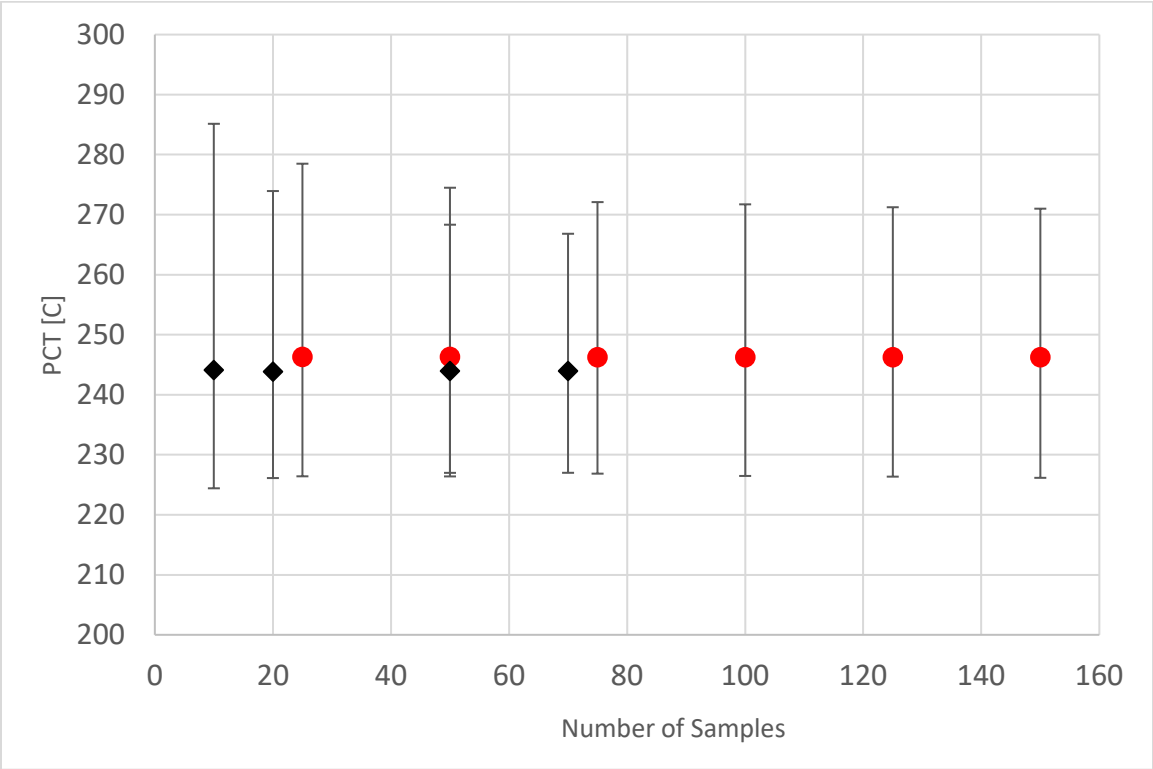

Figure 5-19. STAR-CCM+ PCT data (black) and COBRA-SFS PCT data (red)

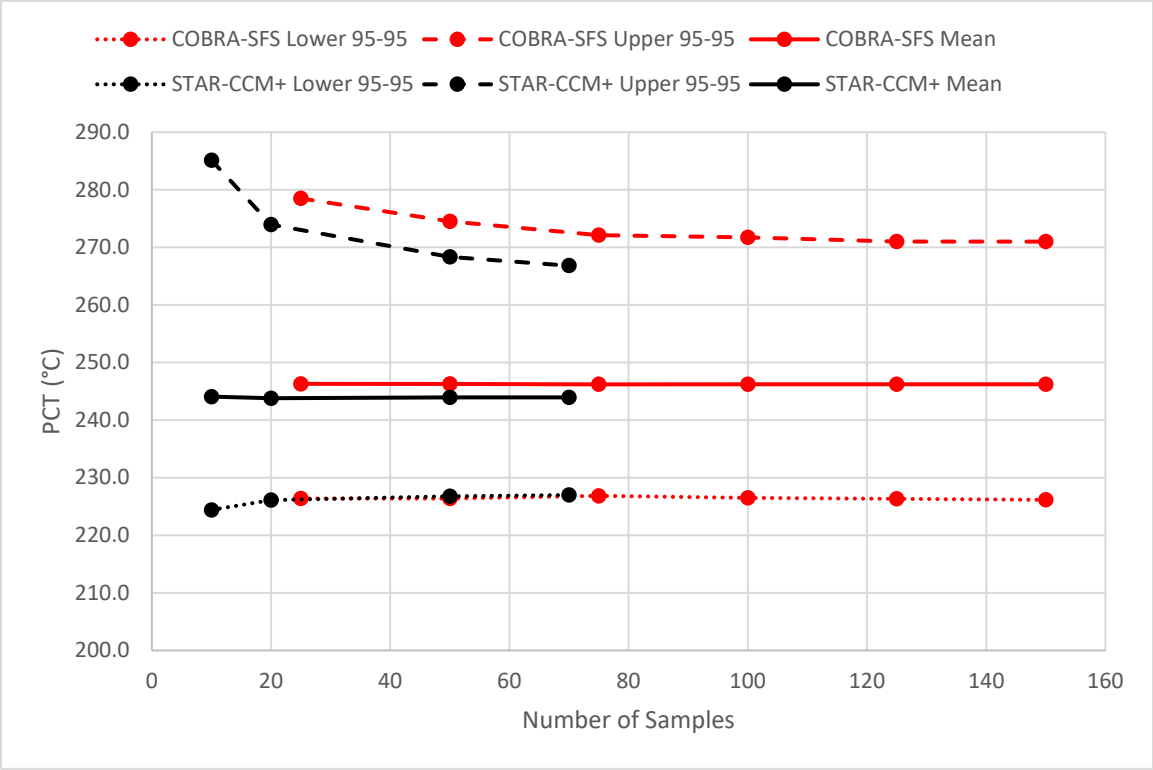

Figure 5-20. 95–95 interval vs number of samples

5.4 Computational Resources and Workflow

The computational and staff resources needed to run a model should always be considered when developing methodologies. In this case, COBRA-SFS and STAR-CCM+ were used in tandem to provide an example of how the two codes perform and investigate how they might best be utilized together.

The cases for the uncertainty analysis with STAR-CCM+ were run serially on PNNL's institutional computer Deception. Deception has 96 compute nodes with dual AMD EPYC 7502 CPUs running at 2.5 GHz. Each case was run on a single node with 64 cores and took approximately 3 hours to run. Analyzing the 70 cases took a little over 8 days to run. Parallel cases could be run in the future to speed up the overall time required to run the analysis with STAR-CCM+.

The COBRA-SFS modeling used a desktop system with Dual Intel Xenon Gold 5120 CPU @2.20 GHz and 2.19 GHz and 128 Gb of RAM. Although 28 cores were available, modeling used 25 simultaneous instances for each DAKOTA analysis, and this resulted in 70.2 Gb of memory use by the analysis process at any given time. Each simulation takes 2–4 hours to solve and 2.8 Gb of memory. This is larger than many COBRA-SFS models but not atypical. Wall time reported in Table 5-5 and Figure 5-21 reflects the time from the start of a DAKOTA analysis to the end with the vast majority of that time being analysis runs and a negligible time spent for DAKOTA to sample variables and compute statistics. DAKOTA's job scheduler automatically starts a new instance of the code when a core is free, which makes the larger simulation numbers more efficient in wall time than the smaller. For example, the time to complete 25 simulations was 3.9 hours, whereas in the 150-simulation case, the average time for 25 simulations was 2.8 hours.

Table 5-5. Wall time for COBRA-SFS and STAR-CCM+

COBRA-SFS		STAR-CCM+	
Simulations	Wall Time (hr.)	Simulations	Wall Time (hr.)
25	3.9	10	28
50	6.2	20	57
75	9.2	50	142
100	12.8	70	198
125	15.4		
150	17.2		

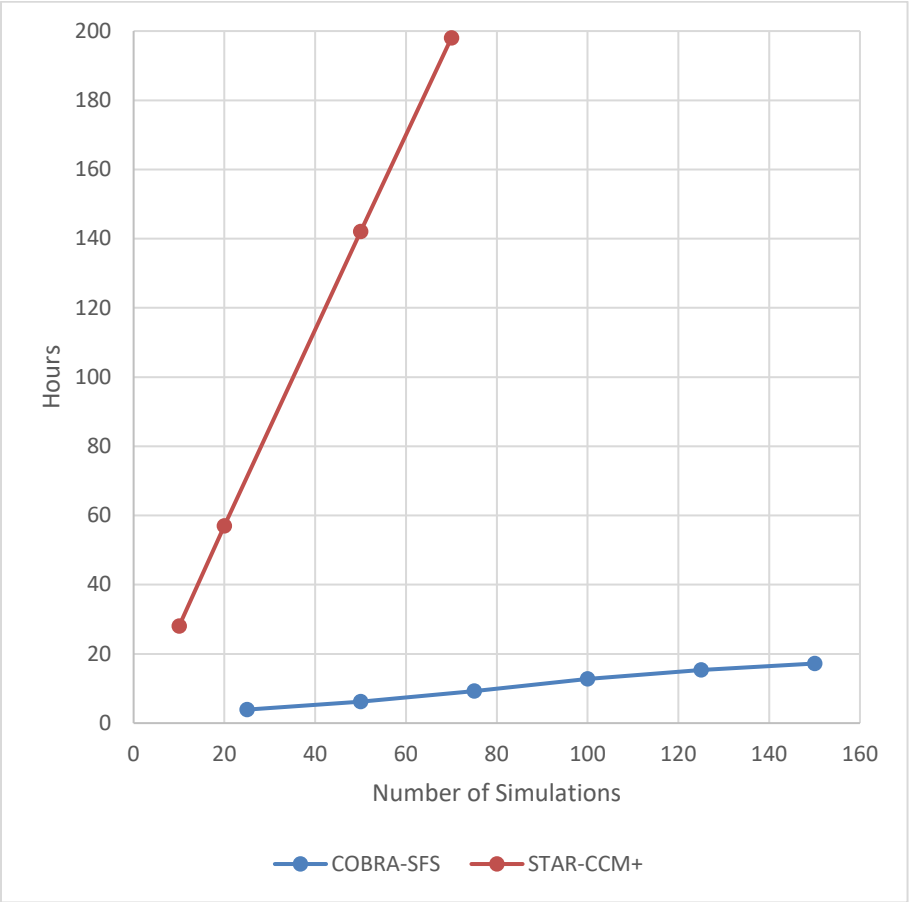

Figure 5-21. Wall time vs. number of simulations

To determine the number of simulations to run in a single code scenario, the benefit must be weighed against the necessary simulation resources and time. In the case of a two-code workflow, the optimum simulation number can be determined with the faster code (COBRA-SFS in this case) and applied to the slower code (STAR-CCM+ in this case). This method provides the greatest time efficiency to analysts and a more efficient use of computing resources overall.

This page is intentionally left blank.

6. CONCLUSIONS

This report covers three major modeling task areas that provide an overview of the types of sensitivity and uncertainty present in a spent fuel storage and transportation system. Section 3 discusses sensitivity and uncertainty analysis in the effective thermal conductivity model for the fuel region and the application of these results to a single assembly model. Section 4 shows sensitivity analysis of a full cask model in the TN-32B and Section 5 demonstrates the overall uncertainty workflow using COBRA-SFS and STAR-CCM+ developed from the sensitivity work in the preceding sections. Key outcomes and demonstrations from this work include:

- The results of the effective thermal conductivity uncertainty quantification show that the quantity, while important to modeling, has minimal effect on overall uncertainty and can be estimated reliably with different codes.
- Key sensitivities were identified in the TN-32B High Burnup Demonstration Research Project Cask; these will inform uncertainty analysis and future transient modeling.
- LHS UQ was demonstrated as a practical method for UQ even with computationally intensive full cask models.
- Full cask model uncertainty results showed good agreement with data and demonstrated the importance of input parameter distribution selection.
- Methodology for a streamlined workflow utilizing multiple analysis tools was developed and can be applied to any future spent fuel cask modeling or other relevant systems that can be computationally modeled.

The work in this report was undertaken to study sensitivities and uncertainties in spent fuel cask modeling and to then develop methodologies for uncertainty analysis that can be practically applied to future work. These goals were successfully met and there is now a demonstrated workflow in place that the U.S. Department of Energy can use when analyzing thermal models and apply to other relevant computational modeling areas.

This page is intentionally left blank.

7. REFERENCES

Adams, B. M., M. S. Ebeida, M. S. Eldred, G. Geraci, J. D. Jakeman, K. A. Maupin, J. A. Monschke, J. A. Stephens, L. P. Swiler, D. M. Vigil, T. M. Wildey, W. J. Bohnhoff, K. R. Dalbey, J. P. Eddy, J. R. Frye, R. W. Hooper, K. T. Hu, P. D. Hough, M. Kahlil, E. M. Ridgway, J. G. Winokur, and A. Rushdi. 2018. *Dakota, A Multilevel Parallel Object-Oriented Framework for Design Optimization, Parameter Estimation, Uncertainty Quantification, and Sensitivity Analysis: Version 6.9 User's Manual*. SAND2014-4633. Sandia National Laboratories Albuquerque, NM.

Akkurt, H. and A. Csontos. 2019. *International Thermal Modeling Benchmark Description for High-Burnup Used Fuel Dry Storage System*. Report number 3002018498. Electric Power Research Institute. Palo Alto, CA.

Angelucci, M., S. Paci, F. Feria, and L. Herranz. 2022. "Uncertainty and Sensitivity Analysis of a Dry Cask for Spent Nuclear Fuel." *Energies* 15 (3): 1216. https://doi.org/10.3390/en15031216.

Bahney, R. and T. Lotz. *Spent Nuclear Fuel Effective Thermal Conductivity Report*. 1996. Prepared for the U.S. DOE, Yucca Mountain Site Characterization Project Office by TRW Environmental Safety Systems, Inc.

Csontos, A. 2020. *High-Burnup Used Fuel Dry Storage System Thermal Modeling Benchmark – Round Robin Results*. Report number 3002013124. Electric Power Research Institute. Palo Alto, CA.

Dakota. 2021. Dakota 6.15 (computer software). Albuquerque, New Mexico: Sandia National Laboratories.

Durbin, S. and E. R. Lindgren. 2017. *Thermal-Hydraulic Results for the Boiling Water Reactor Dry Cask Simulator*. Sandia National Lab SAND-2017-10551R; 657411. https://www.osti.gov/servlets/purl/1398335.

EPRI. 2014. *High Burnup Dry Storage Cask Research and Development Project – Final Test Plan*. Contract No. DE-NE-0000593, Electric Power Research Institute, Palo Alto, California.

Fort, J. A., D. J. Richmond, J. M. Cuta, and S. R. Suffield. 2019a. *Thermal Modeling of the TN-32B Cask for the High Burnup Spent Fuel Data Project*. Pacific Northwest National Laboratory PNNL-28915. Richland, WA.

Fort, J. A., D. J. Richmond, B. J. Jensen, and S. R. Suffield. 2019b. *High-Burnup Demonstration: Thermal Modeling of TN-32B Vacuum Drying and ISFSI Transients*. Pacific Northwest National Laboratory PNNL-29058. Richland, WA.

Fort, J. A., D. J. Richmond, and B. J. Jensen. 2020. *Thermal Models of a TN-32B Cask for the International Benchmark*. Pacific Northwest National Laboratory PNNL-30645. Richland, WA.

Glaeser, H. 2008. "GRS Method for Uncertainty and Sensitivity Evaluation of Code Results and Applicatins." *Science and Technology of Nuclear Installations*. http://dx.doi.org/10.1155/2008/798901.

Ivanov, K., M. Avramova, S. Kamerow, I. Kodeli, E. Sartori, E. Ivanov, and O. Cabellos. 2013. *Benchmarks for Uncertainty Analysis in Modelling (UAM) for the Design, Operation and Safety Analysis of LWRs – Volume I: Specification and Support Data for Neutronics Cases (Phase I)*. Organisation for Economic Co-Operation and Development.

Jensen, B. J., S. R. Suffield, M. E. Higley, B. M. Hom, and J. A. Fort. 2021. *Modeling Environmental Effects on Ventilated Spent Fuel Storage Systems*. Pacific Northwest National Laboratory. Richland, WA.

Khalil, I., Q. Pratt, H. Schmachtenberger, and R. Ghanem. 2018. "Heat Transfer Modeling of Spent Nuclear Fuel Using Uncertainty Quantification and Polynomial Chaos Expansion." *Journal of Heat Transfer* 140 (2): 022001. https://doi.org/10.1115/1.4037501.

Kloos, M. and E. Hofer. 1999. *SUSA - PC, A Personal Computer Version of the Program System for Uncertainty and Sensitivity Analysis of Results from Computer Models, version 3.2, User's Guide and Tutorial*. Gesellschaft fur Anlagen- und Reaktorsicherheit, Garching, Germany.

Knio, O. and O. Le Maître. 2006. "Uncertainty propagation in CFD using polynomial chaos decomposition." *Fluid Dynamics Research* 38 (9): 616–640. https://doi.org/10.1016/j.fluiddyn.2005.12.003.

Lindgren, E. R. and S. Durbin. 2017. *Materials and Dimensional Reference Handbook for the Boiling Water Reactor Dry Cask Simulator*. Sandia National Laboratory. Albuquerque, NM.

Mahagin, D. E., J. L. Bates, and D. E. Baker. 1973. *Boron Carbide Thermal Conductivity*. HEDL-TME 73–78. Hanford Engineering Development Laboratory. Richland, WA.

Michener, T. E., D. R. Rector, J. M. Cuta, and H. E. Adkins, Jr. 2017. *COBRA-SFS: A Thermal-Hydraulic Code for Spent Fuel Storage and Transportation asks, Cycle 4a.* Pacific Northwest National Laboratory PNNL-24841. Richland, WA.

Najm, H. 2009. "Uncertainty Quantification and Polynomial Chaos Techniques in Computational Fluid Dynamics. *Annual Reviews of Fluid Mechanics* 41: 35–52. https://doi.org/10.1146/annurev.fluid.010908.165248.

Oberkampf, W. L. and C. J. Roy. 2010. *Verification and Validation in Scientific Computing*. New York: Cambridge University Press.

Suffield, S.R., D. J. Richmond, and J. A. Fort. 2020a. *Modeling of the Boiling Water Reactor Dry Cask Simulator.* Pacific Northwest National Laboratory PNNL-28424, Rev. 1. Richland, WA.

Suffield, S. R., D. J. Richmond, B. J. Jensen, J. A. Fort, and C. Grant. 2020b. *Modeling of the Horizontal Boiling Water Reactor Dry Cask Simulator.* Pacific Northwest National Laboratory PNNL-30145. Richland, WA.

Waldrop, K. 2019. *High Burnup Dry Storage Research Project Cask Loading and Initial Results*. Electric Power Research Institute Report number 3002015076. Palo Alto, CA.

Yaman, K. and Ö. Taga. 2018. "Thermal and Electrical Conductivity of Unsaturated Polyester Resin Filled with Copper Filler Composites." *International Journal of Polymer Science* 2018, Article ID 8190190. https://doi.org/10.1155/2018/8190190.